

Dynamics of crowded and active biological systems

by

Michael W. Stefferson

B.S., University of Arizona, 2012

M.S., University of Colorado, 2015

A thesis submitted to the

Faculty of the Graduate School of the

University of Colorado in partial fulfillment

of the requirements for the degree of

Doctor of Philosophy

Department of Physics

2018

This thesis entitled:
Dynamics of crowded and active biological systems
written by Michael W. Stefferson
has been approved for the Department of Physics

Professor Meredith Betterton

Professor Attendant Rank Matthew Glaser

Date _____

The final copy of this thesis has been examined by the signatories, and we find that both the content and the form meet acceptable presentation standards of scholarly work in the above mentioned discipline.

Stefferson, Michael W. (Ph.D., Physics)

Dynamics of crowded and active biological systems

Thesis directed by Professor Meredith Betterton

Interactions between particles and their environment can alter the dynamics of biological systems. In crowded media like the cell, interactions with obstacles can introduce anomalous subdiffusion. Active matter systems, *e.g.*, bacterial swarms, are nonequilibrium fluids where interparticle interactions and activity cause collective motion and dynamical phases. In this thesis, I discuss my advances in the fields of crowded media and active matter. For crowded media, I studied the effects of soft obstacles and bound mobility on tracer diffusion using a lattice Monte Carlo model. I characterized how bound motion can minimize the effects of hindered anomalous diffusion and obstacle percolation, which has implications for protein movement and interactions in cells. I extended the analysis of binding and bound motion to study the effects of transport across biofilters like the nuclear pore complex (NPC). Using a minimal model, I made predictions on the selectivity of the NPC in terms of physical parameters. Finally, I looked at active matter systems. Using dynamical density functional theory, I studied the temporal evolution of a self-propelled needle system. I mapped out a dynamical phase diagram and discuss the connection between a banding instability and microscopic interactions.

Dedication

To my family and the Bro-op.

Acknowledgements

Reflecting back on my time in Boulder, it is almost overwhelming to realize how many people made my time here so special. I am so lucky to have had an amazing support system that I could always rely on. Thank you to everyone.

It's safe to say that I would not be writing this if it were not for my advisors Meredith Betterton and Matt Glaser. Meredith, I am grateful for your guidance and everything you taught me over the years. Your broad knowledge base in physics, math, and biology as well as your ability to communicate science always impressed me. Matt, you have always been someone I could count on for support. You are a great scientist and friend, and I always admired your skepticism and insight. While technically a collaborator, I would like to thank my unofficial third advisor, Loren Hough. Some of our scientific discussions were the most rewarding I've had. I'd also like to thank collaborator and committee member Franck Vernerey for our fruitful discussions. I appreciate your insight and help on projects, and I regret that I did not get to work with you more. Since I've hit almost my whole committee, it would be a shame to leave out Joe MacLennan. Joe, I always enjoyed our chats in the hallway. Thanks for being my biggest mohawk fan and for the coloring ideas. Shout out as well to others in the department: Tom DeGrand, Mike Hermele, Paul Romatschke, Leo Radzihovsky, John Bohn, Mike Ritzoller, Mike Dubson, Oliver Nix, Kirsten Apocada, Annett Baumgartner, Dakota Nanton, Lauren Moreno, Jeanne Nijhowne, and others for stimulating discussions, advice, and help.

As for the rest of my group, thank you to Chris Edelmaier, Adam Lamson, Robert Blackwell, and Zach Gergely for all of the help and advice. Special thanks to Laura Maguire and Hui-Shun

Kuan for working on these projects with me; it was a pleasure. And then, there is Jeffrey Moore. Jeff, you may have had the biggest influence on me over the three years since we've known each other. My Windows, git-less, and VIM-less days feels like a lifetime ago. Thank you for helping me become the computational physicist I am today; I couldn't have done it without you. I will never forget your patience and advice. You are an incredible problem solver and code monkey, and I cannot wait to see what you accomplish. I hope I can help on the other side.

Outside of work, thank you to my loving family for their support. I am so lucky to have such loving parents. From the days of AYSO soccer to my eleventh year of college, you have been cheering me along all the way. It truly means a lot. Lindsay, you've always been the greatest source of emotional support. Thanks for always knowing how to make me laugh. I love you all so much.

I do not think I would have survived graduate school without my friends in Boulder. The Bro-op has been one of my greatest sources of joy, adventure, and personal connection. Short-term members Katie, Stacey, and Dimitri: it was a blast, and I wish we had more time to live together. Stephen, Tom, and Matt, you guys will forever be my brothers. I am so grateful for our time over the years. You helped me keep my sanity. Thank you. Living with one the world's most brilliant physicists, electrical engineers, and a polymath was quite the experience. You taught me the value of hard work, skepticism, communication, and critical thinking—even when it is inconvenient. Tom, thank you for being the best friend I could ever hope for. I'll never forget all you have done for me. I would also like to thank the Dinner Club for wonderful memories over the ($> 5!$) years, Martha for crafting, Molly for our conversations, and Phoebe for the pottery help and laughs.

Ok, I'm almost done. Many thanks to Boulder's premier party mixed frisbee team, All Jeeps All Night, for having me as a practice player. Captains Marek, Tristan, and Grant, you made this all possible. Thanks for the time you've spent organizing everything; you've brought me and others countless great memories. Shout out to Joliene, Stevie, and all the wonderful baristas at Pekoe for keeping me fueled with free coffee for three years. It was fun being the guy who got free stuff, but no one knew why. Thanks to Stephanie and the wonderful PTs for keeping me up and running over the years. To all the awesome musicians who played at our house parties, thank you for some of

my fondest memories. To my fellow Cocktail Burrito band mates Justin Griffith and Tom Nummy (and biggest fan Dani), thanks for letting me play rhythmless guitar and bass and sing off-key with you guys. Finally, thanks to the Armer boys, HMS Beagle, and the 41st house for always hosting fun events. Clearly, I think work-life balance is important. Thanks again everyone who helped me with that.

Finally, science ain't free. Thanks for the support from the SMRC (DMR-1420736), Biofrontiers Computing Core (NIH 1S10OD012300), and RMACC Summit supercomputer (awards ACI-1532235 and ACI-1532236).

Contents

Chapter

1	Introduction	2
1.1	Brownian dynamics	4
1.2	Random walks 101	5
1.3	Effects of obstacles	8
1.4	Effects of interactions and activity	9
2	Sticky and slippery soft obstacles	11
2.1	Anomalous diffusion	13
2.2	Lattice models	14
2.3	Model	15
2.3.1	Simulation methods	16
2.3.2	Trajectory analysis	18
2.4	Sticky soft obstacles	22
2.4.1	Sticky soft obstacles in 3D	26
2.5	Slippery soft obstacles	26
2.5.1	Slippery soft obstacles in 3D	27
2.5.2	Comparison of sticky and slippery obstacles in 2D	27
2.6	Semi-slippery obstacles	29
2.7	Varying obstacle size	30

2.7.1	Sticky obstacles of varying size	30
2.7.2	Slippery obstacles of varying size	32
2.8	Conclusion	33
3	Biofilter modeling	37
3.1	Reaction-diffusion model of selectivity in biofilters	38
3.1.1	Linear solution and numerics	40
3.2	Selectivity in the nuclear pore	42
3.2.1	Comparison to lattice model	44
4	Banding instability of active hard needles	46
4.1	Microscopic interactions	47
4.1.1	Langevin equations of motion	48
4.2	Continuum equations	49
4.2.1	Dynamical density functional theory	50
4.2.2	Pseudospectral numerical scheme	51
4.3	Results	52
4.3.1	Banding instability	53
4.3.2	Connection to previous work	55
4.3.3	Connection to simulations	56
4.4	Conclusions	58
5	Validation and additional features of the code	60
5.1	Isotropic-nematic transition and numerical analysis	60
5.2	Concentration dependent diffusion	60
5.3	Effects of course-graining	64
5.3.1	Comparing simulation to DDFT	66
5.4	Finite-size effects	66

5.5 External potentials in DDFT	69
6 Conclusions and future directions	71
6.1 Conclusions	71
6.2 Future directions	72
Bibliography	74

Appendix

A Fluctuation-dissipation theorem	84
B Numerics for Brownian dynamics simulations	86
C Derivation of the Smoluchowski equation	88
D Derivation of DDFT	90
E Second virial approximation	93
F Repositories	95

Tables**Table**

3.1	NPC parameters	39
3.2	Selectivity comparison between experiment and model	44
F.1	GitHub repositories	95

Figures

Figure

2.1	Soft sticky and slippery model schematic	16
2.2	MSD curves	18
2.3	Fitting procedure	20
2.4	Sticky diffusion in 2D	22
2.5	Percolation threshold	23
2.6	Sticky diffusion in 3D	25
2.7	Slippery diffusion in 2D	27
2.8	Slippery obstacles in 3D	28
2.9	Comparision	28
2.10	Semi-slippery obstacles	29
2.11	Size effects cartoon	30
2.12	Sticky size effects	31
2.13	Slippery size effects	33
3.1	NPC model schematic	38
3.2	Transient flux	43
3.3	Selectivity versus dissociation constant	43
4.1	Banding instability	53
4.2	Band stability schematic	54

4.3	Dynamical phase diagram	55
4.4	Band structure	56
4.5	Simulation snapshots	57
5.1	IN transition	61
5.2	Concentraion dependent diffusion (small flock perturbation)	62
5.3	Concentraion dependent diffusion (large flock perturbation)	63
5.4	Course-graining	64
5.5	Finite-size effects: homogeneous nematic initial condition	67
5.6	Finite-size effects: band initial condition	68
5.7	External potential validation	69

help and laughs

Chapter 1

Introduction

Interactions, either between particles or with the environment, play a crucial role in the dynamics of biological systems. For example, there are biological polymeric filters which facilitate the transport of molecules, nanoparticles, viruses and other organisms through interactions between the polymers and particles [1]. In biological crowded media, obstacles can inhibit motion and introduce anomalous subdiffusion [2]. This has implications for the motion of lipids or macromolecules in membranes [3–10] and the cell interior [11]. Active matter systems, *e.g.*, a bacterial swarm [12–14], can exhibit an array of exotic phenomena: dynamical phases, self assembly, and collective motion [15] because of the interplay between particle-particle interactions and nonequilibrium activity. Understanding how microscopic interactions influence particle dynamics, transport, and macroscopic phases could assist in designing and tuning these systems.

The commonality between these crowded and active systems is Brownian motion. A particle is considered Brownian if it undergoes random motion in an environment, typically called a heat bath. The heat bath exerts two forces on the Brownian particle: a random fluctuating force and frictional drag force [16]. Note, the term heat bath, solvent, and solution will be used interchangeably to describe the surrounding fluid environment. Brownian motion was first reported by Robert Brown in 1827 when he observed the random motion of pollen in water. Einstein’s interpretation that the phenomenon could be described by water molecules bumping into the pollen provided further evidence of the existence of atoms and molecules [17]. If we knew all the trajectories of a solvent

particles, we could in principle calculate the motion of the Brownian particle. However, these degrees of freedom are intractable. Instead, we approximate the effect of the solvent particles as a random fluctuating and damping force. The equation which describes this motion is the Langevin equation [16]. In most cases, we are interested in the overdamped limit, which gives us Brownian dynamics (BD).

The study of Brownian dynamics is ubiquitous in physics: diffusion of holes and electrons in semiconductors [18], Doppler cooling of neutral atoms [19], and motion of macromolecules in biological systems [20]. The primary focus of this thesis is analyzing different Brownian systems found in biology. I will examine the role of binding and bound motion in crowded environments, transport of proteins across the nuclear pore complex (NPC), and dynamical phases in active matter systems. I will use Brownian dynamics simulations, lattice Monte Carlo models, kinetic Monte Carlo, and numerical analysis of partial differential equations and describe how I implemented and advanced these tools.

In this thesis, I will begin by first discussing various Brownian systems and providing the essential theory. I will then discuss a lattice Monte Carlo model, which studied the effects of binding and bound motion on diffusion in a crowded environment [21]; results that have implications for various biological systems. Next, I will discuss transport across biofilters like the nuclear pore complex. I will present a minimal reaction diffusion equation that can predict the selectivity (*i.e.*, what proteins can and cannot easily pass through) of the NPC in terms of measurable parameters. I then move to active matter systems: nonequilibrium systems which can convert some source of stored energy into (kinetic) motion [15]. I will discuss how to derive macroscopic equations of motion starting from microscopic interactions using dynamic density functional theory (DDFT) [22–25], and how a pseudospectral theory was implemented to numerically evaluate them. Finally, I will apply this theory to a system of self-propelled hard needles and conclude.

1.1 Brownian dynamics

The equation of motion of a particle in a one dimensional heat bath is given by the Langevin equation [16]

$$m\ddot{x} = -\frac{dU(x)}{dx} - \zeta\dot{x} + \xi(t), \quad (1.1)$$

where x is the position, ζ the drag coefficient, $U(x)$ the potential energy from external fields, ξ the random uncorrelated fluctuating force, or noise, and the overdot means derivative with respect to time. The average properties of the noise are

$$\langle \xi(t) \rangle = 0, \quad (1.2)$$

$$\langle \xi(t)\xi(t') \rangle = 2\zeta k_B T \delta(t - t'), \quad (1.3)$$

where k_B is the Boltzmann factor, T the temperature, δ the Dirac delta function, and $\langle \dots \rangle$ the ensemble average over all noise realizations. Here, we assumed that the drag is homogeneous (constant in space). The Langevin equation is Newton's second law with forces from gradients in potential energy and the drag and random force provided by the heat bath. The drag and random force are connected through the drag coefficient (Eqn. 1.1 and 1.3). This is a consequence of the fluctuation-dissipation theorem [16], which is derived for Brownian motion in Appendix A.

To understand the overdamped limit, assume the particle experiences a constant force f from an external field and temporarily ignore the random force to determine the behavior of the average velocity. Solving the linear ordinary differential equation for the velocity, we get

$$\dot{x}(t) = f/\zeta + e^{-\zeta t/m} [\dot{x}(0) - f/\zeta]. \quad (1.4)$$

The particle's velocity exponentially decays with rate ζ/m from its initial value to a steady state value f/ζ . Now, if we are interested in time scales larger than $\tau_r = m/\zeta$, the velocity is constant. These time scales can be extremely small, $\tau_r \sim 10^{-7}\text{--}10^{-9}$ sec, in colloidal and biological systems [20, 26]. Brownian dynamics is this overdamped limit: the velocity decays so quickly to a steady state value that we can drop the inertial terms from the Langevin equation. In the overdamped limit,

the Langevin equation describing Brownian dynamics [16, 27] is

$$\dot{x} = \zeta^{-1} \left[-\frac{dU(x)}{dx} + \xi(t) \right]. \quad (1.5)$$

Eqn. 1.5 resembles a biased random walk, allowing us to discover the connection between the Langevin equation and diffusion.

1.2 Random walks 101

The random fluctuating force leads to a connection between Brownian dynamics and a discrete random walk. By discrete, I mean that the particle will take a random step Δx at a rate $1/\tau$. On average, $\langle \Delta x \rangle = 0$ and $\langle \Delta x^2 \rangle = l^2$ where l is the characteristic step length scale. After N steps, the particle's total displacement is a sum over i steps

$$x_N - x_0 = \sum_{i=1}^N \Delta x_i. \quad (1.6)$$

This equation is at the heart of the lattice Monte Carlo models and BD simulations we will discuss later. Let's imagine repeating this experiment several times. In doing so, we hope to say something meaningful about the average behavior of the motion by exploiting the properties of the random step. Upon averaging over experiments, the mean squared displacement (MSD) is

$$\langle x_N - x_0 \rangle^2 = \left\langle \sum_i^N \Delta x_i \sum_j^N \Delta x_j \right\rangle = Nl^2 = 2Dt, \quad (1.7)$$

where $D = \frac{l^2}{2\tau}$. Here, we used the fact that steps at different times are uncorrelated $\langle \Delta x_i \Delta x_j \rangle = \delta_{ij}l^2$ and that $N = \frac{t}{\tau}$ where t is the total time of the random walk. D is the diffusion coefficient; it connects the measurable spread of a random walk, *i.e.*, $\langle x^2 \rangle$, to time. For arbitrary dimension d , the MSD is

$$\langle r^2(t) \rangle = 2dDt, \quad (1.8)$$

where now $D = \frac{l^2}{2d\tau}$, τ the step frequency along any dimension, and r the total displacement, $r^2 = \sum_{i=1}^d x_i^2$.

A brief comment on what we mean by averaging $\langle \dots \rangle$. Typically, this is called an ensemble or noise average. This means repeating the experiment with the same initial conditions and averaging the results. By doing this, we are exploiting the average properties of the noise.

Now that we explained the connection between random walks and the diffusion coefficient, we can return to Eqn. 1.5. In the absence of interactions and fields, the overdamped Langevin equation is

$$\dot{x} = \zeta^{-1}\xi(t). \quad (1.9)$$

Upon integration with respect to time, we get

$$x(t) - x(0) = \int_0^t \zeta^{-1}\xi(t') dt'. \quad (1.10)$$

Since ξ is a random force, we can interpret this integral as a sum of random steps of length $\zeta^{-1}\xi(t')dt'$ [27].

Let's write the integral as a sum over N_t time steps of length δt , *i.e.*, $t = N_t\delta t$. This discretization gives

$$x(t) - x(0) = \int_0^t \zeta^{-1}\xi(t') dt' \approx \sum_{i=1}^{N_t} \zeta^{-1}\xi_i \delta t. \quad (1.11)$$

When we discretize time, we are assuming that the noise is constant over the length of a time step. Since ξ is uncorrelated in time, we are summing uncorrelated steps just like in the discrete random walk. We can also translate ξ into a time discretization framework, $\langle \xi_i \xi_j \rangle = \frac{2\zeta k_B T}{\delta t} \delta_{ij}$ [28]. Thus, the mean squared displacement can be written as

$$\langle (x(t) - x(0))^2 \rangle \approx \sum_{i=1}^{N_t} \sum_{j=1}^{N_t} \zeta^{-2} \langle \xi_j \xi_i \rangle \delta t^2 \approx \frac{2k_B T \delta t}{\zeta} N_t = \frac{2k_B T}{\zeta} t. \quad (1.12)$$

Comparing Eqn. 1.12 to Eqn. 1.8, we see the Einstein relation [17],

$$D = \frac{k_B T}{\zeta}. \quad (1.13)$$

It is common to express the inverse friction as the mobility $\mu = \frac{1}{\zeta}$. I will mention the mobility throughout the thesis while avoiding the use of the symbol μ for mobility to avoid confusion with the chemical potential, also called μ . Eqn. 1.13 can be derived through other means [16, 27].

Typically, we are looking at something a little more interesting: interacting particles, external fields, etc. Regardless, we imagine discretizing time and adding up small positional changes that occurred over a time interval [28]. The basic methods behind Brownian dynamic simulations are summarized in Appendix B.

Finally, I connect the Brownian dynamics to a continuity equation, *i.e.*, instead of examining a single random walk, what can we say about the probability of finding the particle at a given location and time? Since a Brownian particle undergoes a random walk, its position is a sum of independent random variables. By the central limit theorem, the distribution of positions is Gaussian [27]. The variance along any given dimension i must be $\sigma_i^2 = \langle x_i^2(t) \rangle = 2Dt$. Thus, the probability density in d dimensions is

$$p(\mathbf{r}, t) = \frac{1}{(4\pi d D t)^{d/2}} e^{-\frac{r^2}{4Dt}}. \quad (1.14)$$

Here, I have assumed that the particle has started at origin; the $t \rightarrow 0$ limit recovers a delta function centered at the origin. This distribution satisfies the diffusion equation

$$\frac{\partial p(\mathbf{r}, t)}{\partial t} = D \nabla^2 p(\mathbf{r}, t). \quad (1.15)$$

We are interested in tracking noninteracting Brownian particles. The single-particle probability distribution and concentration differ by a factor of the particle number N since there are no correlations between particles. We can therefore write the diffusion equation as

$$\frac{\partial c(\mathbf{r}, t)}{\partial t} = -\nabla \cdot \mathbf{j}_{\text{diff}} = \nabla \cdot D \nabla c(\mathbf{r}, t). \quad (1.16)$$

From this, we can extract Fick's law of diffusion [27]

$$\mathbf{j}_{\text{diff}} = -D \nabla c(\mathbf{r}, t). \quad (1.17)$$

The diffusion coefficient is a constant scalar in our derivation because we assumed that the friction coefficient is isotropic and homogeneous. From here, I briefly introduce obstacles and interactions.

1.3 Effects of obstacles

While random walks are useful for describing dynamics of particle in many situations, it is not complete. Particle dynamics can be altered from interactions with either other particles or the environment. In crowded media, obstacles impede tracer motion, *e.g.*, diffusion of macromolecules in a cell [2]. A profound effect of these obstacles is that the random walk can become anomalous [29].

One of the key assumptions in a normal random walk is that steps are attempted at a constant frequency. When this occurs, the MSD is linear in time (Eqn. 1.8), which is referred to as Fickian or normal diffusion. If this assumption is relaxed and the MSD is no longer linear in time [29],

$$\langle r^2 \rangle = 2dDt^\alpha, \quad (1.18)$$

the diffusion is said to be anomalous. Randomly placed obstacles can impede motion and cause a variable step frequency [30, 31]. In biological systems, anomalous diffusion has been measured due to the presence of obstacles [32–34]. Since the early work of Saxton [35], lattice Monte Carlo models have been an important tool for studying diffusion in crowded environments. Obstacles affect the probability to move to a certain location.

While there are myriad lattice models for static obstacles with single-site hard steric repulsion [31, 35], multi-site hard obstacles [36, 37], and surface binding [38, 39], previous work did not address bound motion and soft obstacles. There are several biological systems that suggest bound motion and soft obstacles, *i.e.*, particles and obstacles can occupy the same spatial region [40–44]. The model we developed in [21] studied how bound motion and binding affect tracer dynamics.

Another type of obstacle is a homogeneous distribution of binding sites that a particle can attach to. The binding is controlled by binding kinetics



where T is the concentration of unbound particles, B the concentration of binding sites, and C the concentration of the bound complex. A diffusing particle could bind to the uniform background of binding sites that alter its motion. This was the model we developed to understand how biofilters

select which particles are allowed to pass through [45].

1.4 Effects of interactions and activity

Active matter is collections of interacting particles which are propelled by a nonconservative force. These novel systems illuminate how particle interactions and activity can lead to new properties, such as giant number fluctuations and unusual mechanical responses [15], that are not present in equilibrium systems. We are interested in how microscopic interactions lead to bulk behavior. Introducing interactions and activity to the Langevin equation is straightforward. In a simulation, one can imagine calculating forces on each particle, updating the positions, and analyzing the results. A single simulation, however, was just one possible outcome, *i.e.*, one realization of the noise. To say something about the average behavior, we would have to repeat the simulation many times. Another method would be to evolve a probability density in time, like in the diffusion equation (Eqn. 1.16), and I will refer to these as continuity, continuous, or macroscopic equations.

When evolving the Langevin equation, the corresponding microscopic density of a system of point-like particles is [46]

$$\hat{\rho}(\mathbf{r}) = \sum_{i=1}^N \delta(\mathbf{r} - \mathbf{r}_i). \quad (1.20)$$

This density is an operator since it is only truly meaningful in an integral. The ensemble averaged density describes how the system behaves after averaging over noise,

$$\rho^{(1)}(\mathbf{r}) = \langle \hat{\rho}(\mathbf{r}) \rangle = \left\langle \sum_{i=1}^N \delta(\mathbf{r} - \mathbf{r}_i) \right\rangle, \quad (1.21)$$

where $\rho^{(1)}(\mathbf{r})$ is the one-body density. Typically, the (1) superscript is dropped or it is denoted as $c(\mathbf{r})$, and it is also referred to as the density profile or concentration. The one-body density is the noise ensemble averaged probability of finding a particle at location \mathbf{r} . As N increases, the BD numerics become unwieldy. Solving continuous equations allows us to evolve the dynamics at specified spatial coordinates instead of for all N particles.

A technique for solving the temporal evolution of density is dynamical density functional theory (DDFT) [22–25]. Using DDFT, a continuity equation for the evolution of the one-body

density is expressed in terms of functional derivatives of the free energy \mathcal{F}

$$\frac{\partial \rho(\mathbf{r}, t)}{\partial t} = -\nabla \cdot \mathbf{j} = \nabla \cdot \left[\zeta^{-1} \rho(\mathbf{r}, t) \nabla \frac{\delta \mathcal{F}[\rho(\mathbf{r}, t)]}{\delta \rho(\mathbf{r}, t)} \right]. \quad (1.22)$$

We can interpret the DDFT flux $\mathbf{j}^{\mathcal{F}} = -\zeta^{-1} \rho(\mathbf{r}, t) \nabla \frac{\delta \mathcal{F}[\rho]}{\delta \rho(\mathbf{r}, t)}$ as a concentration $\rho(\mathbf{r}, t)$ times a velocity $\mathbf{v} = -\zeta^{-1} \nabla \frac{\delta \mathcal{F}[\rho]}{\delta \rho(\mathbf{r}, t)}$. The velocity term arises from the gradients of chemical potential $\mu(\mathbf{r}) = \frac{\delta \mathcal{F}[\rho]}{\delta \rho(\mathbf{r})}$.

The nonconservative active force cannot be expressed as a gradient of a chemical potential. However, it can be described by an active flux $\mathbf{j}^D = \rho(\mathbf{r}, t) \mathbf{v}^D$. Our total flux will therefore be given by

$$\mathbf{j} = \mathbf{j}^{\mathcal{F}} + \mathbf{j}^D. \quad (1.23)$$

We can separate the free energy into contributions from ideal gas entropy \mathcal{F}^{id} , interactions or excess \mathcal{F}^{ex} , and external fields \mathcal{F}^{ext} [46],

$$\mathcal{F} = \mathcal{F}^{\text{id}} + \mathcal{F}^{\text{ex}} + \mathcal{F}^{\text{ext}}. \quad (1.24)$$

The ideal gas and external field contributions are known exactly. The crux of DDFT is approximating a functional for the interactions [25].

In this thesis, I will describe how the DDFT framework can be used to solve for the temporal evolution of active systems. I will then apply it to a self-propelled hard needle system [47–52]. I will present novel results including a banding instability and discuss where my work fits into the larger body of work [53].

Chapter 2

Sticky and slippery soft obstacles

The diffusion of macromolecules in crowded environments is generally slowed relative to the uncrowded case, and particles can undergo transient anomalous subdiffusive motion [2]. The motion of lipids or macromolecules within biological membranes can be affected by crowding [3–10] because the membrane contains both macromolecules and inhomogeneities in membrane composition [54,55]. In the cell interior, macromolecules, organelles and other cellular structures can inhibit motion, or in contrast, enhance sampling of non-crowded regions [11]. Biological crowders can also contain interaction sites which further modify the macromolecular motion [56]. The kinetics and equilibrium behavior of interactions between mobile proteins can be modified by crowding [57,58]. The magnitude of the effects of crowding on macromolecular motion and reactions is important to determine the limiting rate of biological processes such as signaling receptor activation.

Although most theoretical work has focused on anomalous diffusion in crowded systems made up of impenetrable obstacles with attractive or repulsive surfaces [31,35,36,38,39], there is growing evidence of the importance of soft compartments and barriers in biological systems. In membranes, lipids may be only partially excluded from lipid rafts or domains. When they do interact, they can still diffuse within them [59–62]. Lipid motion can be hindered, though not stopped, near α -synuclein protein aggregates [63]. For all of these cases, theoretical considerations of a two-dimensional system should include the effects of soft interaction potentials and bound-state mobility.

Inside the cell, intrinsically disordered or low-complexity domains can act as soft obstacles

or wells, with rapid diffusion within the wells. Membraneless organelles spontaneously form from low-complexity domain proteins. They are typically highly dynamic assemblies [40], which show fast intra-particle diffusion times, and allow rapid entry and exit of constituents [41]. Proteins that interact with intrinsically disordered proteins can still diffuse during the binding interaction [42,43]. This effect may be particularly pronounced in the central channel of the nuclear pore complex, which contains a high density of binding sites on intrinsically disordered domains. Recent simulation work suggests that the disordered protein binding pockets can exchange on transport factors [43], providing a clear mechanism for mobility while bound to an obstacle. Particles are weakly excluded from individual disordered protein chains due to the lowering of the polymer chain entropy [44], but are expected to allow other macromolecules to enter, and pass through, the space that they occupy. The increasingly recognized importance of proteins that are intrinsically disordered or contain low-complexity domains (within their assemblies) warrants a more careful consideration of the differences between the previously well-studied models, in which binding immobilizes the bound species, and a model that includes soft interactions and obstacles or barriers in which the bound species may remain mobile.

Motivated by the biological importance of binding interactions which can retain mobility of the bound particle, we studied a minimal model with bound tracer mobility (Figure 2.1). In our model, tracer particles move on a 2D or 3D lattice in the presence of immobile obstacles, to which the tracers can bind. A primary distinction between our model and many others that consider binding or adhesion is that others typically consider adhesion between a tracer and an adjacent hard obstacle in which there is no overlap between tracers and a hard obstacle's core [38,39,64]. Here, obstacles are soft: tracer particles can overlap with obstacles, with an energy penalty (or gain) ΔG upon moving to a lattice site occupied by an obstacle. Unlike previous work modeling lipid rafts, we closely examine the dependence on binding, instead of just pure exclusion or free entry into lipid regions [5].

To understand the effects of bound mobility, we first consider the limits of ‘sticky obstacles’, in which tracers are immobile while bound, and ‘slippery obstacles’, in which tracers are mobile

while bound. We use lattice Monte Carlo methods to explore a range of binding energies and obstacle filling fractions. We also examine the effects of semi-sticky obstacles, *i.e.*, intermediate bound diffusion coefficients, and obstacle size effects. Our work demonstrates how diffusion is altered in a crowded environment comprised of compartments with different properties, such as a cell [65]. Our results demonstrate how binding and bound-state motion independently impact particle dynamics, including long-time normal diffusion and anomalous diffusion. Bound tracer mobility increases the long-time diffusion coefficient, reduces the transient anomalous time, and eliminates caging for all times typically observed above the percolation threshold. These results demonstrate that mobility of bound particles can benefit biological systems by allowing mobility even in highly crowded environments.

2.1 Anomalous diffusion

Fractional or anomalous diffusion has been experimentally measured in cells, using fluorescence recovery after photobleaching [32], fluorescence correlation spectroscopy [33, 66], and single-particle tracking [34]. Anomalous diffusion in crowded environments is typically described by a MSD that is no longer linear in time [29]

$$\langle r^2 \rangle \sim t^\alpha, \quad (2.1)$$

where α is called the anomalous coefficient. The magnitude of α describes the type of diffusion: subdiffusive ($\alpha < 1$), Fickian ($\alpha = 1$), and superdiffusive ($\alpha > 1$). There is a fractional diffusion equation associated with the dynamics in Eqn. 2.1, but we will neglect discussing it further (see [29, 30] for more details).

In a traditional Fickian random walk, steps occur at a fixed interval. In a continuous-time random walk, this assumption is relaxed. The waiting-time before taking a step is sampled from a distribution. A continuous-time random walk in which the mean waiting time diverges, *e.g.*, with a power law waiting-time distribution, results in anomalous diffusion [29, 30].

An inhomogeneous random arrangement of hard obstacles can provide an irregular step rate

that introduces memory [30]. One way of viewing viewing anomalous diffusion of a tracer in the presence of obstacles is by considering the fractal structure of an obstacle cluster [31, 35]. Clusters of random hard objects are fractal over short length scales and homogeneous over larger length scales. On length scales larger than the fractal structure, for which the landscape is homogeneous, the diffusion becomes normal ($\alpha = 1$). The Fickian diffusion constant is a measure of the long time behavior of a tracer diffusing in this homogeneous environment. When $\alpha \neq 1$, a tracer is exploring length scales in which clusters of hard obstacles are fractal [35].

The anomalous coefficient characterizes the non-homogeneity and fractal structure of a local landscape. It does not describe the time it takes to escape an trapping cage; just that there is a possibility that the landscape could trap a tracer. In the $\alpha \rightarrow 0$ limit, a tracer is fully caged.

2.2 Lattice models

Lattice Monte Carlo is a valuable tool for studying diffusion in crowded media. A tracer particle undergoes a random walk on a lattice. Obstacles on the lattice can alter dynamics of the tracer by inhibiting steps, lowering the step attempt rate, etc. The typical procedure is that a random number is generated at a given time step. Based on that number, a particle will attempt a step in a given direction. If there are obstacles present, a move will be accepted or rejected based on the interaction with that obstacle. For example, if an obstacle is impenetrable and a tracer tries to step there, the move is rejected. We can also imagine obstacles affecting the local energy landscape. If there is an energy difference ΔE associated with moving between lattice sites, moves are accepted with a probability based on the Boltzmann factor $P_{\text{accept}} \sim e^{-\beta \Delta E}$ where $\beta = 1/k_B T$.

Our model seeks to build on stochastic lattice-gas models that have been important to understanding tracer dynamics in the presence of immobile and mobile hard obstacles [35], anomalous subdiffusion [31], and effects of binding on diffusion [38]. Saxton showed that the tracer diffusion coefficient drops to zero at the percolation threshold, the critical concentration of obstacles at which a continuous path of vacancies (through which a tracer can move) no longer exists. Above this percolation threshold, diffusion is anomalous at long times. The effects of tracer and obstacle

size [36, 37, 67] and adhesion and repulsion to sites adjacent to obstacles [39] on transient subdiffusion and long-time diffusion have been studied. Extensions to mobile obstacles that interact with each other have demonstrated how obstacle clustering dynamics can influence the diffusivity of tracers [68].

Numerically exact methods for calculating diffusion coefficients using the Nernst-Einstein relation [69, 70] and Markov chains [71] have been implemented as a different approach to analyzing these systems; the Nernst-Einstein approach can lower the computational cost of measuring diffusion coefficients for lattice gases [67]. Protein motion in polymer networks has been studied using random walk and self-avoiding-chain models for immobile [72] and mobile [64, 73] hard chains. Studies of chains with binding sites found that modeling chain dynamics allowed a mapping onto randomly distributed obstacles with an effective volume, and showed how sliding along a defined chain can effect tracer dynamics [73, 74]. Note, this mapping, which amounts to a mean-field approximation of obstacles, is not valid in the limit of static obstacles. In some previous work, the effects of binding and sliding while bound were entangled because both effects were encoded by a single parameter [73, 74]. Domains with different diffusion coefficients and sizes (to model lipid rafts) have been studied, but the analysis only included total or no exclusion although it was noted that binding effects could play a large role [5].

2.3 Model

In our model, tracer particles undergo a random walk on a square lattice and interact with immobile obstacles. The interaction is characterized by a binding free energy; for simplicity, we neglect any additional activation barrier. The characteristic binding free energy change of a tracer that hops from an empty site to an obstacle site is ΔG (in units where $k_B T = 1$). We consider both attractive ($\Delta G < 0$) and repulsive ($\Delta G > 0$) obstacles. We use the Metropolis algorithm [75] to accept or reject candidate binding (probability P_B) and unbinding (probability P_U) events. Each tracer occupies a single site lattice site, but the obstacle size is varied to represent domains of characteristic size. Obstacles are squares with sides of length l_{obst} , measured in units of the lattice

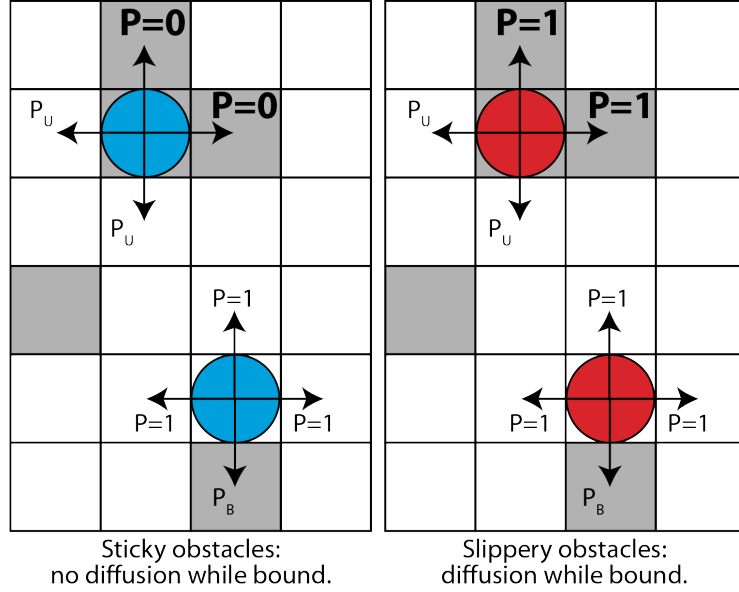


Figure 2.1: Model schematic. Tracers (colored circles) hop on a lattice of empty sites (white squares) and obstacles (gray squares). Tracer binding with a soft interaction potential allows them to overlap with obstacles (top). For sticky obstacles, the only allowed moves of a bound tracer are to empty sites (unbind). For slippery obstacles, tracers can hop to other obstacles while remaining bound. Arrows denote possible moves and P the probability that a given move is accepted.

spacing.

To study the effects of tracer particle motion while bound, we considered the limits of perfectly sticky and slippery obstacles Figure 2.1, as well as the intermediate ‘semi-slippery’ case. In all models, obstacles are soft, so that tracers overlap with obstacles when bound. For sticky obstacles, no hopping between obstacle sites can occur, but tracers can exit an obstacle to an unoccupied site. For slippery obstacles, tracers can hop between adjoining obstacles while remaining bound. In the limit of perfectly slippery obstacles, bound motion is identical to unbound motion: there is no difference in hopping rates between free and bound tracers. For semi-slippery obstacles, we vary the bound diffusion coefficient.

2.3.1 Simulation methods

In our kinetic Monte Carlo scheme, at each time step a tracer attempts a move in a randomly chosen direction. Moves from **empty** → **empty** are always accepted, **empty** → **obstacle** moves are accepted with probability $P_B = \min(e^{-\Delta G}, 1)$, **obstacle** → **empty** moves are accepted with probability $P_U = \min(e^{\Delta G}, 1)$, and **obstacle** → **obstacle** moves are always accepted/rejected if obstacles are slippery/sticky (Figure 2.1); for semi-slippery obstacles, the acceptance probability is $D_{\text{bound}}/D_{\text{free}}$. If a tracer’s move is rejected, it remains immobile for that time step. We assume noninteracting tracers.

Initially, obstacles were uniformly randomly placed on the lattice, at the specified filling fraction, without overlaps. Next, tracers were randomly placed on obstacles and empty sites at their equilibrium occupancy, as determined by the filling fraction of obstacles ν , and binding energy ΔG . The fraction of tracers on obstacles is proportional to the obstacle filling fraction times the Boltzmann factor $\nu e^{-\Delta G}$, while the fraction of tracers on empty sites is proportional to the fraction of empty sites $(1 - \nu)$. The equilibrium fraction of tracers on obstacles of size one is then

$$f_o = \frac{\nu e^{-\Delta G}}{\nu e^{-\Delta G} + (1 - \nu)}. \quad (2.2)$$

Using an initial fraction of tracers bound to obstacles determined from f_o avoids the time required for binding equilibration in the simulations, ensuring that mean-squared displacement measurements are independent of time origin.

We performed 2D simulations with 200 tracers on a 256×256 periodic lattice for $10^5 - 10^{7.5}$ time steps, with a recording interval of 10–100 steps. For each parameter set (determined by filling fraction and binding energy), we averaged over 96 separate obstacle configurations. We varied ν from 0 to 1 and ΔG from −5 to 10. Three dimensional simulations used similar parameters with a $256 \times 256 \times 256$ periodic lattice. In the semi-slippery case, we varied the ratio of bound to free diffusion coefficient $D_{\text{bound}}/D_{\text{free}}$ between 0 (perfectly sticky) and 1 (perfectly slippery) in steps of 0.2, for binding energy $\Delta G = 1, 2, 3, \infty$ and for filling fraction, $\nu = 0.3$ and 0.6. When varying obstacle size, we used square obstacles with the length of a side, l_{obst} , equal to odd values from

1 to 15. When varying obstacle size, we studied repulsive obstacles, to understand how binding affects diffusion for finite repulsion between the previously-studied free binding and pure exclusion limit [5, 36].

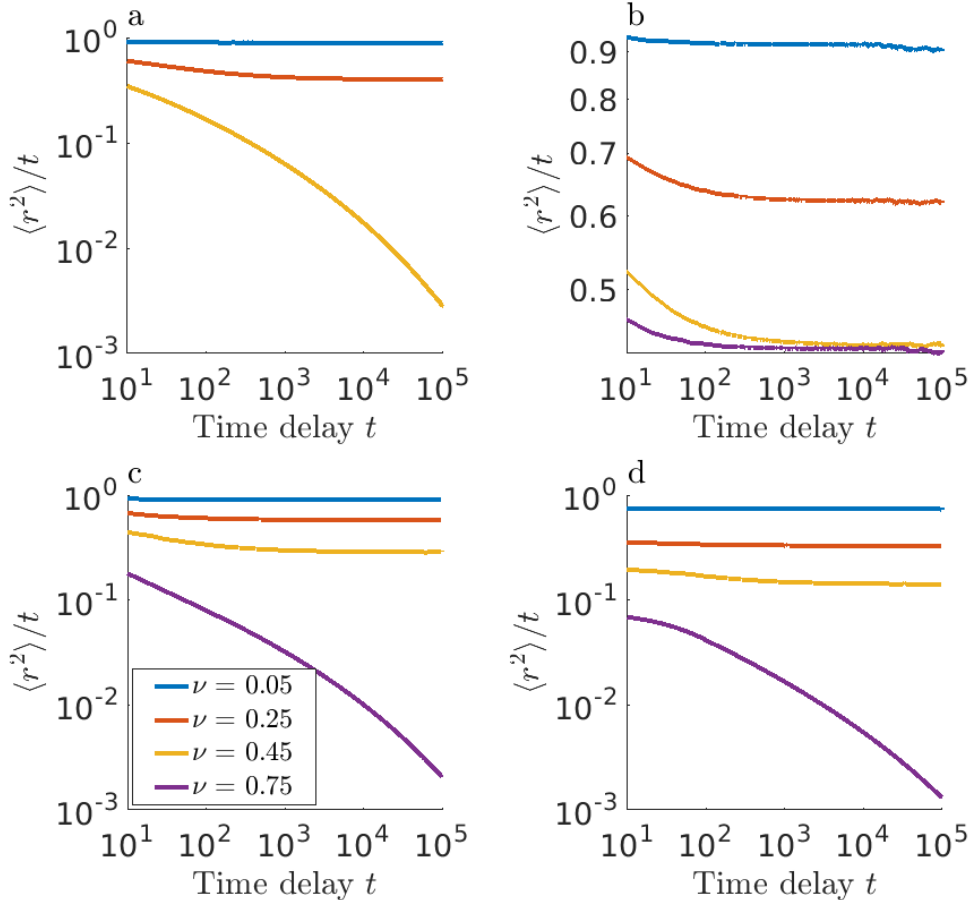


Figure 2.2: Mean-squared displacement $\langle r^2 \rangle$ divided by time delay t as a function of time delay t for (a) impenetrable obstacles, (b) repulsive slippery obstacles ($\Delta G = 2$), (c) repulsive sticky obstacles ($\Delta G = 2$), and (d) attractive sticky obstacles ($\Delta G = -2$). Different colors correspond to different filling fraction ν . Curves with non-zero slope indicate anomalous diffusion, and the horizontal asymptote indicates the long-time diffusion coefficient. Each curve represents an average over tracers, independent time windows, and obstacle configurations.

2.3.2 Trajectory analysis

We determined tracer mean-squared displacement (MSD) as a function of time delay by averaging over all tracers, 100 randomly selected independent time origins, and obstacle configurations. For long time delays for which 100 independent time intervals were not available, we averaged over the maximum number of independent time intervals. As previously mentioned, averaging over time windows improves our statistics; note that the time origins are not unique, since the placement of tracers in their equilibrium binding distribution ensures that there is no initial binding equilibration time. We have verified that there are no aging effects [76, 77], *i.e.*, MSD measurements that depend on simulation time, in our model (data not shown).

We sought to quantify the effects of binding and obstacle filling fraction on tracer mobility. In systems with either purely Fickian diffusion or particular obstacle geometry, the mean-squared displacement grows as a power law in time:

$$\langle r^2 \rangle = 2dDt^\alpha, \quad (2.3)$$

where $\langle r^2 \rangle$ is the ensemble-, time-origin-, and obstacle-configuration-averaged mean-squared displacement, d the spatial dimension, D the diffusion coefficient, α the diffusion scaling exponent, and t the time delay. This fractional diffusion equation has been studied extensively [29], both because it emerges from certain microscopic theories and as a means to quantify anomalous random walks. For hard obstacles, α reflects the non-homogeneity and fractal structure of a cluster. In this case, α can be thought of as a measure of a local landscape, in which obstacles have the possibility of trapping a tracer and introducing memory effects into the system. The value of α does not quantify the time it takes to escape a trapping cage, but $\alpha < 1$ suggests the possibility that the landscape can cage tracers. In the $\alpha \rightarrow 0$ limit, a tracer is fully caged, and the $\alpha \rightarrow 1$ limit represents Fickian diffusion.

However, many systems have more complex dynamics that are not power law. For example, tracer dynamics can be transiently anomalous: subdiffusive on short time scales and Fickian on longer time scales (Figure 2.2b). The dynamics can be quantified using a phenomenological

approximation in which the exponent α is treated as time dependent [31, 36, 37, 67, 71, 78]. Thus, $r^2 \sim t^\alpha$ holds only over particular time scales.

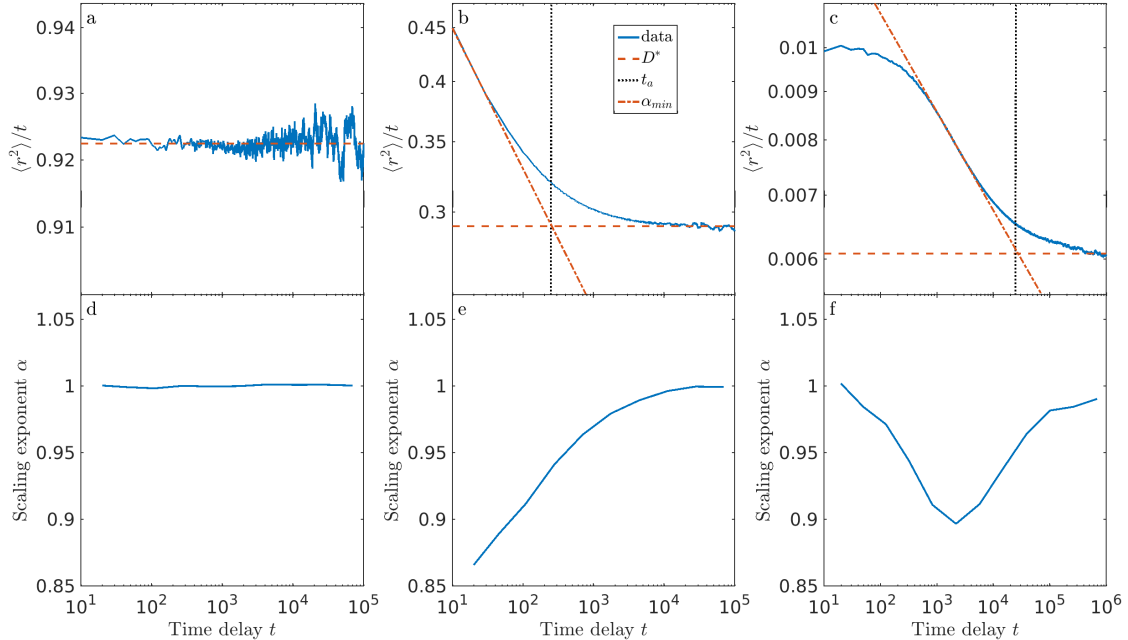


Figure 2.3: Top panel: Illustration of fitting procedure, showing $\langle r^2 \rangle / t$ vs time delay t for simulation data (blue), line fitted to horizontal asymptote (red dashes), line tangent to point of maximum absolute slope of the curve (red dash-dots), and anomalous time t_a (black dots) for different parameters. Bottom panel: instantaneous scaling exponent α vs time delay t . (a, d) Slippery obstacles with $\Delta G = 1$, $\nu = 0.95$: normal diffusion occurs for all measured time. (b, e) Sticky obstacles with $\Delta G = 2$, $\nu = 0.45$. (c, f) Sticky obstacles with $\Delta G = -5$, $\nu = 0.50$.

For non-power law dynamics, we can apply Eqn. 2.3 locally, with a phenomenological, time-varying exponent. Then $\alpha(t)$ is defined by local fitting to the logarithm of $\frac{\langle r^2 \rangle}{t}$:

$$\log \left(\frac{\langle r^2 \rangle}{t} \right) = \log (2dD) + (\alpha(t) - 1) \log (t), \quad (2.4)$$

so that $\alpha(t) - 1$ is the local slope of the $\frac{\langle r^2 \rangle}{t}$ versus t curve on a log-log plot. As seen in figs. 2.2 and 2.3, the instantaneous effective α varies with delay time. Thus, a power law MSD scaling with time, such as can arise from fractional Brownian dynamics, does not encompass the complexity of our crowded diffusion model, as has been found previously [9, 37].

At short times, our model typically exhibits anomalous diffusion. However, under some conditions, the short-time behavior is diffusive, with an intermediate anomalous regime. We defined α_{\min} as the minimum instantaneous value of α (the most anomalous exponent). We characterized the transition between short- or intermediate-time anomalous diffusion and long-time normal diffusion by the time scale t_a , determined as the intersection of the horizontal long-time asymptote of $\frac{\langle r^2 \rangle}{t}$ with a line tangent to the point of the maximum rate of decrease of this curve (Figure 2.3b,c). We found that this transition time could be robustly determined for a wide range of diffusion coefficients and anomalous behavior. We denote t_a the anomalous time. Qualitatively, it is the crossover time from short-time subdiffusion to long-time Fickian diffusion. While α_{\min} characterizes how trapped a tracer is, t_a quantifies how long it takes a tracer to escape a cage and forget the memory effects that the cage introduced to its motion.

We defined the long-time Fickian diffusion coefficient as

$$D = \lim_{t \rightarrow \infty} \frac{\langle r^2 \rangle}{2dt}. \quad (2.5)$$

All diffusion coefficient measurements are expressed in terms of the scaled diffusion coefficient $D^* = \frac{D}{D_0}$, where $D_0 = \frac{l^2}{2d\tau}$ the diffusion coefficient in the absence of obstacles, l the distance between lattice sites (here defined to be 1), and τ the time interval between steps (also set to 1).

In practice, we binned Eqn. 2.4 into (~ 10) separate regions. We locally fit the slope of each region. If the magnitude of the slope was below a certain threshold value, we assumed it was flat. We then took a weighted averaged of all dependent values $\log\left(\frac{\langle r^2 \rangle}{t}\right)$ from the first, *i.e.*, earliest time, flat bin to the end of the simulation to calculate the horizontal asymptote. The scaling coefficient α was found from the bin with the largest negative slope, and t_a was calculated from the intercept of the horizontal asymptote and the fit line from the bin associated with α .

In some cases, we were unable to determine all of D^* , α_{\min} , and t_a . For some parameter sets, the slope of $\frac{\langle r^2 \rangle}{t}$ vs. t on a log-log plot approached a non-zero constant, indicating that diffusion was anomalous over all measured time delays, so that the Fickian diffusion coefficient was not well-defined. For other parameter sets, the $\frac{\langle r^2 \rangle}{t}$ versus t curve did not reach a clear asymptote

during the simulation time. We therefore could not determine D^* , but could measure α_{\min} . When tracer diffusion was normal over all or nearly all measured time delays, neither α_{\min} nor t_a were well-defined, but D^* could be measured.

2.4 Sticky soft obstacles

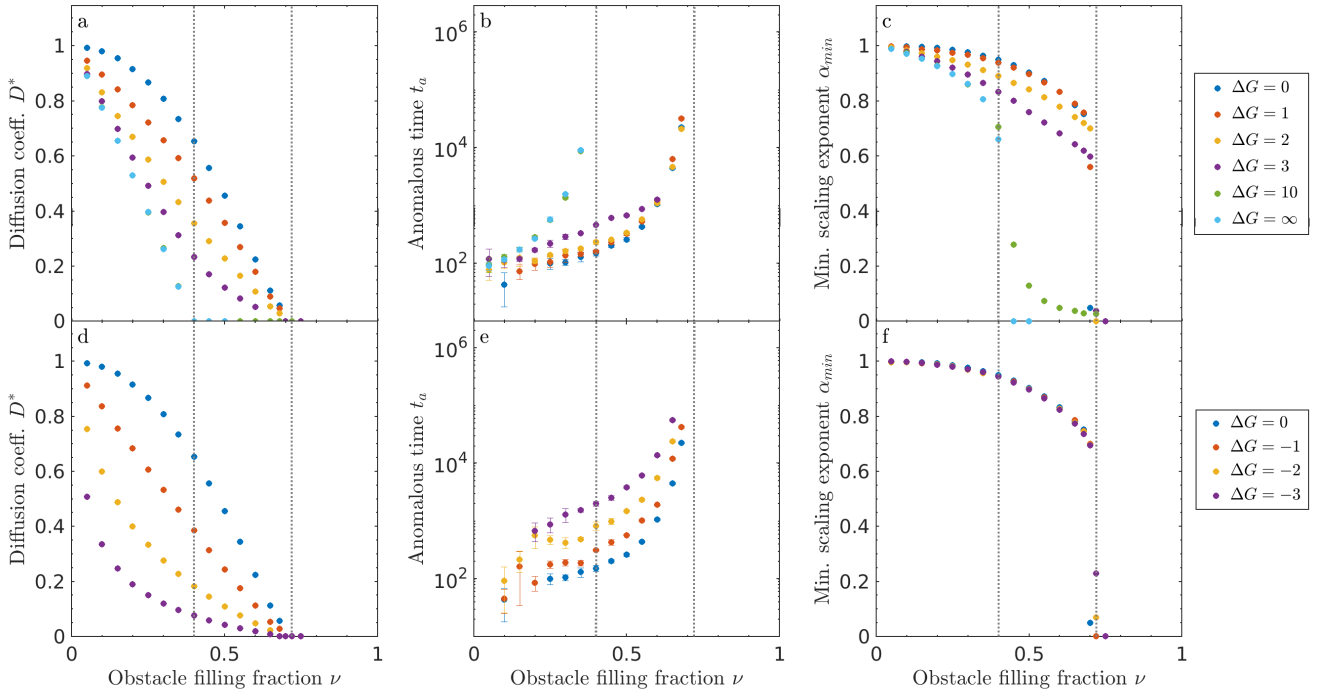


Figure 2.4: Sticky obstacles of size one in 2D. (a, d) Diffusion coefficient D^* , (b, e) anomalous time t_a , and (c, f) minimum scaling exponent α_{\min} as a function of obstacle filling fraction ν for repulsive (top) and attractive (lower) binding energy. Note that points for $\Delta G = 10$ are partially hidden behind $\Delta G = \infty$. The approximate locations of the critical occupancies ν^l and ν^u are indicated with gray dotted lines.

We initially focused on the limit of perfectly sticky obstacles of size 1, to determine the effects of stickiness, filling fraction, and binding energy on tracer motion. We varied parameters over a wider range for the 2D model, with a comparison to 3D results for some parameter sets.

For sticky obstacles, the motion of a bound tracer to an adjacent obstacle is prohibited. This could occur, for example, because the net free energy cost of binding to an obstacle is a result of an

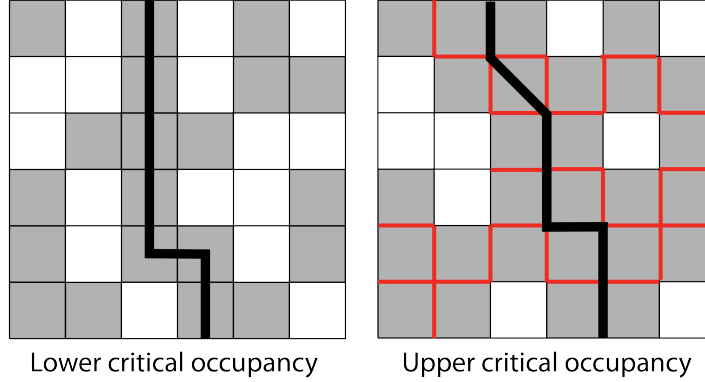


Figure 2.5: The two types of percolation threshold in our lattice model: the lower critical occupancy ν^l (left) and the upper critical occupancy ν^u (right). For the lower critical occupancy, which is the standard percolation threshold, the percolating network is the obstacles. At the upper critical occupancy, the percolating network is the *interface* between two or more obstacles. The barrier to tracer motion is shown as a black line; obstacle-obstacle boundaries which cannot be crossed by a tracer in the sticky model are shown in red. Without binding, tracers cannot pass through the percolating network of obstacles. If they can bind, tracers can ‘hop through’ a single obstacle, with or without bound motion.

attractive binding interaction, with a high free energy barrier to moving to an adjacent site. Here, we consider the limit that the free energy cost of moving to an adjacent obstacle is so large that it approaches infinity. This situation provides an important point of comparison to explicitly test the effects of bound-state diffusion on tracer behavior.

We separately consider repulsive and attractive obstacles (Figure 2.4). Note that we include the case $\Delta G = 0$, that is, where the binding interactions are neither attractive nor repulsive, but still block moves to adjacent obstacles. We define the lower critical occupancy ν^l as the filling fraction at which diffusion is non-Fickian for all time scales for impenetrable obstacles ($\Delta G = \infty$). In the limit of a hard repulsive obstacle, D^* decreases with filling fraction, and approaches zero at the percolation threshold expected for hard obstacles on a square lattice, $\nu^l \approx 0.4$ [79], where t_a diverges [35]. The lower critical occupancy is the percolation threshold, at which there is no longer a continuous path of empty sites (Figure 2.5).

For finite binding free energy in our model, Fickian diffusion can still occur above the perco-

lation threshold ν^l because soft binding allows tracers to ‘hop through’ single obstacles via binding and unbinding. Without soft binding of the type we consider, obstacle percolation would prevent a tracer from moving between vacancy clusters. In other words, tracers that start in an area caged by obstacles are stuck there. With soft binding, tracers that start in a cage can hop onto an obstacle and then hop off into a new vacancy cluster. For soft binding interactions and sticky obstacles, there is an upper critical occupancy $\nu^u \approx 0.72$ at which the long-time diffusion coefficient approaches zero irrespective of binding energy (Figure 2.4). Above ν^u , tracers become caged regardless of the binding kinetics. Therefore, there is a different type of percolating network above the upper critical occupancy: the percolation of the inter-obstacle boundary (Figure 2.5). At the upper critical occupancy, there is a second adjacent obstacle preventing the tracer from ‘hopping through.’ Note that, as expected, the transition time t_a appears to diverge on the approach to the upper critical occupancy (Figure 2.4). We are unaware of a theoretical value for this percolating density, but our results suggest its approximate value is 0.72 in 2D (Figure 2.4). Intermediate repulsive binding energy leads to intermediate behavior, as expected. For strong repulsion, *e.g.*, $\Delta G = 5$, D^* remains small, though clearly non-zero, up to the upper critical occupancy, while t_a monotonically increases until it diverges at ν^u .

Anomalous dynamics appear in the slope of $\langle r^2 \rangle / t$ on a log-log plot. The most anomalous behavior occurs when the scaling coefficient α reaches its smallest value, α_{\min} . We find that α_{\min} decreases with filling fraction and binding energy (Figure 2.4c). Adding more obstacles and increasing the repulsion causes greater hindrance of tracer motion. We note that $\alpha_{\min} \approx 0.7$ near ν^l for impenetrable obstacles, as found previously [5, 31]. Finite repulsive binding energy leads to a smaller exponent ($\alpha_{\min} < 0.7$) than the infinite case at filling fraction above ν^l . For lower values of ΔG , the scaling coefficient does not go to zero at the upper critical occupancy ν^u . Note that the sharp cutoff with filling fraction occurs because we did not collect data past ν^u .

Sticky obstacles with attractive binding interactions show a more rapid falloff in the diffusion coefficient and larger anomalous time (Figure 2.4). The upper critical density $\nu^u \approx 0.72$ is in the same vicinity as for $\Delta G > 0$. The dependence of the diffusion coefficient on filling fraction for

positive and negative binding energy are similar for low magnitude of the binding energy, but the diffusion coefficient falls off more rapidly with filling fraction for highly attractive obstacles. This occurs because an attractive obstacle confines a tracer in one position until it escapes, while a repulsive obstacle only impedes tracer motion for one time step. Therefore, repulsive interactions require several obstacles to transiently confine a tracer, while a single attractive obstacle can cause confinement. Note that we did not include large attractive binding free energy in our analysis.

For attractive obstacles, α_{\min} is independent of binding energy over the range we studied (Figure 2.4). The characteristic time for a tracer to unbind from an attractive obstacle depends on the binding energy, leading to the energy-dependent variation in the anomalous time we observe. However, it is properties of the obstacle arrangement, rather than of binding, which determine the shape of the MSD curve, and therefore α_{\min} . The minimum anomalous exponent occurs when tracers are, on average, confined to a cage formed by inter-obstacle boundaries and single-site wells. Therefore, the minimum anomalous exponent is approximately the same for all binding energies, but varies with filling fraction.

We note that the sticky soft obstacle model studied here does not simply map to impenetrable obstacles at a lower effective obstacle filling fraction, because tracers can ‘hop through’ single obstacles via binding, while never being able to hop between obstacles. Sticky obstacles allow for move attempts (and blocks) that would never be attempted in the impenetrable case.

2.4.1 Sticky soft obstacles in 3D

We extended our study of single-site sticky repulsive obstacles to three dimensions, to determine whether the spatial dimension plays a key role in the tracer behavior (Figure 2.6). The results are qualitatively the same as the 2D model (Figure 2.4). However, in 3D, the lower and upper critical occupancies appear at higher filling fraction: a higher obstacle filling fraction is required to percolate a 3D lattice. The anomalous time is also typically smaller in 3D. For sticky soft obstacles, increasing the spatial dimension does not change the qualitative features of our model, but does shift the critical occupancy and anomalous time.

2.5 Slippery soft obstacles

When obstacles are perfectly slippery, bound tracers can hop to adjacent obstacles without penalty. Our model of perfectly slippery obstacles contains an occupancy-energy inversion symmetry: the dynamics are invariant to changing the filling fraction by switching obstacles and empty sites ($\nu \rightarrow 1 - \nu$) while simultaneously switching the sign of the binding energy ($\Delta G \rightarrow -\Delta G$). In other words, a low filling fraction of attractive obstacles is equivalent to a high filling fraction of repulsive barriers (Figure 2.7).

Slippery obstacles remove the obstacle percolation threshold for all measured binding energy (Figure 2.7). The curves for $\Delta G = 10$ for the repulsive slippery obstacles qualitatively resemble the sticky case (Figure 2.4), because the diffusion coefficient approaches zero for $\nu \approx 0.4$. However, for slippery obstacles, the anomalous time increases, but does not diverge, at the percolation threshold, and then decreases at larger filling fraction. For slippery obstacles with finite ΔG , one can always find a time after which the system displays normal diffusion.

Slippery obstacles lead to non-monotonic behavior: for large enough ν , the diffusion coefficient increases and anomalous time decreases. For high obstacle filling fraction, binding increases tracer mobility, because tracers can hop along the percolating network of obstacles. Similarly, the minimum exponent varies non-monotonically with filling fraction.

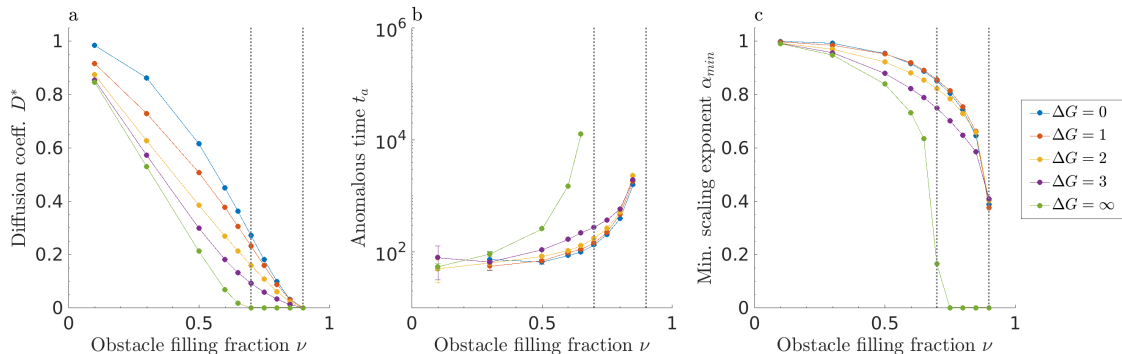


Figure 2.6: Sticky obstacles of size one in 3D. (a) Diffusion coefficient D^* , (b) anomalous time t_a , and (c) minimum scaling exponent α_{\min} as a function of obstacle filling fraction. The approximate locations of the critical occupancies ν^l and ν^u are indicated with gray dotted lines.

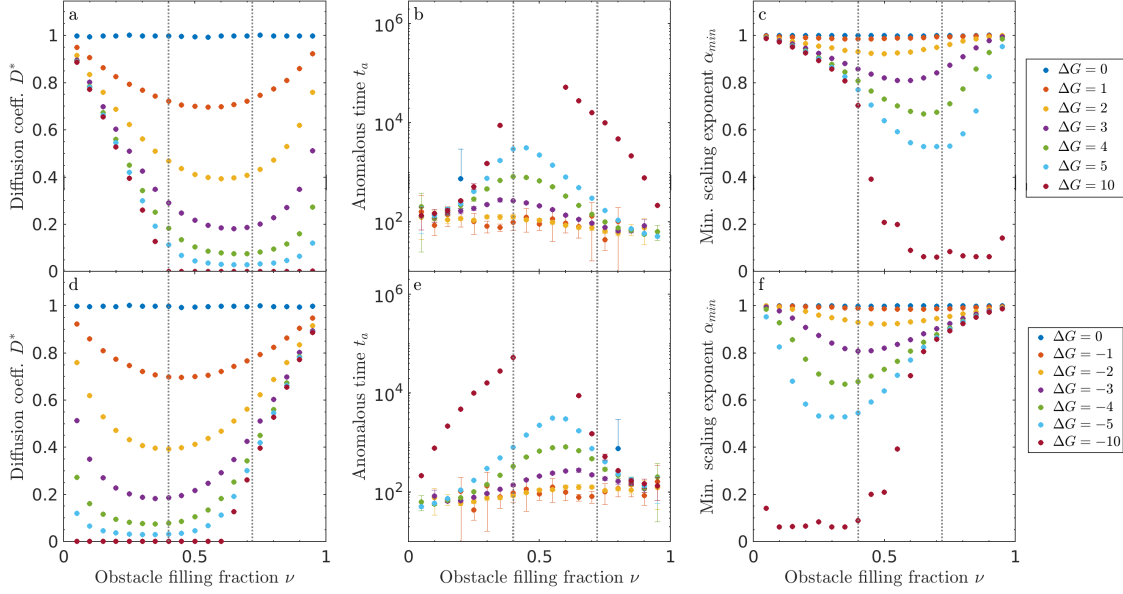


Figure 2.7: Slippery obstacles in 2D. (a, d) Diffusion coefficient D^* , (b, e) anomalous time t_a , and (c, f) minimum scaling exponent α_{min} as a function of obstacle filling fraction ν for repulsive (top) and attractive (lower) binding energy. The approximate locations of the critical occupancies ν^l and ν^u are indicated with gray dotted lines.

2.5.1 Slippery soft obstacles in 3D

As for sticky obstacles, we examined tracer motion with single-site slippery obstacles in three dimensions (Figure 2.8). The results are qualitatively the same as the 2D model (Figure 2.7), with typically smaller anomalous time. The occupancy-energy inversion symmetry noted above for two dimensions also holds in three dimensions. Therefore, the behavior for attractive obstacles can be extracted from Figure 2.8.

2.5.2 Comparison of sticky and slippery obstacles in 2D

The limits of perfectly sticky and slippery obstacles are most similar at low filling fraction (Figure 2.9). In general, slippery obstacles lead to exponents closer to one (less anomalous) than do sticky obstacles, because tracers are not caged by the obstacle-obstacle interface. Even for relatively small values of the binding energy ($|\Delta G| \leq 3$) and intermediate filling fraction, sticky and

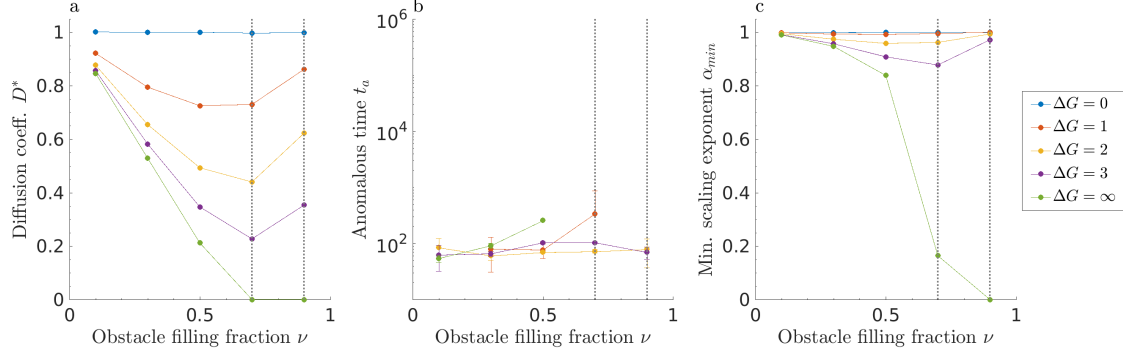


Figure 2.8: Slippery obstacles of size one in 3D. (a) Diffusion coefficient D^* , (b) anomalous time t_a , and (c) minimum scaling exponent α_{\min} as a function of obstacle filling fraction ν . The approximate locations of the critical occupancies ν^l and ν^u are indicated with gray dotted lines.

slippery obstacles lead to significantly different tracer dynamics (Figure 2.9). Slippery obstacles, on which motion can occur for high obstacle filling fraction, allow normal diffusion with coefficients comparable to those for low filling fraction. This effect may be important to explain the rates of a number of biological processes that are diffusion-limited, including transcriptional regulation and nucleo-cytoplasmic transport.

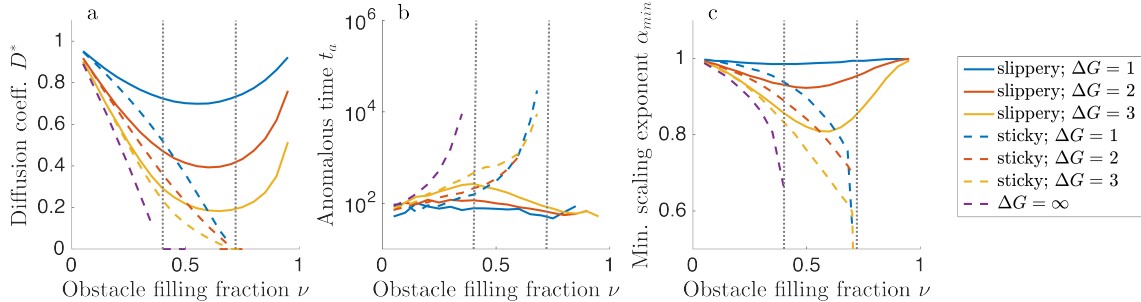


Figure 2.9: Comparison of models with slippery repulsive obstacles (solid lines), sticky repulsive obstacles (dashed lines), and hard repulsive obstacles (purple dashed line). (a) Diffusion coefficient D^* , (b) anomalous time t_a , and (c) minimum scaling exponent α_{\min} as a function of obstacle filling fraction ν . The gray dotted lines indicate the approximate locations of the critical occupancies ν^l and ν^u .

2.6 Semi-slippery obstacles

Having compared the limits of perfectly sticky ($D_{\text{bound}} = 0$) and slippery ($D_{\text{bound}} = D_{\text{free}}$) obstacles, we now study intermediate cases. We varied the bound diffusion coefficient for repulsive binding energy $\Delta G = 1, 2, 3, \infty$ and filling fraction $\nu = 0.3$ and 0.6 . We chose these values to illustrate how our results change from the sticky to the slippery case, as shown in Figure 2.9. For finite binding energy, increasing D_{bound} increases the long-time diffusion coefficient (Figure 2.10). This effect is larger for higher filling fraction and lower binding energy, when tracers spend more time bound. Varying D_{bound} has little effect on the anomalous time at low filling fraction, because t_a is already near the threshold at which we can accurately measure it. However, increasing D_{bound} decreases t_a at higher filling fraction, because tracers can more quickly escape obstacles when their bound diffusion coefficient is larger. Similarly, varying D_{bound} has little effect on α_{\min} at low ν ,

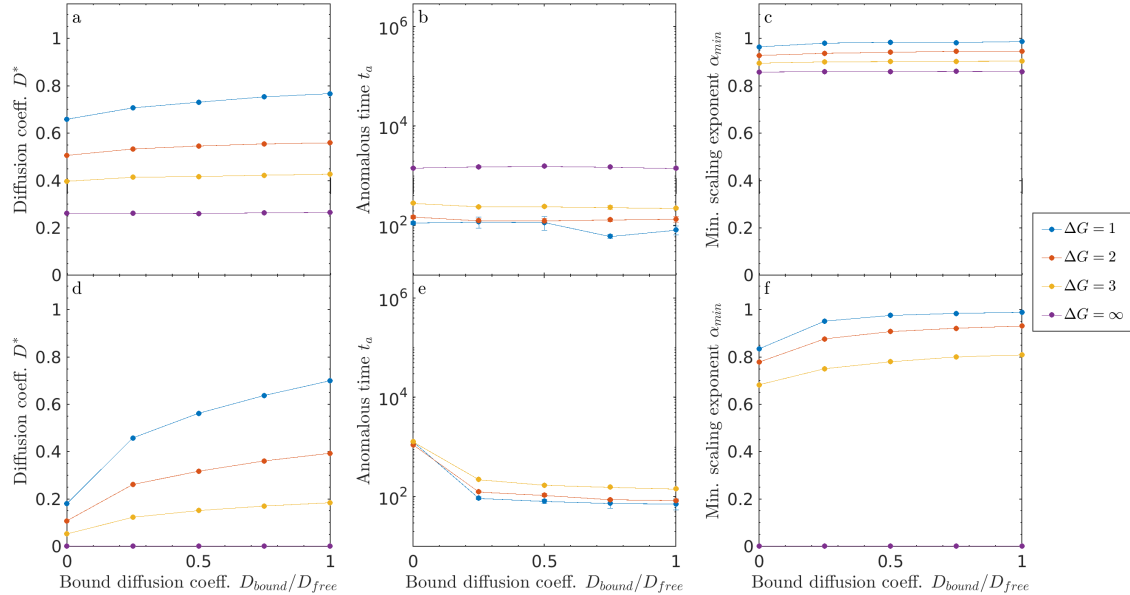


Figure 2.10: Semi-slippery obstacles in 2D. We varied the bound diffusion coefficient from the sticky limit $D_{\text{bound}} = 0$ to the slippery limit $D_{\text{bound}} = D_{\text{free}}$ for single site obstacles. (a, d) Diffusion coefficient D^* , (b, e) anomalous time t_a , and (c, f) minimum scaling exponent α_{\min} as function of D_{bound} for low filling fraction $\nu = 0.3$ (top) and high filling fraction $\nu = 0.6$ (bottom).

but does make diffusion less anomalous at higher filling fraction, because increasing bound mobility reduces tracer caging.

2.7 Varying obstacle size

We varied the length of the obstacles l_{obst} , while maintaining their square shape. Increasing the obstacle size (with filling fraction fixed) clusters obstacles. Since in our model the binding penalty occurs only for **empty** \rightarrow **obstacle** moves, increasing the size of obstacles effectively reduces the number of binding sites: more obstacle sites are interior to obstacles, rather than on their perimeter. For sticky obstacles with $l_{\text{obst}} = 1$, tracers can easily hop through cages, since their bound motion is only blocked by an obstacle-obstacle interface. Increasing the obstacle size guarantees that individual obstacles will contain an obstacle-obstacle interface, which makes it less likely that tracers can hop through neighboring obstacles (Figure 2.11). Increasing obstacle size at fixed filling fraction also increases the typical distance between obstacles. These changes alter obstacle percolation effects: ν^l and ν^u depend on l_{obst} .

2.7.1 Sticky obstacles of varying size

First, we examined tracer dynamics on sticky obstacles of variable size (Figure 2.12). Qualitatively, large sticky obstacles have a soft surface (binding can occur on surface sites, although hops along the surface are still blocked), but a hard core (interior sites are inaccessible). A sig-

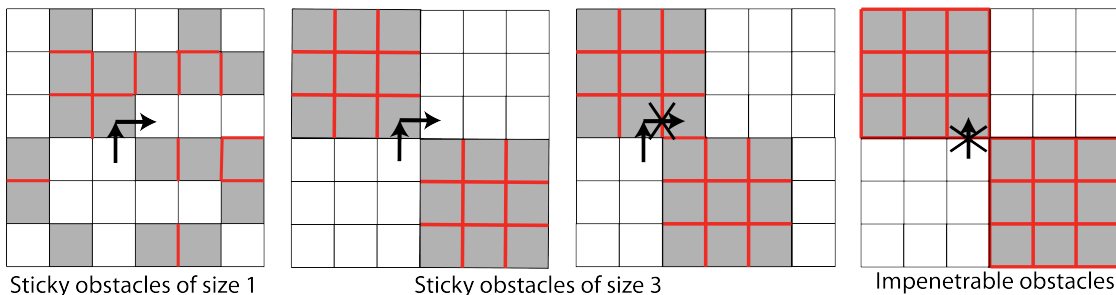


Figure 2.11: Cartoon showing size effects for sticky and impenetrable obstacles. Red lines indicate borders between obstacles that cannot be crossed by a tracer.

nificant change in dynamics occurs when l_{obst} increases above 1. Any obstacle with $l_{\text{obst}} > 1$ is fundamentally different from $l_{\text{obst}} = 1$, because larger obstacles are guaranteed to contain sites with an adjacent obstacle site. Increasing l_{obst} prevents hopping across the interior of any one obstacle, which can hinder tracer motion. The cages are thus more robust. Tracers can still hop across corners, unlike in the case of a purely repulsive interaction (Figure 2.11).

The dependence of tracer dynamics on binding energy changes upon increasing the obstacle size above 1 (Figure 2.12). For size-one obstacles, particles can hop through a single obstacle, and so lower binding energy leads to higher long-time diffusion coefficient. In contrast, with larger obstacles, high binding energy leads to an increased diffusion coefficient. With higher repulsion, a tracer is less likely to bind to the surface of an obstacle where it can get stuck. Thus, for larger obstacles, higher repulsion can facilitate motion.

For $l_{\text{obst}} > 3$, increasing obstacle size increases the cage size, and so the long-term diffusion coefficient and the anomalous time both increase smoothly, in agreement with previous work on

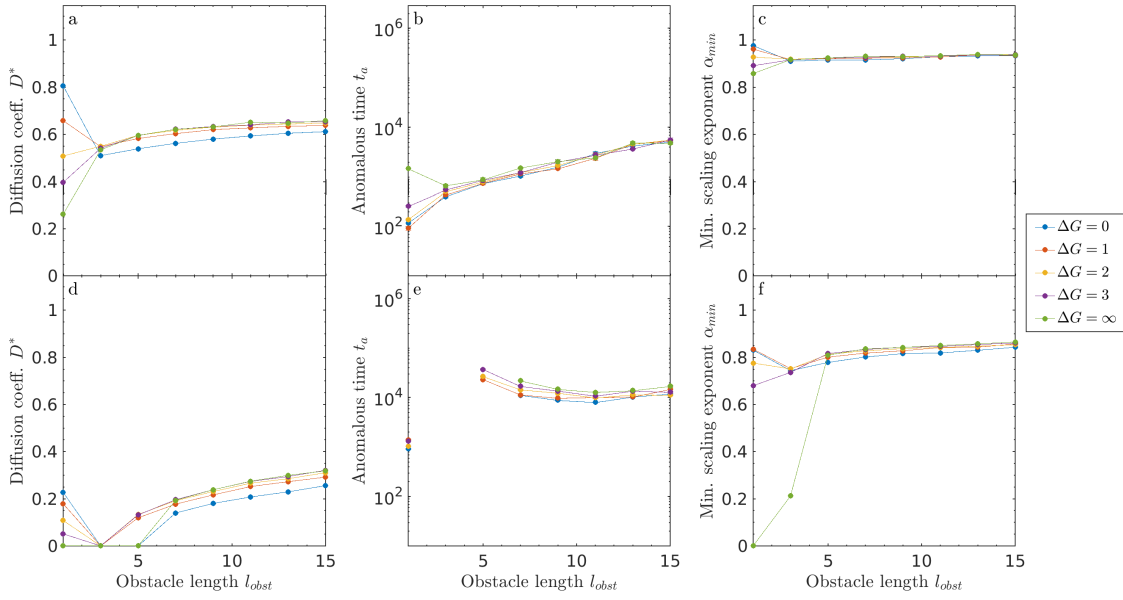


Figure 2.12: Size effects for sticky obstacles in 2D. (a, d) Diffusion coefficient D^* , (b, e) anomalous time t_a , and (c, f) minimum scaling exponent α_{\min} as a function of obstacle filling fraction ν for $\nu = 0.3$ (top) and $\nu = 0.6$ (lower).

impenetrable obstacles [36]. The anomalous time increases with l_{obst} above 3, because the effective cage size increases: tracers take longer to explore a cage to escape. For $l_{\text{obst}} \geq 3$ and small filling fraction, the size dependence is roughly energy independent. The dynamics are dominated by blocked **obstacle** → **obstacle** moves, rather than by the energy dependence of **empty** → **obstacle** moves. For low filling fraction, α_{\min} remains > 0.9 , suggesting that obstacle caging effects are minimal.

Next, we examined a higher packing fraction $\nu = 0.6$, chosen because it is between ν^l and ν^u for size-1 obstacles in 2D. The effects of obstacle size on percolation are significant, leading to larger changes in behavior than for $\nu = 0.3$. As l_{obst} increases, obstacles are on average spaced farther apart, which increases ν^l .

In contrast, the upper critical concentration is more complicated, because now each obstacle contains within it obstacle-obstacle interfaces. The upper critical concentration decreases below 0.6 for $l_{\text{obst}} = 3$, and therefore the dynamics are anomalous at all times; t_a diverges and D^* goes to zero. Above $l_{\text{obst}} = 3$, the upper critical concentration increases with increasing obstacle size. For $l_{\text{obst}} = 5$, $\nu^u > 0.6$, leading to long-time Fickian diffusion. Here, t_a decreases with l_{obst} , because the time required for a tracer to escape a cage is not dominated by the cage size (as it was for low ν), but by the time needed to find a gap between cages. As l_{obst} increases, the gaps become larger on average, lowering the escape time. Overall, above $l_{\text{obst}} = 5$, the behavior is only mildly dependent on either obstacle size or binding energy, making the long-time diffusivity primarily a function of the filling fraction.

2.7.2 Slippery obstacles of varying size

Understanding the effects of variable obstacle size on tracer motion is more straightforward for the case of slippery obstacles, because the difference between edge and interior obstacle sites is eliminated (Figure 2.13). In the perfectly slippery limit, increasing l_{obst} effectively lowers the number of binding sites: tracers experience the binding energy change only when binding to obstacle edge sites, but can move freely through obstacle interior sites. Therefore, D^* and α_{\min} increase with

obstacle size, an effect that is larger for higher filling fraction, because obstacle overlaps at high filling fraction lower the fraction of obstacles that impede motion and cage tracers. In nearly all cases, t_a increases with obstacle size, because the effective cage size grows. The exception occurs for impenetrable obstacles, where increasing l_{obst} increases the size of vacancies between cages, allowing caged tracers to escape more quickly.

2.8 Conclusion

In this chapter, we have studied a lattice model of tracer particles that diffuse and experience crowding due to immobile obstacles. While most previous work has considered hard (impenetrable) obstacles, we consider soft (penetrable) obstacles characterized by a binding free energy that allows tracers to overlap with obstacles. We also consider the effects of varying the tracer mobility while bound, including the limiting cases of ‘sticky’ obstacles (which immobilize bound tracers) and ‘slippery’ obstacles (which allow full tracer mobility), as well as the intermediate regime between

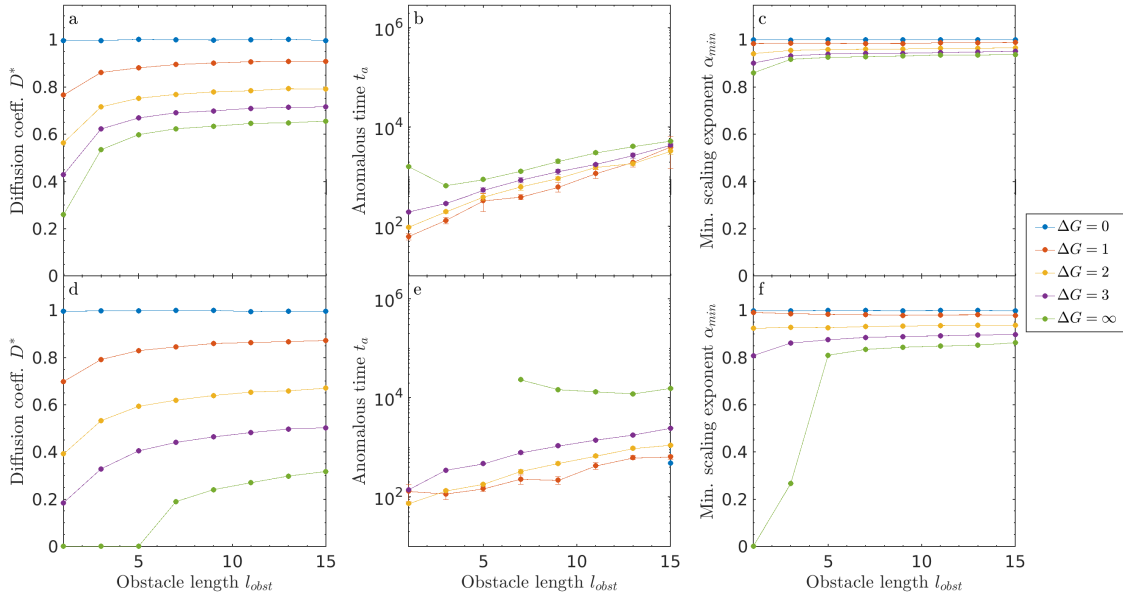


Figure 2.13: Size effects for slippery obstacles in 2D. (a, d) Diffusion coefficient D^* , (b, e) anomalous time t_a , and (c, f) minimum scaling exponent α_{\min} as a function of obstacle filling fraction ν for $\nu = 0.3$ (top) and $\nu = 0.6$ (lower).

the two.

In some cases, diffusion in crowded media leads to dynamics that are anomalous ($r^2 \sim t^\alpha$) with a constant α [2]. However, our system typically does not give a power law dependence of the MSD on time delay; this has been seen by others [9, 37]. As a result, we quantified a long-time diffusion constant (D^*), the timescale on which the systems transitions from anomalous to Fickian (t_a), and the minimum instantaneous anomalous exponent (α_{\min}).

Our results demonstrate the key differences between sticky and slippery obstacles. For sticky obstacles, increasing the obstacle filling fraction decreases the diffusion coefficient and increases the degree of anomalous diffusion. Above an upper critical occupancy $\nu^u \approx 0.72$ in 2D, diffusion becomes anomalous at all times, independent of binding energy. In the sticky case, the minimum anomalous exponent α_{\min} monotonically decreases with filling fraction, because adding obstacles creates more cages in which tracers become transiently confined.

For slippery obstacles, by contrast, tracers always reach normal diffusion after a sufficiently long time; even increasing the filling fraction above the percolation threshold does not eliminate tracer motion. For nonzero binding free energy, we find a novel non-monotonic dependence of D^* on filling fraction: increasing the filling fraction away from zero introduces binding sites that slow tracer diffusion, but for sufficiently high filling fraction, bound mobility allows tracer motion along clusters of obstacles. The anomalous exponent decreases with binding energy magnitude, but varies non-monotonically with filling fraction. For low filling fraction, α_{\min} decreases as more obstacles are added, because binding transiently traps tracers on isolated obstacles. For sufficiently high density, diffusion becomes more normal when tracers hop along clusters of obstacles while bound. For intermediate ‘semi-slippery’ obstacles, we demonstrate that in the crossover from sticky to slippery behavior: D^* , α_{\min} , and t_a vary smoothly. Increasing bound diffusion always makes the diffusion coefficient larger and the diffusive motion less anomalous.

We varied obstacle size to examine how relatively large obstacle domains affect tracer motion in our model. For sticky obstacles, increasing obstacle size above 1 led to a sharp jump in tracer properties. This occurs because larger obstacles always contain interior obstacle sites, which are

inaccessible to tracers in the sticky model. For large obstacles, increasing repulsive binding energy tends to increase the tracer diffusion coefficient, because tracers spend less time trapped in a binding site.

For slippery obstacles, perimeter and interior obstacle sites are both accessible, which means that varying obstacle size has effects that are easier to understand intuitively. The diffusion coefficient and anomalous exponent increase with obstacle size, because larger obstacles lead to a fewer obstacle-empty boundaries. The effect of obstacle size on t_a varied with filling fraction, due to competing effects on increasing cage size and increasing gaps between cages.

Our models separately represent effects of soft interactions (through the binding energy) and bound-state motion (through obstacle stickiness/slippiness). Sticky and slippery obstacles show dramatically different tracer dynamics, even at short time and low filling fraction. Slippery obstacles lead to a diffusion coefficient which varies non-monotonically with filling fraction, with high values at both high and low obstacle density. As the filling fraction increases from zero, tracers are more and more inhibited by obstacles. However, as the obstacle density increases, particles which bind can more easily move between obstacles. This may describe transport factor motion within the nuclear pore complex, where transport factors can slide on the disordered FG Nup [43]. Therefore, biological systems may use soft interactions and slippery obstacles to allow particle diffusion, even in the highly crowded cellular interior.

Our work highlights how soft interactions and bound-state mobility can dramatically change tracer motion. These effects are relevant to biological systems, ranging from membraneless organelles to lipid rafts. Although most previous theoretical work on crowded diffusion has focused on the anomalous exponent, these biological examples highlight the importance of changes in the diffusion coefficient. For example, proteins which do not passage through the nuclear pore complex on biologically relevant time scales (minutes to hours) cannot have biological effects, and so the speed of passage is the fundamentally important biological quantity. The long-time diffusion coefficient varies dramatically in our model between hard obstacles, sticky soft obstacles, and slippery soft obstacles (Figure 2.9). Thus, the effective permeability of obstacles and the degree to which

bound particles can diffuse can be used by cells to tune macromolecular motion.

Chapter 3

Biofilter modeling

The nuclear pore complex (NPC) is a biofilter that blocks certain macromolecules while allowing the passage of others. Binding is crucial: transport factors (TF) that can bind to disordered proteins (FG nucleoporins or FG nups) in the NPC move through rapidly [80]. Other examples of biofilters that facilitate transport of nanoparticles, like proteins and viruses, are the pericellular matrix in cells, the extracellular matrix in tissues, mucus in cells, and synthetic hydrogels [1]. In certain cases, binding can reduce the transport of macromolecules across the filter, which has negative implications for drug delivery, *e.g.*, cancer treatments can bind to mucosal layers [1]. In other circumstances, the role of binding is protective, *e.g.*, mucus trapping viruses and other nanoparticles [81–83]. Binding and bound mobility play a role in selectivity in all these biofilters.

Laura Maguire, Meredith Betterton, Loren Hough, and I developed a general framework to study transport across the NPC, and the model can be applied to other biofilters. The collaboration originally formed to model experimental density profiles of a hydrogel NPC mimic created in the Hough lab. Focus shifted to a theory paper summarized in Ref. [45]. My role was mainly focused on numerically evaluating the model’s continuum equations while Laura Maguire worked on different bound motion mechanisms.

The work in the previous chapter stressed the importance of inhomogeneities that cause anomalous diffusion. In this chapter, we study transport across biofilters by analyzing the bulk-continuum behavior of particle concentration. We assume that obstacles form a homogeneous continuum in which tracers can bind at any given location. Once bound, a tracer may also exhibit

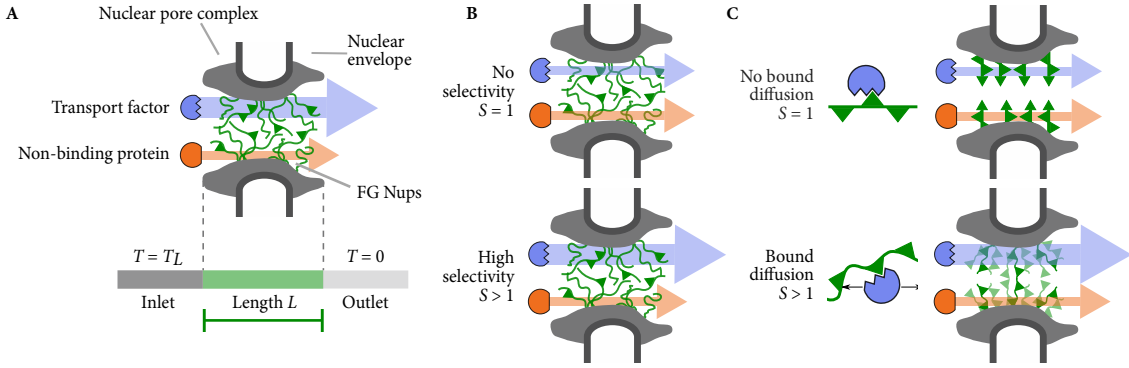


Figure 3.1: Schematics of the nuclear-pore complex and model. (A) The nuclear pore complex (gray) is filled with FG Nups (green polymers) that selectively passage transport factors that bind to FG Nups (blue) while blocking non-binding proteins (red). The central channel of the pore has length L . Protein concentration is high on the left (inlet) and low on the right (outlet). (B) Selectivity quantifies the degree of selective transport through the pore. A non-selective pore with $S = 1$ has the same flux for a transport factor as for a non-binding protein (top). A selective pore with $S > 1$ has a larger flux for a transport factor than a non-binding protein (lower). (C) The bound diffusion coefficient quantifies the mobility of a bound transport factor. A transport factor may be immobile (top) or mobile (lower) when bound. Figure created by Laura Maguire and used with permission.

bound motion.

3.1 Reaction-diffusion model of selectivity in biofilters

In this section, we present a minimal model that can be used to characterize transport across biofilters and apply this tool to study selectivity in the NPC (Figure 3.1). Particles diffuse with coefficient D_F in a one-dimensional gel of length L . The gel is filled with binding sites at concentration N_T with a binding on-rate constant k_{on} , off-rate k_{off} , and dissociation constant $K_D = \frac{k_{\text{off}}}{k_{\text{on}}}$. In the NPC, these binding sites correspond to polymers that some proteins (TF) bind to while others cannot. The free species has concentration T while the bound species has concentration C . The concentration of the inlet and outlet for the free species are fixed to T_L and 0, respectively. Once bound, the complex can diffuse (D_B). Since the binding sites are immobile, the bound species has no-flux boundary conditions. The number of free binding sites is $N(x) = N_T - C(x)$. We assume that particles do not interact with each other. This system is described by the reaction diffusion

equations

$$\frac{\partial T}{\partial t} = -k_{\text{on}}TN + k_{\text{off}}C + D_F \frac{\partial^2 T}{\partial x^2}, \quad (3.1)$$

$$\frac{\partial C}{\partial t} = k_{\text{on}}TN - k_{\text{off}}C + D_B \frac{\partial^2 C}{\partial x^2}. \quad (3.2)$$

The second two terms in Eqn. 3.1 and 3.2 correspond to reaction kinetics while the last term describes diffusion. The bound complex (a particle bound to a site) diffuses, meaning, a bound particle can move across binding sites without unbinding. We chose a parameter set that described the NPC (Table 3.1).

The particle flow into the outlet is given by the flux, $J = -D_F \frac{\partial T}{\partial x}|_{x=L}$. As particles diffuse across the gel, the flux reaches steady state. We define the selectivity as

$$S = \frac{J_{\text{binding}}(t \rightarrow \infty)}{J_{\text{non-binding}}(t \rightarrow \infty)}. \quad (3.3)$$

The selectivity is the flux into the outlet at steady state relative to the flux of a non-binding particle.

A filter is selective if it has the ability to let certain particles through while blocking others.

Parameter	Symbol	Value	Notes
Box length	L	100 nm	[84, 85]
Free diffusion	D_F	$0.012 \mu\text{m}^2/\text{s}$	Calculated from flux [86]
Bound diffusion	D_B/D_F	0–1	Our model [45]
Binding on-rate	k_{on}	10^{-9} Ms^{-1}	Diffusion-limited [42, 87]
Inlet concentration	T_L	$1 \mu\text{M}$	Calculated bulk concentration of $5 \mu\text{M}$ an estimated barrier height of $1.5 k_B T$ [44]
Dissociation constant	K_D	$10^{-2}\text{--}10^3 \mu\text{M}$	[44, 87–91]
Binding site concentration	N_T	$4700 \mu\text{M}$	Estimate of 800 binding sites with 60 nm pore diameter

Table 3.1: The parameters we used to model the NPC.

3.1.1 Linear solution and numerics

The steady state solution in the absence of binding is

$$T(x) = \frac{T_L(L-x)}{L}; \quad J = \frac{D_F T_L}{L}. \quad (3.4)$$

When $D_B = 0$, the unbound species steady state concentration is linear (Eqn. 3.4). When bound motion does not occur, the reaction kinetics do not play a role in selectivity. While kinetics cannot alter the steady state density profile, it can influence dynamics.

When $C(x)/N_T$ is small compared to one, the model is approximately linear. Physically, this corresponds to binding site saturation. A linear model assumes that binding sites can always accept another binding complex. This can lead to unphysical results if the concentration of the bound complex exceeds the concentration of binding sites. At chemical equilibrium,

$$Ck_{\text{off}} = k_{\text{on}}A(N_T - C). \quad (3.5)$$

The linearity condition is then

$$\frac{C(x)}{N_T} = \frac{1}{K_D/T(x) + 1} \ll 1. \quad (3.6)$$

The maximum concentration of the free species occurs at the boundary where $T = T_L$. Therefore, our system is linear when

$$\frac{T_L}{K_D} \ll 1. \quad (3.7)$$

When this condition is met, we can drop the non-linear term in the coupled reaction-diffusion equations. We can solve for the linear solution of the free species

$$T(x) = b + mx + fe^{\lambda x} + ge^{-\lambda x}, \quad (3.8)$$

where $\lambda^2 = k_{\text{off}}(D_F + N_t K_A D_B)/(D_F D_B)$ and b, m, f, g are coefficients fixed from boundary conditions [45].

The coupled reaction-diffusion equations can be written

$$\frac{\partial \mathbf{a}}{\partial t} = L_{\text{op}} \mathbf{a} + W_{\text{op}}(\mathbf{a}), \quad (3.9)$$

where $\mathbf{a} = [T(x), C(x)]'$, $W_{\text{op}}(\mathbf{a}) = [k_{\text{on}}T(x)C(x), -k_{\text{on}}T(x)C(x)]'$ a non-linear function of \mathbf{a} , and the linear operator is

$$L_{\text{op}} = \begin{bmatrix} D_F \frac{\partial^2}{\partial x^2} - k_{\text{on}} N_T & k_{\text{off}} \\ k_{\text{on}} N_T & D_B \frac{\partial^2}{\partial x^2} - k_{\text{off}} \end{bmatrix}. \quad (3.10)$$

We used finite differences to approximate the second derivative

$$\left. \frac{\partial^2 f}{\partial x^2} \right|_{x_i} = \frac{f_{i+1} - 2f_i + f_{i-1}}{\delta x^2}, \quad (3.11)$$

where $f_i = f(x_i)$ is the function evaluated at the i^{th} grid point and δx the grid spacing. We can break up the operators into block matrices that act on T , C , and coupling terms as

$$L_{\text{op}} = \begin{bmatrix} L_{\text{op}}^T & | & L_{\text{op}}^{C \rightarrow T} \\ \hline L_{\text{op}}^{T \rightarrow C} & | & L_{\text{op}}^C \end{bmatrix}. \quad (3.12)$$

The linear operator that acts on T is

$$L_{\text{op}}^T = \begin{bmatrix} 0 & 0 & 0 & \cdots & 0 & 0 \\ \frac{D_F}{\delta x^2} & -k_{\text{on}} N_T - \frac{2D_F}{\delta x^2} & \frac{D_F}{\delta x^2} & \cdots & 0 & 0 \\ 0 & \frac{D_F}{\delta x^2} & -k_{\text{on}} N_T - \frac{2D_F}{\delta x^2} & \cdots & 0 & 0 \\ \vdots & & & \ddots & & \\ 0 & \cdots & 0 & \frac{D_F}{\delta x^2} & -k_{\text{on}} N_T - \frac{2D_F}{\delta x^2} & \frac{D_F}{\delta x^2} \\ 0 & 0 & 0 & \cdots & 0 & 0 \end{bmatrix}. \quad (3.13)$$

Note, the first and last row are zero because of Dirichlet boundary conditions. The operator that acts on C is

$$L_{\text{op}}^C = \begin{bmatrix} -k_{\text{off}} - \frac{2D_B}{\delta x^2} & \frac{2D_B}{\delta x^2} & 0 & \cdots & 0 & 0 \\ \frac{D_B}{\delta x^2} & -k_{\text{off}} - \frac{2D_B}{\delta x^2} & \frac{D_B}{\delta x^2} & \cdots & 0 & 0 \\ 0 & \frac{D_B}{\delta x^2} & -k_{\text{off}} - \frac{2D_B}{\delta x^2} & \cdots & 0 & 0 \\ \vdots & & & \ddots & & \\ 0 & \cdots & 0 & \frac{D_B}{\delta x^2} & -k_{\text{off}} - \frac{2D_B}{\delta x^2} & \frac{D_B}{\delta x^2} \\ 0 & 0 & 0 & \cdots & \frac{2D_B}{\delta x^2} & -k_{\text{off}} - \frac{2D_B}{\delta x^2} \end{bmatrix}, \quad (3.14)$$

where now Neumann boundary conditions are enforced. The coupling matrices are given by

$$L_{\text{op}}^{C \rightarrow T} = k_{\text{off}} \mathbb{I}, \quad (3.15)$$

$$L_{\text{op}}^{T \rightarrow C} = k_{\text{on}} N_T \mathbb{I}, \quad (3.16)$$

where \mathbb{I} is the identity operator. Our numeric scheme evolves the linear term with a Crank-Nicolson step and the nonlinear term with an Euler step,

$$\mathbf{a}_{n+1} = \mathbf{a}_n + \delta t L_{\text{op}}(\mathbf{a}_n + \mathbf{a}_{n+1})/2 + W_{\text{op}}(\mathbf{a}_n) \delta t, \quad (3.17)$$

where n refers to the n^{th} time step. This can be rearranged to give

$$\mathbf{a}_{n+1} = \left(\mathbb{I} - \frac{\delta t}{2} L_{\text{op}} \right)^{-1} \left(\left[\mathbb{I} + \frac{\delta t}{2} L_{\text{op}} \right] \mathbf{a}_n + W_{\text{op}}(\mathbf{a}_n) \delta t \right). \quad (3.18)$$

The numerical integration was implemented in MATLAB. For a computation speed-up, the MATLAB function *mldivide* was used instead of inverting any matrices. We also numerically found steady state solutions of the equation

$$\frac{\partial}{\partial x} \begin{bmatrix} T \\ C \\ T_x \\ C_x \end{bmatrix} = \begin{bmatrix} T_x \\ C_x \\ \frac{1}{D_F} [k_{\text{on}} T (N_T - C) - k_{\text{off}} C] \\ -\frac{1}{D_B} [k_{\text{on}} T (N_T - C) - k_{\text{off}} C] \end{bmatrix}, \quad (3.19)$$

where the x subscript refers to partial differentiation with respect to x , using the differential equation solver *bvp5c* in MATLAB. Whenever we were interested in the dynamics, we solved the full PDE; all of the selectivity measurements were found by numerically integrating the ODE (Eqn. 3.19).

3.2 Selectivity in the nuclear pore

The transient behavior was found for no bound mobility (Figure 3.2A) and bound mobility (Figure 3.2B). Note the different axis limits. Without bound mobility, binding slowed transport, and there was no selectivity. For $D_B > 0$, there was a large increase in particle flux, and particles moved more quickly through the gel.

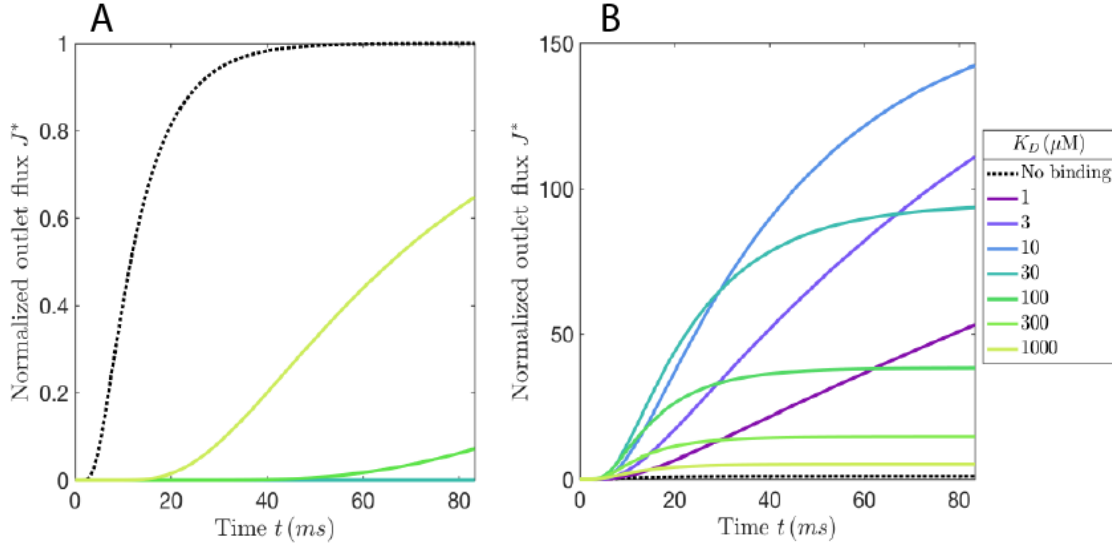


Figure 3.2: Transient flux with (A) no bound motion ($D_B = 0$) and (B) bound motion ($D_B = 1$).

In the model, increasing the bound diffusion coefficient always increases selectivity (Figure 3.3). Varying binding leads to a non-monotonic change of selectivity in the full model (Figure 3.3A). In the weak binding limit $K_D \sim 10^3 \mu\text{M}$, decreasing K_D increases selectivity. As more particles bind, larger gradients in $T(x)$ form, and selectivity increases. As binding increases further

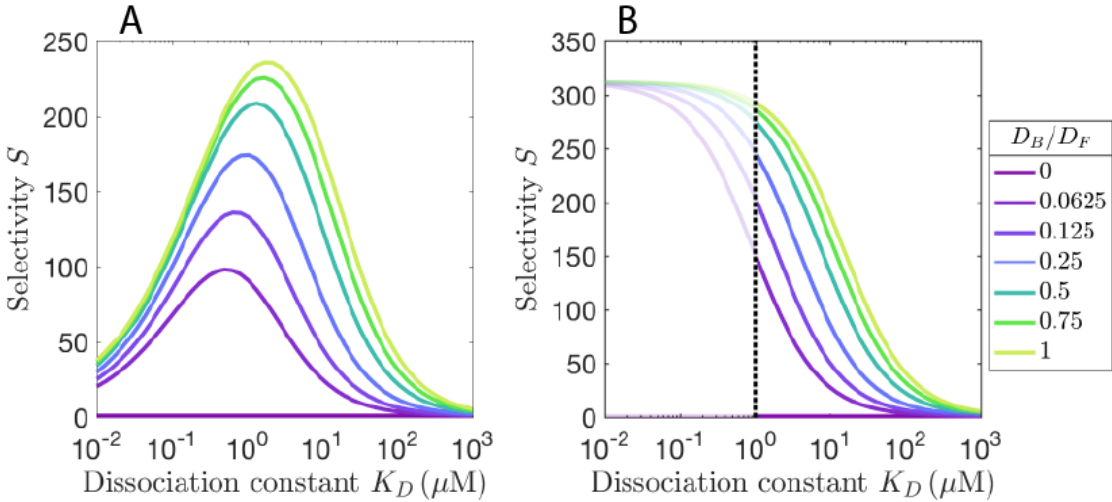


Figure 3.3: Selectivity as a function of diffusion coefficient ratio, with varying dissociation constant using the (A) full model and (B) linear approximation.

$K_D < 1 \mu\text{M}$, the binding sites saturate $N(x) \sim N_T$. Saturation mitigates the inhomogeneity, and therefore, lowers selectivity.

We investigated the non-linear coupling term $T(x)C(x)$ (Eqn. 3.1, 3.2) by comparing the full (Figure 3.3A) and linear solutions (Figure 3.3B). The peak in selectivity in the full model occurs near the linear threshold $K_D \sim 1 \mu\text{M}$. Finally, we found that our model corresponds to experimental selectivity measurements (Table 3.2). The results are for two similarly size proteins: NTF2 (can bind) GFP (cannot bind). Our model captures the range of selectivity values for the NPC.

3.2.1 Comparison to lattice model

How does this system correspond to the previous lattice model (Chapter 2)? In that model, inhomogeneities introduced memory effects that caused anomalous diffusion, and obstacles excluded volume at specific locations. Here, particles can bind anywhere, and obstacles cannot block a specific step. Rather, there is a chance that a tracer will bind at a given time step without changing its position. We can image this as a dual-lattice system: one lattice corresponds to a free state and another corresponds to a bound state. When free, a particle undergoes a random walk on the free-state lattice. There is a probability to bind to the other lattice. When it does, it stays at the same position but moves onto the bound-state lattice. Similarly, it can hop back to the free-state from the bound-state lattice. These binding probabilities correspond to k_{on} and k_{off} , and differing

Method	Cell type	Species	Flux	Selectivity	Notes
OSTR	<i>Xenopus</i>	NTF2	91–123	24–37	[92]
		GFP	3.3–3.8		
OSTR	<i>Xenopus</i>	NTF2	47.3	43	[93]
		GFP	1.1		
Permeabilized cells	HeLa	NTF2	250	125	[86]
		GFP	2		
Model	—	Binding	2–480	1–240	This work
		Non-binding	2		

Table 3.2: Comparison between experimental results for NTF2 and GFP (a similarly-sized non-binding protein) and model predictions. Flux measured in units of molecules per pore per second. Table made by Laura Maguire and used with permission

step rates on the lattices are related to the diffusion coefficients.

Chapter 4

Banding instability of active hard needles

In this chapter, I study how the interplay between activity, a local nonconservative driving force, and interparticle interactions leads to collective motion and self-assembly [15]. I will present a general dynamical density functional theory for studying active systems, and apply the theory to a model system of self-propelled needles.

Active matter refers to collections of interacting particles which can convert an energy source into a propulsive force. These systems exhibit collective motion, self-assembly, nonequilibrium dynamical phases, anomalous fluctuations, and unusual mechanical responses on length scales ranging from microns to meters [15]. Some examples are cytoskeletal filaments and motor proteins [94], animal flocks [95], bacterial swarms [12–14], crawling cells [96], and vibrated granular particles [97–99]. Since the initial work by Vicsek [100], the study of active systems has illuminated features not found in equilibrium fluids, such as collective motion [51, 52, 99, 101–112] and giant number fluctuations [106, 108, 113–116]. Certain active properties such as laning [117–119], phase separated clusters or flocks [120–122], and large density fluctuations [12, 98] have been experimentally realized.

Anisotropic active particles fall into three main classes depending on the polarity of their interactions and activity: polar active (polar activity and interactions), apolar active or active nematic (apolar activity and interactions), and self-propelled (polar activity and apolar interactions) [15, 50].

Self-propelled rods (SPRs) exhibit the hallmark active matter properties while having minimal features: excluded volume interactions and driving. This chapter focuses on self-propelled

hard needles (infinitesimally thin rods) in a 2D dry system (a Brownian heat bath lacking hydrodynamic coupling between particles, but providing random kicks and a drag force acting on the particles) [15].

Previous theoretical work has been of two flavors: phenomenological equations based on symmetries [101, 102] and course-grained models of microscopic interactions [47, 48, 123, 124]. Hydrodynamic theories of self-propelled rods have studied the effects of apolar (nematic) interaction for steric [47] and Yukawa [49] repulsion, activity-modified interactions [48], and a phenomenological polar interaction [110]. These theories predicted instability of the nematic state [47], enhanced diffusion and modified interactions based on activity [48], clustering near confining walls [49], and a mapping of SPRs to active nematics [50]. Furthermore, infinitesimally thin SPRs display rich dynamical phases which include an inhomogeneous band state predicted by theory [47, 50] and demonstrated in simulations [51, 52].

In our work, we study self-propelled hard needles in a 2D dry periodic system using dynamical density functional theory (DDFT) [22–24, 125]. Our model begins with the same microscopic model and approach as Ref. [47]. However, unlike previous work, we solve the full system of equations instead of approximate equations for concentration, polar order, and nematic order. We connect past work to DDFT to clarify some confusion in the literature, describe how the DDFT framework lends itself to studying other active systems, and suggest improvements for the theory. We numerically solve the working equations to find a nematic band at high driving stabilized by inhomogeneous polar order. Our results suggest that mapping SPRs to active nematics [50] is not completely valid, even without a modified interaction from activity as in Ref. [48, 126], because an active nematic cannot possess polar order. Finally, by comparing to simulations, we address the strengths and limitations of our theory.

4.1 Microscopic interactions

Our system contains N infinitely-thin needle shaped particles of length L in a two-dimensional periodic Brownian heat bath of length L_{box} . The particles experience forces from steric interactions,

driving along their director $\hat{\mathbf{u}}$, and random kicks and drag from the solution. Our Brownian heat bath is ‘dry’: there is no momentum conservation (*i.e.*, no hydrodynamic interactions).

4.1.1 Langevin equations of motion

Our simulations directly integrate the microscopic equations of motion. The Brownian dynamics of the i^{th} particle’s position \mathbf{r}_i and orientation $\hat{\mathbf{u}}_i = [\cos \theta_i, \sin \theta_i]$ is described by the overdamped Langevin equations

$$\frac{d\mathbf{r}_i}{dt} = \zeta_i^{-1} \left[-\nabla_i V(\mathbf{r}^N, \hat{\mathbf{u}}^N) + F_D \hat{\mathbf{u}}_i + \xi_i(t) \right], \quad (4.1)$$

$$\frac{d\hat{\mathbf{u}}_i}{dt} = \frac{1}{\zeta_i^R} \left[-\frac{\partial}{\partial \theta_i} V(\mathbf{r}^N, \hat{\mathbf{u}}^N) + \xi_i^R(t) \right], \quad (4.2)$$

where $\mathbf{r}^N = [\mathbf{r}_1, \mathbf{r}_2, \dots, \mathbf{r}_N]$ and $\hat{\mathbf{u}}^N = [\hat{\mathbf{u}}_1, \hat{\mathbf{u}}_2, \dots, \hat{\mathbf{u}}_N]$ are the $2N$ dimensional position and orientation vectors, ζ the spatial friction tensor, ζ^R the rotational drag, V the potential energy, F_D the driving force, and ξ and ξ^R the spatial and rotational noise terms. We have ignored hydrodynamic interactions but have included anisotropy due to the particle geometry in the mobility $\zeta_{\alpha,\beta}^{-1} = \zeta_{\parallel}^{-1} \hat{u}_{\alpha} \hat{u}_{\beta} + \zeta_{\perp}^{-1} (\delta_{\alpha,\beta} - \hat{u}_{\alpha} \hat{u}_{\beta})$ where α, β label Cartesian coordinates. The noise terms are Gaussian-distributed and uncorrelated in time, spatial coordinates, and between particles

$$\langle \xi_{i,\alpha}(t) \xi_{j,\beta}(t') \rangle = 2\zeta_{\alpha\beta} k_B T \delta_{ij} \delta_{\alpha\beta} \delta(t - t'), \quad (4.3)$$

$$\langle \xi_i^R(t) \xi_j^R(t') \rangle = 2\zeta_R k_B T \delta_{ij} \delta(t - t'). \quad (4.4)$$

The potential energy depends solely on excluded volume interactions between particles

$$V(\mathbf{r}^N, \hat{\mathbf{u}}^N) = \sum_{i \neq j} V(\mathbf{r}_i - \mathbf{r}_j, \hat{\mathbf{u}}_i, \hat{\mathbf{u}}_j) = \begin{cases} \infty, & \text{if particles } i, j \text{ overlap} \\ 0, & \text{no overlap} \end{cases}. \quad (4.5)$$

Unlike some previous work [48, 50, 126], we did not include a modified potential due to momentum transfer in collisions in our model; all particle-particle effects are included in the interaction potential. The simulation methods we implemented to solve the equations are described in Ref. [46, 106, 127–131]. All simulations in this project were done by Hui-Shun Kuan and are included in this thesis for completeness.

4.2 Continuum equations

Starting from the microscopic equations of motion (Eqn. 4.1, and 4.2), we are interested in arriving at a continuum continuity equation for the one-particle density $\rho(\mathbf{r}, \hat{\mathbf{u}}, t)$,

$$\frac{\partial \rho(\mathbf{r}, \hat{\mathbf{u}}, t)}{\partial t} = -\nabla \cdot \mathbf{j}(\mathbf{r}, \hat{\mathbf{u}}, t), \quad (4.6)$$

where \mathbf{j} is the flux. The one-body density, or density profile, is the noise ensemble average of the instantaneous microscopic density operator $\rho(\mathbf{r}) = \langle \sum_i \delta(\mathbf{r} - \mathbf{r}_i) \rangle$. The density operator depends on the instantaneous positions of every particle for a given experiment or simulation while the density profile is an average of $\hat{\rho}$ over identical initial conditions but with different realizations of the noise ξ , *i.e.*, one experiment tells you the behavior of $\hat{\rho}$, and averaging over many experiments describes ρ . The density profile is the probability density of finding a particle at location \mathbf{r} pointing in direction $\hat{\mathbf{u}}$ irrespective of the locations of other particles. Unlike solving for the dynamics of the density propagator or a course-grained density, the temporal evolution is deterministic [132].

In our system, there can be fluxes from diffusion, interactions, and driving. We can separate the local driving flux \mathbf{j}^D from the diffusive and interaction flux \mathbf{j}^F . The driving term is given by

$$\mathbf{j}^D = \zeta^{-1} F_D \hat{\mathbf{u}} \rho(\mathbf{r}, \hat{\mathbf{u}}, t). \quad (4.7)$$

To find \mathbf{j}^F in terms of microscopic interactions, we implemented DDFT.

In the introduction of this thesis, we discussed a continuity equation for noninteracting particles, *i.e.*, the diffusion equation. Our goal here is to present a continuity equation for the density of interacting particles starting from microscopic interactions. Arriving at a continuity equation for the N particle phase space density starting from the Langevin equation (*i.e.*, the Smoluchowski equation) is straightforward (see Appendix C). However, this $2N$ dimensional (for 2D) phase space density is not only numerically intractable for large systems, it does not correspond to an experimentally measurable quantity. Dynamical density functional theory allows us to go from the Smoluchowski equation to a closed equation for the one-body density. We will avoid these details here, but the steps are laid out in Appendix D. In the following section, we will present the DDFT

equation and discuss the implementation for our active needle system.

4.2.1 Dynamical density functional theory

Dynamical density functional theory (DDFT) is a technique to obtain the temporal evolution of the one-body density [22–24]. By assuming that correlations out of equilibrium are of the same form as equilibrium correlations but at the nonequilibrium density $\rho(\mathbf{r}, t)$ [24], DDFT casts the temporal evolution of density in terms of functional derivatives of the free energy

$$\mathbf{j}^{\mathcal{F}} = -\zeta^{-1} \left(\rho(\mathbf{r}, \hat{\mathbf{u}}, t) \nabla \frac{\delta \mathcal{F}[\rho]}{\delta \rho(\mathbf{r}, \hat{\mathbf{u}}, t)} \right). \quad (4.8)$$

The free energy can be separated into an ideal gas term and an excess term from interactions, $\mathcal{F} = \mathcal{F}^{\text{id}} + \mathcal{F}^{\text{ex}}$. The ideal gas term which leads to diffusion is exact [46]. To approximate the excess free energy, we used the second virial approximation, which Onsager originally used to predict the isotropic-nematic (IN) transition in three dimensions [133]. This functional describes the equilibrium phase behavior, can be connected directly to microscopic interactions, and is numerically tractable. By truncating the virial expansion at the second term, the approximate excess free energy is

$$\mathcal{F}^{\text{ex}} = -\frac{k_B T}{2} \int d\mathbf{r} d\hat{\mathbf{u}} d\mathbf{r}' d\hat{\mathbf{u}}' F_M(\mathbf{r} - \mathbf{r}', \mathbf{u}, \mathbf{u}') \rho(\mathbf{r}, \mathbf{u}, t) \rho(\mathbf{r}', \mathbf{u}', t), \quad (4.9)$$

where $F_M(\mathbf{r} - \mathbf{r}', \mathbf{u}, \mathbf{u}') = \exp(-\beta V(\mathbf{r} - \mathbf{r}', \hat{\mathbf{u}}, \hat{\mathbf{u}}')) - 1$ is the Mayer function [46]. The second-virial approximation amounts to approximating the direct pair correlation with the Mayer function [46].

For more information on the second virial approximation, see Appendix E.

While ignoring higher order terms works well in 3D, this approximation can lead to dubious quantitative results in 2D [127, 134]. In the absence of driving, the second virial approximation predicts the isotropic-nematic transition at concentration $c = N/L_{\text{box}}^2 = \frac{3\pi}{2} \sim 4.71$ [134] while simulation finds a value of $c \sim 7.25$ [127, 135]. Qualitatively, the second virial only accounts for two-particle interactions. Higher order virial coefficients are more important in two than three dimensions [127] because multiple particle overlaps are more likely at a fixed concentration in two dimensions. However, we believe that this approximation can qualitatively represent the nonequilib-

rium phase behavior of hard needles because it correctly accounts for the phases in the equilibrium system. Note, Eqn. 4.9 cannot account for finite width effects in 2D, and therefore only describes needles (Appendix E).

By plugging in the flux and taking the functional derivatives, we obtain our working equation of motion

$$\begin{aligned}\partial_t \rho(\mathbf{r}, \hat{\mathbf{u}}, t) &= \nabla \cdot \mathbf{D} \nabla \rho(\mathbf{r}, \hat{\mathbf{u}}, t) - \nabla \cdot \zeta^{-1} F_D \hat{\mathbf{u}} \rho(\mathbf{r}, \hat{\mathbf{u}}, t) \\ &\quad - \nabla \cdot \mathbf{D} \rho(\mathbf{r}, \hat{\mathbf{u}}, t) \nabla \int F_M(\mathbf{r} - \mathbf{r}', \hat{\mathbf{u}}, \hat{\mathbf{u}}') \rho(\mathbf{r}', \hat{\mathbf{u}}', t) d\mathbf{r}' d\hat{\mathbf{u}}',\end{aligned}\tag{4.10}$$

where

$$\mathbf{D} = \left[\begin{array}{c|c} \mathbf{D}_T & 0 \\ \hline 0 & D_R \end{array} \right].\tag{4.11}$$

is a block diagonal matrix separated into its translational component $D_T^{\alpha\beta} = D_{\parallel} \hat{u}_{\alpha} \hat{u}_{\beta} + D_{\perp} (\delta_{\alpha\beta} - \hat{u}_{\alpha} \hat{u}_{\beta})$ and rotational component D_R . In principle, activity can influence D_{\parallel} [48] and interactions can introduce a density dependent effect on diffusion [27]. We neglect these effects. For passive infinitely thin rods in the low density limit, $D_{\parallel} = 2D_{\perp} = \frac{2k_B T}{\zeta} = 2D_0$ and $D_R = \frac{6k_B T}{\zeta l^2}$ where ζ is the drag coefficient between the particle and solution [27]. Note that in Eqn. 4.10, there are no phenomenological parameters. Our tunable parameters here are the same as the microscopic model: the driving force and the concentration.

4.2.2 Pseudospectral numerical scheme

To numerically solve Eqn. 4.10, we implemented a pseudospectral method [136]. Complex exponentials form a complete basis for the density profile due to the periodicity of the system. The implemented spectral method involves Fourier transforming the spatial coordinates to momentum space, $\rho(\mathbf{X}, t) \rightarrow \tilde{\rho}(\mathbf{k}, t)$ where $\mathbf{X} = [x, y, \phi]$ and $\mathbf{k} = [k_x, k_y, k_m]$, and integrating in time. All diffusive terms linear in $\tilde{\rho}$ are included in a linear propagator M while the interaction and driving terms are included in a non-linear term ψ . In momentum space, our equation is

$$\frac{\partial \tilde{\rho}(\mathbf{k}, t)}{\partial t} = M \tilde{\rho}(\mathbf{k}, t) + \tilde{\psi}(\mathbf{k}, t).\tag{4.12}$$

We calculate derivatives and convolutions in momentum space and products in real space. We calculate the terms in Eqn. 4.10 at a given time step using the transforms until we get the 1st order ODE in Eqn. 4.12. The numerical integration of Eqn. 4.12 gives

$$\tilde{\rho}(\mathbf{k}, t + \delta t) \approx e^{M\delta t} \tilde{\rho}(\mathbf{k}, t) + \delta t \phi(M\delta t) \tilde{\psi}(\mathbf{k}, t), \quad (4.13)$$

where $\phi(x) = (\exp(x) - 1)/x$. If the propagator is diagonal, we can easily calculate the exponential. In the case where the operator is not diagonal, we used expokit [137] to handle the exponential of the sparse matrix M . In principle, the driving force terms should be put in the linear propagator M . However, it is more computationally efficient to put it in the nonlinear term to make M diagonal. We set $D_{\parallel} = D_{\perp}$ to make M diagonal to further simplify the numerics and increase computational performance for the results in this chapter. We verified that the dynamics are not significantly altered by keeping anisotropies in the equations (results not shown), and this assumption has been used previously [110].

We scale length by rod length L , energy by $k_B T$, and time by the diffusion time $\tau = L^2/D_0$. The box size was fixed at $L_{\text{box}} = 10$, and we use $N_x = N_y = N_{\phi} = 160$ gridpoints. We scale concentration by the average excluded area per particle $c^* = bc = \frac{NL^2}{\pi L_{\text{box}}^2}$. In our scaling scheme, the driving force is equivalent to the Péclet number $\text{Pe} = \frac{L\zeta^{-1}F_D}{D} \equiv F_D$ and the names are used interchangeably. The initial condition was varied, but typically an isotropic or nematic with random plane wave perturbations was used.

4.3 Results

The dynamical density functional equation (Eqn. 4.10) was numerically integrated for varying initial condition, concentration, and driving force. For concentration below the equilibrium IN transition $c^* < c_{IN}$, the system decays to a homogeneous isotropic regardless of driving and initial condition. For $c^* > c_{IN}$, a homogeneous nematic is stable at low activity and high concentration. These match the linear instability predictions due to splay deformations for this specific system [47] as well as a similar behavior in active nematic systems [50, 138].

From $\rho(\mathbf{r}, \hat{\mathbf{u}}, t)$, we compute the local concentration and polar and nematic order parameters

$$C(\mathbf{r}, t) = \int d\hat{\mathbf{u}} \rho(\mathbf{r}, \hat{\mathbf{u}}, t) \quad (4.14)$$

$$P_i(\mathbf{r}, t) = \frac{\int d\hat{\mathbf{u}} \hat{u}_i \rho(\mathbf{r}, \hat{\mathbf{u}}, t)}{C(\mathbf{r}, t)} \quad (4.15)$$

$$N_{ij}(\mathbf{r}, t) = \frac{2 \int d\hat{\mathbf{u}} (\hat{u}_i \hat{u}_j - \frac{1}{2} \delta_{ij}) \rho(\mathbf{r}, \hat{\mathbf{u}}, t)}{C(\mathbf{r}, t)}. \quad (4.16)$$

The degree of alignment at a given location is given by the magnitude of the polar order $P(\mathbf{r}, t) = \|\mathbf{P}(\mathbf{r}, t)\|$, and the largest eigenvalue value of the nematic tensor $N(\mathbf{r}, t) = \max E_\lambda(\mathbf{N})$. We also scaled the local concentration by the average excluded area.

4.3.1 Banding instability

The SPR system has a banding instability for concentration above the IN transition at sufficient driving (Figure 4.1). The band of high concentration and nematic order is surrounded by a low density isotropic gas (Figure 4.2). The band is oriented parallel to the nematic director, and, unlike active nematics which cannot possess a polar state [138], the stability in this system is due to a polar band. The dense nematic band can be understood as a perfectly mixed collection of counterpropagating particles.

Diffusion and interactions generate fluxes that dissolve the band while an inward flux towards

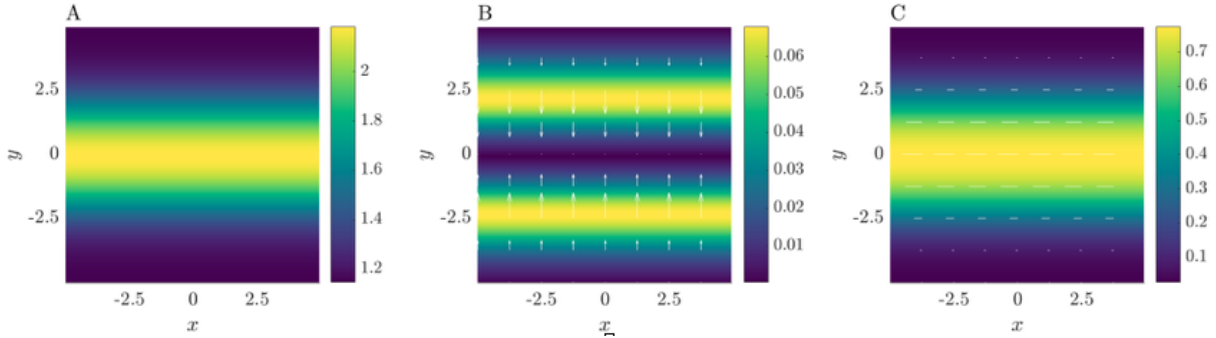


Figure 4.1: (A) Concentration, (B) polar order, and (C) nematic order as a function of position for the steady band state with concentration $c^* = 1.55$ and Péclet number $\text{Pe} = 10$. Magnitude is indicated by color and order parameter director arrows are shown in white. The dense inhomogeneous nematic band is orientated parallel to the local nematic director and is stabilized by inwardly pointing polar edges.

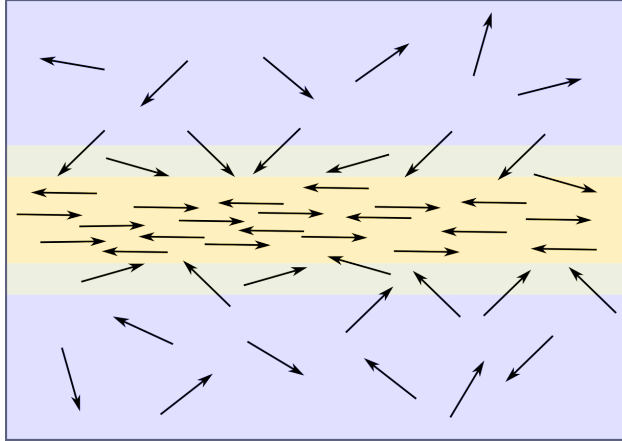


Figure 4.2: Band stability schematic. The dense nematic band corresponds to perfectly mixed counterpropagating needles. The band is supported by a polar edge. The polar order is pointing in toward the band because it is equally likely for a particle to be pointing along either direction of the band. Outside the polar region, there is a sparse isotropic gas.

the band’s center from activity stabilizes the band. Qualitatively, the inward active flux arises because the activity drives rods in the nematic band along the band while it propels rods in the gas in all directions. Thus, it is more likely for a particle to join the band from the gas than to leave. This creates a polar strip outside the band that supports the structure. Another interpretation of this instability is a competition between splay and bend deformation at the boundaries of the band [47]. In our description, this can interpreted as an active flow of particles into a band with equal probability of pointing in either direction along the band.

Above a critical driving and density, shown in dashed red lines in Figure 4.3, the system has a banding instability. At fixed Péclet number, the band peak and width increase as density increases until the band state is no longer stable. For increasing Péclet number, the band peak increase and width decreases. There is no hysteresis or coexistence, suggesting that the band instability is second order.

The homogeneous state is reentrant (Figure 4.3). At low concentration a homogeneous isotropic is stable. When the concentration exceeds the equilibrium IN value, a band state or homogeneous nematic forms depending on the driving amplitude. A band is formed when fluctuations in the nematic order and driving cause an active flow perpendicular to the global nematic

order. If this flow is large enough, it can overcome diffusive fluxes to form a band state. For higher nematic order and low driving, the band is no longer stable because the active flux perpendicular to the director is too small to support a band.

A slice along the inhomogeneous direction shows the band's structure (Figure 4.4). As driving increases, the band becomes more sharply peaked in concentration and order parameter magnitude, and the inward flux towards the band increases. We would expect a higher concentration gradient to balance this effect, so the band gets thinner and more peaked. Since the band thins with increasing driving, one may wonder if there is a critical driving that destroys the band. We found that the numerics became unstable (requiring more gridpoints to prevent a diverging solution) at high driving, so this question remains a topic for further study.

4.3.2 Connection to previous work

In ref. [50], the authors demonstrated that a SPR system can be mapped onto an active nematic. A banding instability was predicted through linear stability analysis and then demonstrated by solving the full hydrodynamic equations of motion [138]. Our results show that this mapping

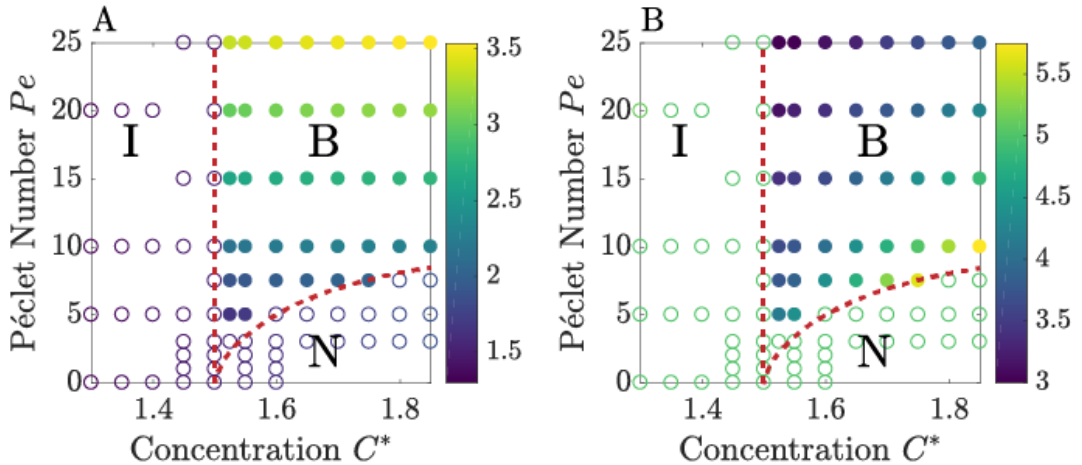


Figure 4.3: Dynamical phase diagram for (A) max band concentration and (B) peak concentration full width half max as a function of Péclet number and concentration. There are three distinct phases: homogeneous isotropic (I), homogeneous nematic (N), and inhomogeneous band (B). The dashed red lines separate the homogeneous and inhomogeneous regions.

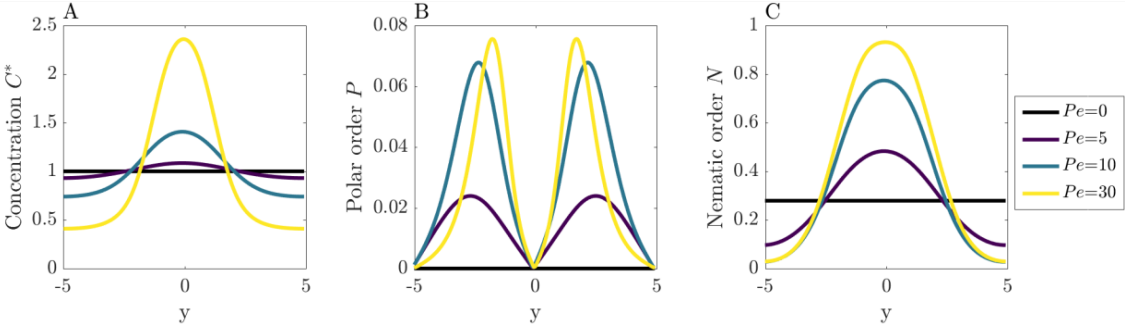


Figure 4.4: A slice along the inhomogeneous direction for (A) concentration, (B) polar order, and (C) nematic order as a function of position for $c^* = 1.55$ and increasing Péclet number. For increasing Péclet number, the band becomes more sharply peaked. The nematic order magnitude is tied to the concentration value while the polar order peak increases with Péclet number to stabilize the band's structure.

is not exact because an active nematic system cannot possess the observed polar band. Therefore, the argument that a band in this system is stabilized by gradients in the nematic order [138] is incomplete. While these systems demonstrate the same qualitative behavior, different mechanisms stabilize the band.

It has been argued that banding is the result of dynamic self-regulation: the density which controls the degree of order is convected by that order parameter [50, 111]. While this is true, it does not provide a microscopic description of stability. By starting with a microscopic model, we can interpret bulk properties in terms of microscopic behavior. In this case, a bulk band is stabilized because activity creates a polar band of particles that produces an inward flux.

4.3.3 Connection to simulations

Simulations of hard self-propelled rods with finite thickness have showed flocking, turbulent-like states, and laning [52, 105]. Our simulations, done by Hui-Shun Kuan, of the infinitely thin rods show flocking (Figure 4.5A) and an apparent band state (Figure 4.5B).

Both the flocking and banding state are highly dynamic. With flocking, several particles form a long-lived collective structure. Flocks are constantly forming and disintegrating; they can collide with other flocks, break up, and form again. The band observed in simulation is also in constant

motion. It appears to be two counterpropagating lanes passing through each other. The center of mass fluctuates; the band will appear, break up, and form again. Unlike the flocking state, there appears to be two definite, although shifting, regions of high and low density in the band state.

The banding state has different behavior than previous laning states [52, 105, 106, 139]. A separation of counterpropagating lanes with finite width occurs from perpendicular flux due to collisions; particles separate into lanes to minimize their collisions [52, 106, 139]. In our system, the rods are infinitesimally thin. Thus, counterpropagating lanes can more easily pass through each and mix without this perpendicular flux. Without this orthogonal motion, a more mixed state of oppositely moving particles should be expected.

We can draw a few distinctions between simulation and DDFT. First, no flocking state is evident in DDFT. One may expect to find a turbulent-like state (fluctuations grow and decay in a seemingly chaotic fashion) in the DDFT solutions, but none exists. The banding state also has differences: it is static in DDFT but highly dynamic in simulation. The nematic order is the consequence of two counterpropagating polar lanes happening to intersect than a stationary (and evenly mixed) nematic.

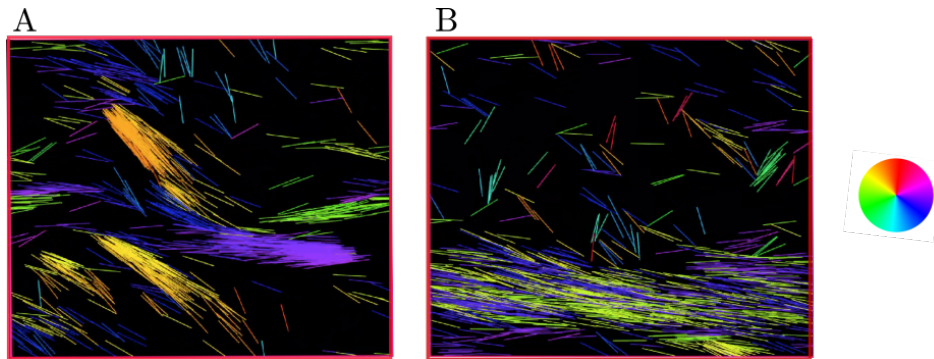


Figure 4.5: Simulation results show two dynamical phases (A) flocking and (B) banding. The flocking state is characterized by dynamic collective clusters that are long lived. The band state is a dense nematic composed of a mixture of counterpropagating particles surrounded by a sparse isotropic gas. Unlike the DDFT results, the simulation band state is highly dynamic. Its center of mass fluctuates and can exhibit fluctuations in local polar along the band, *i.e.*, the two groups of counterpropagating particles are not perfectly mixed. Simulation work done by Hui-Shun Kuan and used with permission.

What mechanisms produce these differences? First, DDFT solves for the ensemble average behavior of a simulation. If we were to consider all possible kicks a flock could receive, we would need to average over all possible paths the flock could take, effectively smearing the flock's density out. However, this doesn't seem to explain everything: there is physics in these flocking states that our functional does not describe. For instance, particles inside a flock get jammed into a glass-like [52] polar state at high density. In DDFT, high density fluctuations quickly decay, *i.e.*, the functional can not accurately describe jamming. Also, DDFT is notorious for not handling fluctuations correctly [125, 140, 141]. For example, DDFT incorrectly characterizes the center of mass fluctuations of a droplet [142].

4.4 Conclusions

We have presented a dynamic density functional theory which demonstrates a banding instability of active hard needles. We presented the framework as a guide to apply this methodology to other active systems where DDFT has been successful in describing the phase behavior of passive systems, *e.g.*, a Gaussian core model [143, 144] or soft shoulder system [145]. Taking the DDFT perspective, rather than considering a theory based on symmetry arguments, can illuminate the strengths and weaknesses of the approximations, and it can be directly compared to a microscopic model.

Using the second virial approximation, we have confirmed the banding instability predicted in previous work [47, 50] by numerically solving the full system of equations. We have laid out a dynamical phase diagram in terms of microscopic parameters, the Péclet number and concentration. Our results are qualitatively similar to active nematics. However, an inhomogeneous band of polar order supports the structure. We have shown how the band peak increases and becomes more compact as driving increases.

We compared the DDFT results to simulations of the microscopic model. The simulation shows rich dynamical phases including flocking and what appears to be an analogous band structure. While we wouldn't expect the same long live flocking states in an ensemble averaged density, *i.e.*, in

a theory for the one body density, one may expect to more evidence of larger density fluctuations. In DDFT at concentrations below c_{IN} , a homogeneous isotropic is the stable state. While a flocking state could be argued to be isotropic and homogeneous when averaging over many simulations, the flocking state has different physical properties like pressure [52] than an isotropic gas. We believe that a functional that can incorporate the physics seen in simulations (like jamming) is the key to a theory that more closely matches simulation results. One such example would be fundamental measure theory [146] although numerically this may be a challenge.

Chapter 5

Validation and additional features of the code

The repository that handled the numerics in the previous chapter is called *ActiveDDFT*. I wrote this package to solve active DDFT equations using pseudospectral collocation for various interactions and external potentials. In this chapter, I focus on additional features and validation of the repository. First, I found the passive isotropic-nematic (IN) transition which validates the code. Next, I studied the effects of coarse-graining, finite-size, and concentration dependent diffusion for the hard needle system. Finally, I present the temporal evolution of the density profile for noninteracting particles in a harmonic well. I look at this particular system because there is an analytic solution [27], and it was used in the microscopic binding model in our paper [45].

5.1 Isotropic-nematic transition and numerical analysis

To validate the code, we studied the isotropic-nematic transition for passive hard needles. The IN transition is second order and occurs at $c^* = 1.5$ in 2D [134]. We measured the steady state global nematic order parameter magnitude, $N = \langle N(x, y) \rangle$, as a function of concentration (Figure 5.1). We found that a homogeneous isotropic is stable for $c^* < 1.5$. At higher concentrations $c^* > 1.5$, a homogeneous nematic is stable. Reproducing equilibrium results validates our model.

5.2 Concentration dependent diffusion

In the previous chapter, we took the dilute limit for the diffusion coefficients. However, diffusion can be slowed by crowding effects. For thin rods [27, 124, 147, 148], this effect is dominant

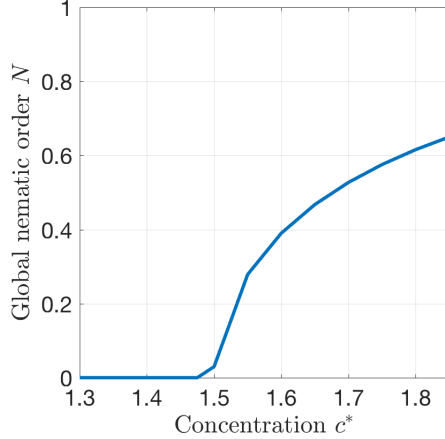


Figure 5.1: Nematic order as a function of concentration in the absence of driving. The isotropic-nematic transition occurs at $c^* = 1.5$. The global nematic order parameter magnitude is the average of the local nematic order $N = \langle N(x, y) \rangle$. The system was homogeneous at all concentration.

in the perpendicular

$$D_{\perp}(\mathbf{r}) \simeq \frac{D_{\perp}^0}{[1 + c(\mathbf{r})/C_{\perp}]^2}, \quad (5.1)$$

and rotational

$$D_r(\mathbf{r}) \simeq \frac{D_r^0}{[1 + c(\mathbf{r})/C_r]^2}, \quad (5.2)$$

diffusion coefficients where C_r, C_{\perp} are constants of order 1 and $c(\mathbf{r})$ is the local concentration. The parallel component is essentially unaffected by crowding [124], and its scaling with concentration is given elsewhere [147, 148].

We studied the effects of nonlinear concentration dependent diffusion on constructed flock states. Our initial state was a homogeneous isotropic with an additive Lorentzian perturbation. We set the width of the Lorentzian to be 1 in x, y , and ϕ . We investigated the effects of diffusion for small (Figure 5.2) and large (4 times the magnitude of the small) perturbations (Figure 5.3). We show the concentration and polar order for normal diffusion (top panel) and nonlinear diffusion (bottom panel). Both cases start with the same initial condition, and time increases from left to right. For all simulations, we set $c^* = 1.45$ and $\text{Pe} = 10$. We exaggerated the effects of differing diffusion coefficients by setting $C_r, C_{\perp} = 0.1$ in the nonlinear case. Normal diffusion refers to the dilute limit.

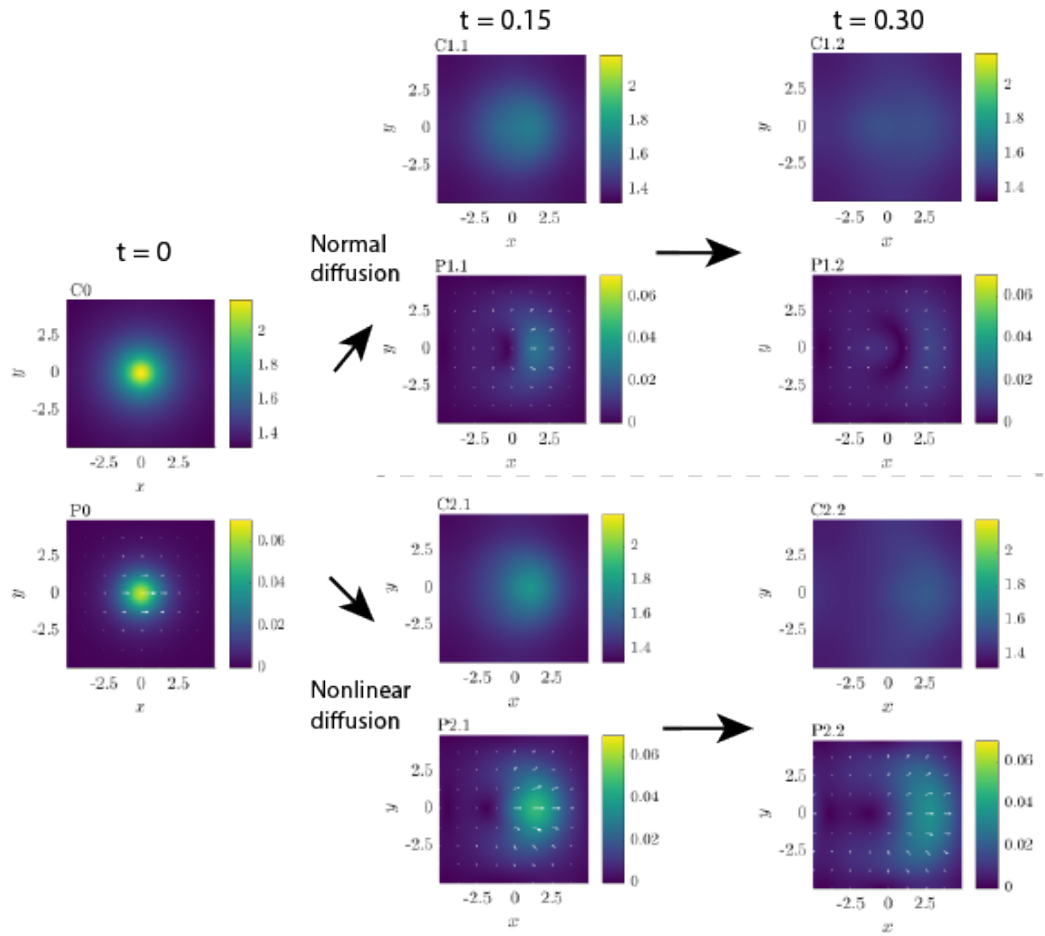


Figure 5.2: The nonlinear concentration dependent diffusion effects on a small amplitude Lorentzian perturbation flock state ($c^* = 1.45$ and $\text{Pe} = 10$). The concentration (C^*) and polar order (P^*) are shown at different times for normal diffusion (top) and nonlinear diffusion with $C_{\perp,r} = 0.1$ (bottom). Time progresses from left to right, and both cases start with the same initial condition. The titles refer to: CO/P0 concentration/polar order at $t = 0$, C1.1/P1.1 concentration/polar order for normal diffusion at $t = 0.15$, C2.1/P2.1 concentration/polar order for nonlinear diffusion at $t = 0.15$, C1.2/P1.2 concentration/polar order for normal diffusion at $t = 0.30$, C2.2/P2.2 concentration/polar order for nonlinear diffusion at $t = 0.30$. The flock dissipated faster with normal diffusion. The final state for both systems was a homogeneous isotropic.

For small perturbations (Figure 5.2), the flock with normal diffusion disintegrates faster than the nonlinear case. The flock breaks up because rods on the edge quickly rotate away from the center and leave the cluster. Since the rotational diffusion is smaller for the nonlinear diffusion, this effect is minimized, and the flock is more stable.

For larger perturbations (Figure 5.3), the nonlinear case behaves qualitatively the same as for

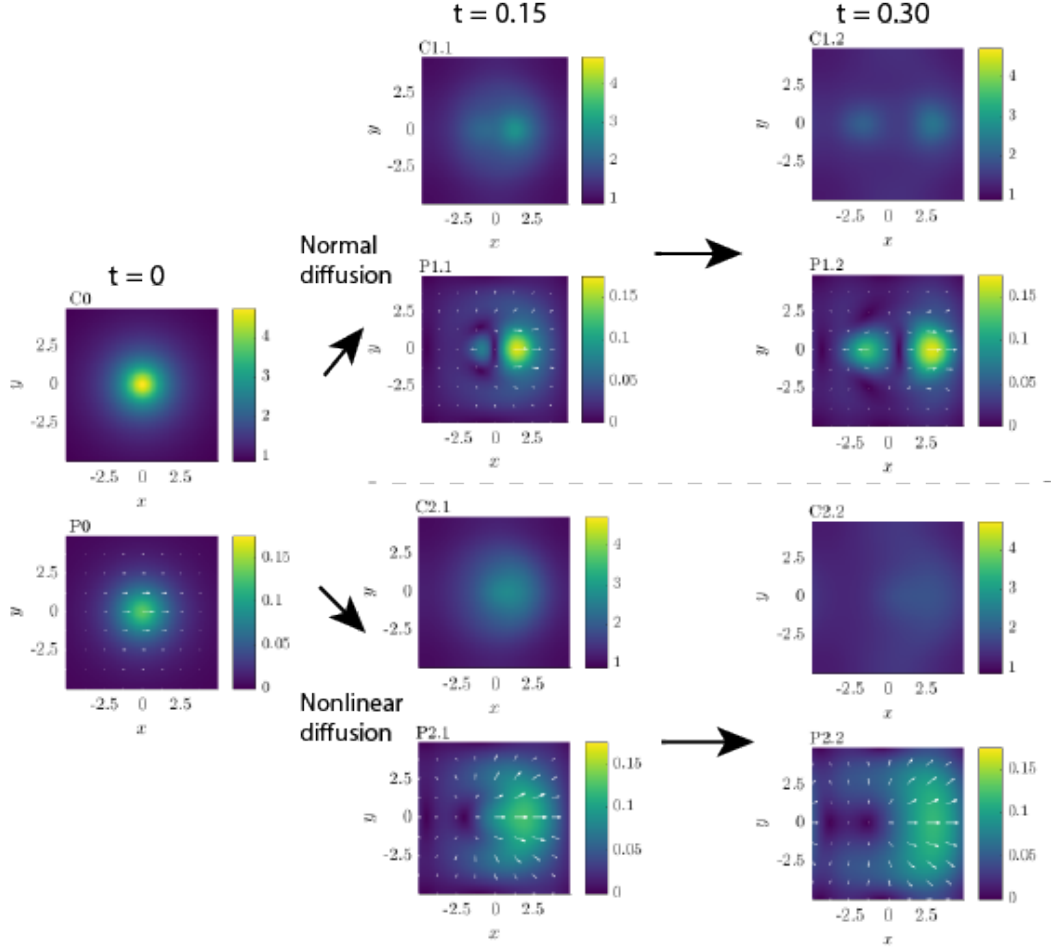


Figure 5.3: The nonlinear concentration dependent diffusion effects on a large amplitude Lorentzian perturbation flock state ($c^* = 1.45$ and $\text{Pe} = 10$). The concentration (C^*) and polar order (P^*) are shown at different times for normal diffusion (top) and nonlinear diffusion with $C_{\perp,r} = 0.1$ (bottom). Time progresses from left to right, and both cases start with the same initial condition. The titles refer to: CO/P0 concentration/polar order at $t = 0$, C1.1/P1.1 concentration/polar order for normal diffusion at $t = 0.15$, C2.1/P2.1 concentration/polar order for nonlinear diffusion at $t = 0.15$, C1.2/P1.2 concentration/polar order for normal diffusion at $t = 0.30$, C2.2/P2.2 concentration/polar order for nonlinear diffusion at $t = 0.30$. For nonlinear diffusion, the flock slowly spread out as it traveled. For normal diffusion, there was an additional flock propagating in the opposite direction of the initial polar order. The final state for both systems was a homogeneous isotropic.

small perturbations. However, the normal diffusion system behaves differently; two counterpropagating flocks form. This is because the center of the flock is at high concentration and, therefore, wants to form a nematic. Since the rods are free to rotate even at high density (which is not physical), we get a nematic in the center of the flock. Thus, we get two counterpropagating flocks

along the nematic director. These flock results provided us with evidence that the functional was not encapsulating the physics seen in simulations. In jammed flocks, rods should not be free to rotate. Even with a modified diffusion coefficient, there was no flocking state in DDFT.

5.3 Effects of course-graining

The dynamical density functional theory equation (Eqn. 1.22) describes the temporal evolution of the ensemble averaged density. Typically in simulation or experiment, a course-grained density $\bar{\rho}$ is measured by averaging the microscopic density over some time or spatial window [132].

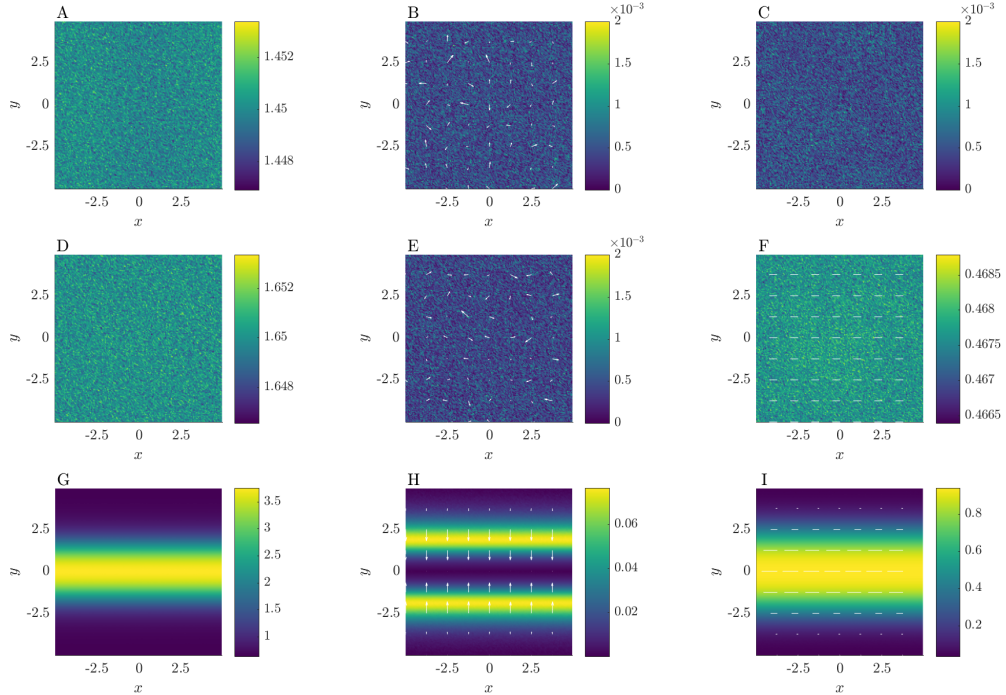


Figure 5.4: Snapshots of the concentration and order parameters showing the effects of course-graining on the three active needle phases. For all panels, the noise strength is $\Delta = 1$. Top panel: (A) concentration, (B) polar order, and (C) nematic order for a homogeneous isotropic with $c^* = 1.45$ and $Pe = 0$. Middle panel: (D) concentration, (E) polar order, and (F) nematic order for a homogeneous nematic with $c^* = 1.65$ and $Pe = 0$. Bottom panel: (G) concentration, (H) polar order, and (I) nematic order for a band state with $c^* = 1.65$ and $Pe = 30$.

The dynamics of the course-grained density are given by [110, 132, 149]

$$\frac{\partial \bar{\rho}(\mathbf{r}, \hat{\mathbf{u}}, t)}{\partial t} = \nabla \cdot \left[\bar{\rho}(\mathbf{r}, \hat{\mathbf{u}}, t) \nabla \frac{\delta \mathcal{F}[\bar{\rho}(\mathbf{r}, \hat{\mathbf{u}}, t)]}{\delta \bar{\rho}(\mathbf{r}, \hat{\mathbf{u}}, t)} + \cdot \zeta^{-1} \sqrt{\bar{\rho}(\mathbf{r}, \hat{\mathbf{u}}, t)} \boldsymbol{\xi}(\mathbf{r}, \hat{\mathbf{u}}, t) \right], \quad (5.3)$$

where $\boldsymbol{\xi}$ is a random vector field with properties

$$\langle \boldsymbol{\xi}(\mathbf{r}, \hat{\mathbf{u}}, t) \rangle = 0 \quad (5.4)$$

$$\langle \xi^l(\mathbf{r}, \hat{\mathbf{u}}, t) \xi^m(\mathbf{r}', \hat{\mathbf{u}}', t') \rangle = 2k_B T \zeta \Delta \delta_{lm} \delta(\mathbf{r} - \mathbf{r}') \delta(\hat{\mathbf{u}} - \hat{\mathbf{u}}') \delta(t - t'), \quad (5.5)$$

where Δ is the effective strength of the noise [110]. There has been a bit of confusion in the literature in regards to this noise term (clarified in Ref. [132]). Random fluctuations are inherent to the dynamics of the microscopic density operator, and therefore, its evolution is stochastic. The ensemble averaged density, however, is an average over all noise realizations and therefore, deterministic. Noise is the source of diffusion. The course-grained density is an incomplete averaging of all possible noise fluctuations. Thus, its evolution is stochastic [132]. The term noise strength, as mentioned in [110], is misleading. Including a noise term in 5.3 is not a more rigorous consideration of noise; it means that we are dealing with a course-grained density and not the ensemble averaged density. Furthermore, this noise strength is a measure of the degree of course-graining

$$\Delta = \frac{\tau_0}{\tau}, \quad (5.6)$$

where τ_0 is a some characteristic microscopic time scale and τ the characteristic course-graining time scale [132]. Note that in the long time average limit ($\tau \gg \tau_0$) the noise term goes to zero, and we recover the DDFT Eqn. 1.22 from Eqn. 5.3.

I studied the effects of course-graining on the three steady state phases of the active needle system: isotropic, nematic, and band (Figure 5.4). Note that the color scales were intentionally set to different limits to show the fluctuations from noise (Eqn. 5.3). For all cases, the fluctuations are constantly varying with time. However, the general structure of the three states in unaltered.

5.3.1 Comparing simulation to DDFT

To compare DDFT and simulations, one must average over many simulations [25, 140, 144]. Each simulation must begin with similar initial conditions, *i.e.*, the initial positions of all particles are sampled from the initial density $\rho(\mathbf{r}, t = 0)$ for each simulation. The ensemble averaged density at a given time t is the average over all microscopic densities from simulations at t .

Given how rapidly the density fluctuations traveled in the active needle simulations, one could image that averaging over many simulations could smear out the flocking dynamics in DDFT. For example, consider running many simulations of a single flock. The flock travels as a collective structure for a long time in any given simulation. However, on average, the density would spread out because the flock has equal probability to turn left or right. With many flocks, averaging over several simulations may cause the density to appear homogeneous but with large fluctuations. We believe this effect contributed to the absence of flocking in DDFT. However, as mentioned in the previous chapter, there is physics the functional cannot capture. The functional approximation is probably the most significant reason why flocking does not occur in the DDFT calculations.

It is natural to wonder why DDFT can show crystallization [145, 150, 151] if a homogeneous liquid is equally likely to crystallize at any position, *i.e.*, the free energy minimum is invariant under translations of the entire crystal. In DDFT, a crystal forms in a deterministic location because fluctuations in the initial conditions [141] (due to density perturbations) or a hard wall boundary [145] break the symmetry. Equilibrium phase transitions are different from the dynamical phases because in some dynamical phases (like flocking) the jammed structures are not static.

5.4 Finite-size effects

We studied the effects of box size on the active needle band state. We varied the box in the direction of inhomogeneity while keeping the other dimension fixed. We looked at two initial conditions: a homogeneous nematic (Figure 5.5) and band state (Figure 5.6). For both, the concentration was $c^* = 1.7$, and driving was $\text{Pe} = 20$. The band state initial condition was

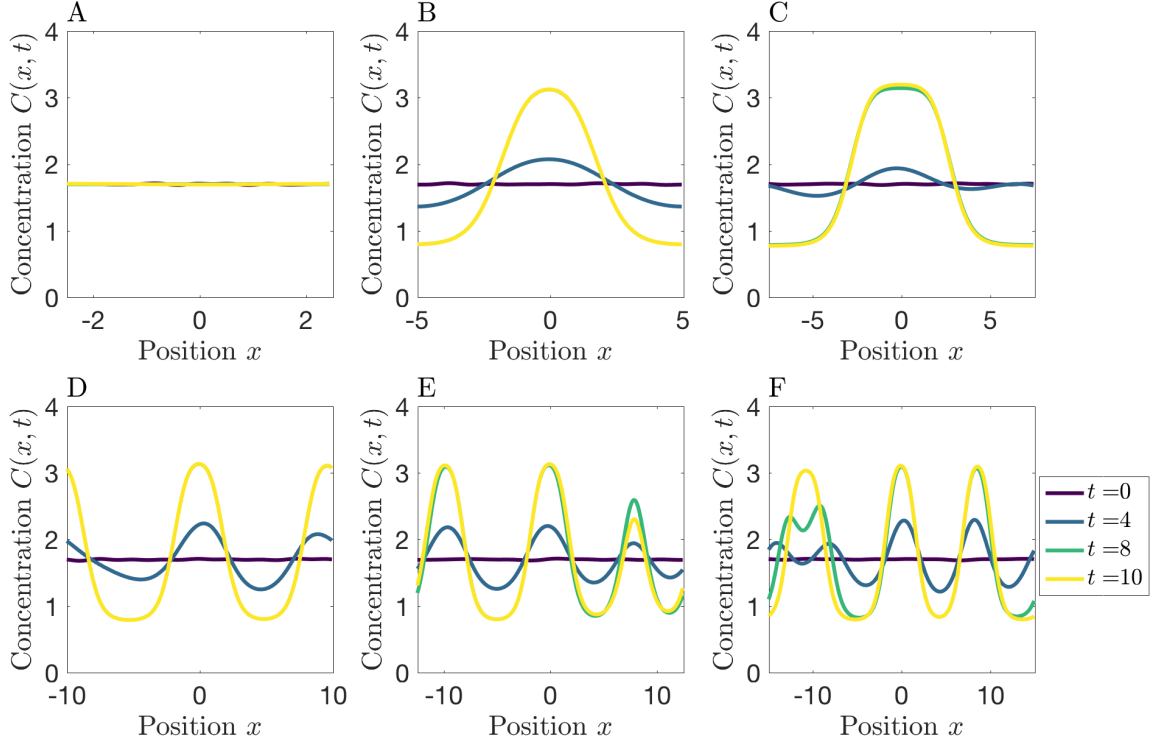


Figure 5.5: The effects of box size on the band state with $c^* = 1.70$ and $\text{Pe} = 20$. The concentration along the inhomogeneous direction is plotted as function of position at various times (indicated by color) for: (A) $L_{\text{box}} = 5$, (B) $L_{\text{box}} = 10$, (C) $L_{\text{box}} = 15$, (D) $L_{\text{box}} = 20$, (E) $L_{\text{box}} = 25$, (F) $L_{\text{box}} = 30$. The initial condition was a homogeneous nematic with random perturbations. The concentration was shifted in the plots so that the highest peak is at $x = 0$.

the steady state solution for a box size $L_{\text{box}} = 10$ ($c^* = 1.7$, $\text{Pe} = 20$). Note, the maximum concentration was centered at $x = 0$ for all plots. For both initial conditions, box size played a role. For the nematic initial condition (Figure 5.5), the band state did not form at the smallest box size $L_{\text{box}} = 5$ during the run; however, a single band formed at later times (results not shown). For $L_{\text{box}} = 10$ and $L_{\text{box}} = 15$, a single band formed and was stable. Multiple bands formed for larger boxes. Some bands were transient over the course of the simulation, *e.g.*, two separate peaks in $L_{\text{box}} = 30$ at $t = 4$ combined by $t = 10$. Note, these runs had not reached steady-state. These results show that multiple transient bands can form at larger box sizes. At a later time ($t = 20$) for $L_{\text{box}} = 20$ and $L_{\text{box}} = 25$, two bands were stable (results not shown), which suggests that multiple bands are stable in larger boxes.

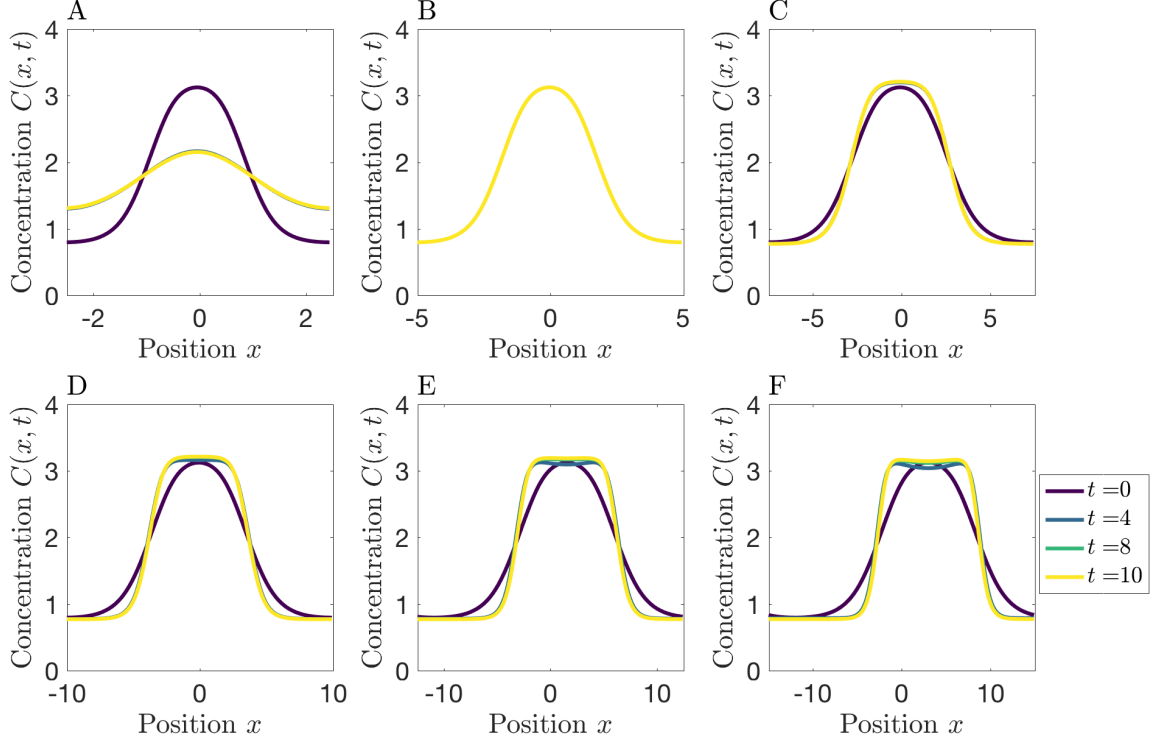


Figure 5.6: The effects of box size on the band state with $c^* = 1.70$ and $\text{Pe} = 20$. The concentration along the inhomogeneous direction is plotted as function of position at various times (indicated by color) for: (A) $L_{\text{box}} = 5$, (B) $L_{\text{box}} = 10$, (C) $L_{\text{box}} = 15$, (D) $L_{\text{box}} = 20$, (E) $L_{\text{box}} = 25$, (F) $L_{\text{box}} = 30$. The initial condition was the steady state solution for a box size $L_{\text{box}} = 10$. The concentration was shifted in the plots so that the highest peak is at $x = 0$.

In Figure 5.6, we studied the stability of a single band. The band shape changed with the box length. At larger box lengths, the band became more step-like. There was no evidence that the single band was unstable. The results in Figure 5.5 and Figure 5.6 suggest that the initial condition effects the number of bands. This differs from the homogeneous nematic to band transition, which is independent of initial condition.

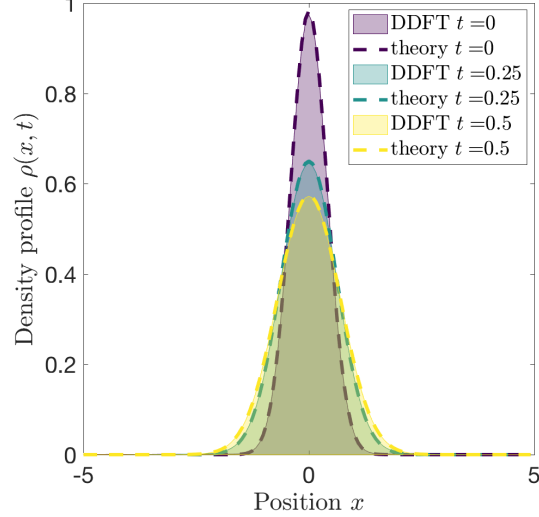


Figure 5.7: A comparison of the DDFT and analytic solution for noninteracting Brownian particles in a harmonic well. Time is indicated by color. The filled curve is the DDFT solution, and the dashed line is the analytic solution. The DDFT and analytic solution match at all times.

5.5 External potentials in DDFT

Up till now, we have not studied the effects of external potentials. Since the free energy is separable, the effects of an external potential is additive in DDFT [24]

$$\frac{\partial \rho(\mathbf{r}, \hat{\mathbf{u}}, t)}{\partial t} = \nabla \cdot \zeta^{-1} \left[k_B T \nabla \rho(\mathbf{r}, \hat{\mathbf{u}}, t) + \rho(\mathbf{r}, \hat{\mathbf{u}}, t) \nabla \frac{\delta \mathcal{F}^{\text{ex}}[\rho]}{\delta \rho(\mathbf{r}, \hat{\mathbf{u}}, t)} + \rho(\mathbf{r}, \hat{\mathbf{u}}, t) \nabla V_{\text{ext}}(\mathbf{r}, \hat{\mathbf{u}}, t) \right], \quad (5.7)$$

where V_{ext} is the external potential. To validate the numerics, we compared the numerical solution for noninteracting particles in a harmonic well $V_{\text{ext}} = \frac{1}{2}kx^2$ to the analytic solution [27]. The equation of motion for the one-dimension case is

$$\frac{\partial \rho(x, t)}{\partial t} = D \frac{\partial^2 \rho(x, t)}{\partial x^2} + Dk\beta \frac{\partial}{\partial x} [x\rho(x, t)], \quad (5.8)$$

where k is the spring constant and $\beta = 1/k_B T$. The analytic solution is

$$\rho(x, t) = \frac{1}{\sqrt{2\pi\alpha(t)}} e^{-\frac{x^2}{2\alpha(t)}}, \quad (5.9)$$

where $\alpha(t) = \frac{1}{\beta k}(1 - e^{-2kD\beta t})$. In Eqn. 5.9, the initial condition is a delta function centered at $x = 0$. To compare the DDFT to the analytic solution, we used the initial condition

$$\rho(x, t = 0) = \frac{1}{\sqrt{2\pi\alpha(0.1)}} e^{-\frac{x^2}{2\alpha(0.1)}}. \quad (5.10)$$

Using a Gaussian as an initial condition avoids numerical issues with sharply peaked delta functions. The comparison between the analytic and DDFT solution with $D = 1$ and $k = 2$ is shown in Figure 5.7. The shaded curve is the DDFT solution, the dashed line is the analytic solution, and the color indicates the time. For the DDFT solution, we solved the system in 2D with the potential along x and took a slice along $P(x, y = 0, t)$ (there was no variation along y). Note, the analytic solution is for infinite boundaries while DDFT has periodic boundaries. I selected a box size where boundary effects did not influence the solution. We see excellent agreement between the numerics and analytic solution. This test validates external potentials in the code. While this case was a one-dimensional example, the code can handle potentials for up to three dimensions.

Chapter 6

Conclusions and future directions

6.1 Conclusions

In this thesis, I have presented my advances to the understanding of particle dynamics in crowded media and active matter. For crowded media, I have shown how soft obstacles affect tracer diffusion. An obstacle's influence on tracer dynamics is highly dependent on the stickiness of the obstacle, *i.e.*, the bound mobility. Bound mobility can minimize the effects of inhibited motion and anomalous subdiffusion. The role of binding and bound motion was also studied for transport of across biofilters. I presented a minimal model in terms of measurable parameters and studied the selectivity of the nuclear pore complex. Finally, I studied dynamical phases of an active matter system. I presented a macroscopic model, built from a microscopic picture, using dynamical density functional theory. I applied this theory to study the banding instability of self-propelled needles. I contributed to and independently wrote several software packages my various projects, summarized in Appendix F.

For all of these systems, I developed models starting from microscopic Brownian dynamics. Studying particle dynamics naturally lends itself to two of the main tools discussed in this thesis: lattice Monte Carlo and Brownian dynamics simulations. I discussed how these tools were advanced and applied to both crowded and active systems. I also connected microscopic models to macroscopic equations, *i.e.*, nonlinear diffusion equations, through DDFT. In doing this, I've

hoped to illustrate a general approach to solving biophysics problems. We start with a question or system of interest and try to use our hammer, Brownian dynamics simulations (off or on lattice). The Langevin equations of motion, either with full interactions or making approximations, are analyzed and refined until we have a minimal model that describes some phenomena. Deriving a theory for the continuum equations is a harder task, but in doing so, larger systems and ensemble averaged behavior can be studied. DDFT is one tool for obtaining these equations that has a direct connection to the microscopic picture.

My final comment is a reflection on my graduate experience. All of my projects have been substantially computational: involving collaborating on ideas, distributing and receiving code, and working in shared repositories on projects. From my experience, I really have come to value writing modular code that is user-friendly and generalizable for other projects. For example, my repository *ActiveDDFT* can easily handle any external field or interaction (in the mean-field or second virial approximation) with just a few lines of additional code. By implementing a mix of object-oriented and procedural code, I hope that future students could easily use, adapt, and advance my software packages. Gaining this perspective was a valuable lesson learned in graduate school. I found that developing computational and problem solving skills, improving communication, and gaining the confidence to tackle hard problems were the most indispensable tools I gained in graduate school.

6.2 Future directions

When thinking about future directions, I have some short term goals for my research group and broader goals of the field. For my group, I wrote all of my code with the intent that it can be applied to other related problems. I believe there is further work that can easily be built onto my existing software packages.

For the crowded media projects, including inter-particle interactions is what I would look at next. For the lattice model, excluded interactions is not tough to do. For a continuum model, a scaled particle theory [152] for steric interactions would be the first thing to try. Long range interactions and external potentials could also be implemented with DDFT to study the effects of

charge. These improvements are aligned with a broader goal for the field: directly modeling the temporal evolution of experimentally measured density profiles in hydrogels. No one knows for sure how filters like the NPC work. I believe that accurately modeling the temporal behavior of experimental results, *e.g.*, TFs diffusing across a hydrogel, will be the key to understanding these systems better.

My *ActiveDDFT* repository, used in the active needle project, is well equipped to handle other excess functionals. I believe studying active systems with softer potentials, like a Gaussian core [143,144] or soft shoulder [145,153] (where DDFT has shown success), would be a natural next step. For broader directions, relatively little work is being done to improve models starting from microscopic interactions. While models similar to our active needle project claimed to see evidence of flocking [47], we did not. I think more work to improve the microscopic functionals is necessary to describe the physics seen in simulations. In a symmetry based model (which many groups use), it is not clear how microscopic interactions can lead to macroscopic collective behavior. Also, using a theory based on equilibrium systems may be suspect for active systems far from equilibrium. One promising approach for nonequilibrium systems is power functional theory [154] which builds dissipation into the model.

A final direction that is appealing is to unify my work on crowded and active systems. One could imagine that obstacles could facilitate the self-assembly process, and in reality, active biological systems can be crowded [2]. The easiest way forward would be to include obstacles in interacting active Brownian simulations. I believe DDFT with external fields mimicking obstacles is feasible.

After my Ph.D., I am off to industry to start a career in data science. Machine learning and statistical modeling are quickly advancing fields, and we are living in an exciting time where technology is rapidly changing the world at an unprecedented rate. I look forward to learning, growing, and continuing to solve problems in a new field. If I help the machines take over, I am sorry. But, hey, at least we had a good run.

Bibliography

- [1] J. Witten and K. Ribbeck. The particle in the spider's web: Transport through biological hydrogels. *Nanoscale*, 9(24):8080–8095, June 2017.
- [2] F. Höfling and T. Franosch. Anomalous transport in the crowded world of biological cells. *Rep. Prog. Phys.*, 76(4):046602, 2013.
- [3] G. J. Schütz, H. Schindler, and T. Schmidt. Single-molecule microscopy on model membranes reveals anomalous diffusion. *Biophys. J.*, 73(2):1073–1080, August 1997.
- [4] G. J. Schütz, G. Kada, V. P. Pastushenko, and H. Schindler. Properties of lipid microdomains in a muscle cell membrane visualized by single molecule microscopy. *EMBO J.*, 19(5):892–901, March 2000.
- [5] D. V. Nicolau, J. F. Hancock, and K. Burrage. Sources of Anomalous Diffusion on Cell Membranes: A Monte Carlo Study. *Biophys. J.*, 92(6):1975–1987, March 2007.
- [6] A. V. Weigel, B. Simon, M. M. Tamkun, and D. Krapf. Ergodic and nonergodic processes coexist in the plasma membrane as observed by single-molecule tracking. *Proc. Natl. Acad. Sci. U.S.A.*, 108(16):6438–6443, April 2011.
- [7] M. Javanainen, H. Hammaren, L. Monticelli, J.-H. Jeon, M. S. Miettinen, H. Martinez-Seara, R. Metzler, and I. Vattulainen. Anomalous and normal diffusion of proteins and lipids in crowded lipid membranes. *Faraday Discuss.*, 161(0):397–417, 2013.
- [8] D. Krapf. Mechanisms Underlying Anomalous Diffusion in the Plasma Membrane. *Curr. Top. Membr.*, 75:167–207, January 2015.
- [9] J.-H. Jeon, M. Javanainen, H. Martinez-Seara, R. Metzler, and I. Vattulainen. Protein Crowding in Lipid Bilayers Gives Rise to Non-Gaussian Anomalous Lateral Diffusion of Phospholipids and Proteins. *Phys. Rev. X*, 6(2), April 2016.
- [10] S. Sadegh, J. L. Higgins, P. C. Mannion, M. M. Tamkun, and D. Krapf. Plasma Membrane is Compartmentalized by a Self-Similar Cortical Actin Meshwork. *Phys. Rev. X*, 7(1):011031, March 2017.
- [11] S. Stylianidou, N. J. Kuwada, and P. A. Wiggins. Cytoplasmic Dynamics Reveals Two Modes of Nucleoid-Dependent Mobility. *Biophys. J.*, 107(11):2684–2692, December 2014.
- [12] H.-P. Zhang, A. Be'er, E.-L. Florin, and H. L. Swinney. Collective motion and density fluctuations in bacterial colonies. *Proc. Natl. Acad. Sci. U.S.A.*, 107(31):13626–13630, 2010.

- [13] L. H. Cisneros, J. O. Kessler, S. Ganguly, and R. E. Goldstein. Dynamics of swimming bacteria: Transition to directional order at high concentration. *Phys. Rev. E*, 83(6):061907, June 2011.
- [14] S. Thutupalli, M. Sun, F. Bunyak, K. Palaniappan, and J. W. Shaevitz. Directional reversals enable *Myxococcus xanthus* cells to produce collective one-dimensional streams during fruiting-body formation. *J. Royal Soc. Interface*, 12(109):20150049, August 2015.
- [15] M. C. Marchetti, J. F. Joanny, S. Ramaswamy, T. B. Liverpool, J. Prost, M. Rao, and R. A. Simha. Hydrodynamics of soft active matter. *Rev. Mod. Phys.*, 85(3):1143–1189, July 2013.
- [16] R. Zwanzig. *Nonequilibrium Statistical Mechanics*. Oxford University Press, Oxford ; New York, 2001.
- [17] A. Einstein. Über die von der molekularkinetischen Theorie der Wärme geforderte Bewegung von in ruhenden Flüssigkeiten suspendierten Teilchen. *Ann. Phys.*, 322(8):549–560, January 1905.
- [18] N. W. Ashcroft and N. D. Mermin. *Solid State Physics*. Brooks Cole, New York, 1 edition edition, January 1976.
- [19] P. D. Lett, W. D. Phillips, S. L. Rolston, C. E. Tanner, R. N. Watts, and C. I. Westbrook. Optical molasses. *JOSA B*, 6(11):2084–2107, November 1989.
- [20] H. C. Berg. *Random Walks in Biology*. Princeton University Press, Princeton, N.J, revised edition edition, September 1993.
- [21] M. W. Stefferson, S. L. Norris, F. J. Vernerey, M. D. Betterton, and L. E. Hough. Effects of soft interactions and bound mobility on diffusion in crowded environments: A model of sticky and slippery obstacles. *Phys. Biol.*, 14(4):045008, June 2017.
- [22] U. M. B. Marconi and P. Tarazona. Dynamic density functional theory of fluids. *J. Chem. Phys.*, 110(16):8032–8044, April 1999.
- [23] U. M. B. Marconi and P. Tarazona. Dynamic density functional theory of fluids. *J. Phys. Condens. Matter*, 12(8A):A413, 2000.
- [24] A. J. Archer and R. Evans. Dynamical density functional theory and its application to spinodal decomposition. *J. Chem. Phys.*, 121(9):4246–4254, September 2004.
- [25] A. J. Archer. Dynamical density functional theory: Binary phase-separating colloidal fluid in a cavity. *J. Phys. Condens. Matter*, 17(10):1405–1427, March 2005.
- [26] J. K. G. Dhont. *An Introduction to Dynamics of Colloids*. Number vol. 2 in Studies in interface science. Elsevier, Amsterdam, Netherlands ; New York, 1996.
- [27] M. Doi and S. F. Edwards. *The Theory of Polymer Dynamics*. Clarendon Press, 1988.
- [28] P. S. Grassia, E. J. Hinch, and L. C. Nitsche. Computer simulations of Brownian motion of complex systems. *J. Fluid Mech.*, 282:373–403, January 1995.
- [29] R. Metzler and J. Klafter. The random walk's guide to anomalous diffusion: A fractional dynamics approach. *Phys. Rep.*, 339(1):1–77, December 2000.

- [30] I. M. Sokolov, J. Klafter, and A. Blumen. Fractional Kinetics. *Phys. Today*, 55(11):48–54, November 2002.
- [31] M. J. Saxton. Anomalous diffusion due to obstacles: A Monte Carlo study. *Biophys. J.*, 66(2):394–401, February 1994.
- [32] T. J. Feder, I. Brust-Mascher, J. P. Slattery, B. Baird, and W. W. Webb. Constrained diffusion or immobile fraction on cell surfaces: A new interpretation. *Biophys. J.*, 70(6):2767–2773, June 1996.
- [33] M. Weiss, M. Elsner, F. Kartberg, and T. Nilsson. Anomalous Subdiffusion Is a Measure for Cytoplasmic Crowding in Living Cells. *Biophys. J.*, 87(5):3518–3524, November 2004.
- [34] R. N. Ghosh and W. W. Webb. Automated detection and tracking of individual and clustered cell surface low density lipoprotein receptor molecules. *Biophys. J.*, 66(5):1301–1318, May 1994.
- [35] M. J. Saxton. Lateral diffusion in an archipelago. The effect of mobile obstacles. *Biophys. J.*, 52(6):989–997, December 1987.
- [36] A. J. Ellery, M. J. Simpson, S. W. McCue, and R. E. Baker. Characterizing transport through a crowded environment with different obstacle sizes. *J. Chem. Phys.*, 140(5):054108, February 2014.
- [37] A. J. Ellery, R. E. Baker, S. W. McCue, and M. J. Simpson. Modeling transport through an environment crowded by a mixture of obstacles of different shapes and sizes. *Physica A*, 449:74–84, May 2016.
- [38] M. J. Saxton. Anomalous diffusion due to binding: A Monte Carlo study. *Biophys. J.*, 70(3):1250–1262, March 1996.
- [39] A. J. Ellery, R. E. Baker, and M. J. Simpson. An analytical method for disentangling the roles of adhesion and crowding for random walk models on a crowded lattice. *Phys. Biol.*, 13(5):05LT02, 2016.
- [40] C. P. Brangwynne, C. R. Eckmann, D. S. Courson, A. Rybarska, C. Hoege, J. Gharakhani, F. Jülicher, and A. A. Hyman. Germline P Granules Are Liquid Droplets That Localize by Controlled Dissolution/Condensation. *Science*, 324(5935):1729–1732, June 2009.
- [41] A. Molliex, J. Temirov, J. Lee, M. Coughlin, A. P. Kanagaraj, H. J. Kim, T. Mittag, and J. P. Taylor. Phase Separation by Low Complexity Domains Promotes Stress Granule Assembly and Drives Pathological Fibrillization. *Cell*, 163(1):123–133, September 2015.
- [42] L. E. Hough, K. Dutta, S. Sparks, D. B. Temel, A. Kamal, J. Tetenbaum-Novatt, M. P. Rout, and D. Cowburn. The molecular mechanism of nuclear transport revealed by atomic-scale measurements. *eLife*, 4:e10027, September 2015.
- [43] B. Raveh, J. M. Karp, S. Sparks, K. Dutta, M. P. Rout, A. Sali, and D. Cowburn. Slide-and-exchange mechanism for rapid and selective transport through the nuclear pore complex. *Proc. Natl. Acad. Sci. U.S.A.*, 113(18):E2489–E2497, March 2016.

- [44] B. L. Timney, B. Raveh, R. Mironksa, J. M. Trivedi, S. J. Kim, D. Russel, S. R. Wente, A. Sali, and M. P. Rout. Simple rules for passive diffusion through the nuclear pore complex. *J. Cell Biol.*, 215(1):57–76, September 2016.
- [45] L. Maguire, M. W. Stefferson, M. D. Betterton, and L. E. Hough. Design principles of binding-induced selective transport through the nuclear pore complex. *(To be published)*, 2018.
- [46] J. P. Hansen and I. R. McDonald. *Theory of Simple Liquids*. Elsevier Academic Press, London ; Burlington, MA, 3rd ed edition, 2006.
- [47] A. Baskaran and M. C. Marchetti. Hydrodynamics of self-propelled hard rods. *Phys. Rev. E*, 77(1), January 2008.
- [48] A. Baskaran and M. C. Marchetti. Enhanced Diffusion and Ordering of Self-Propelled Rods. *Phys. Rev. Lett.*, 101(26), December 2008.
- [49] H. H. Wensink and H. Löwen. Aggregation of self-propelled colloidal rods near confining walls. *Phys. Rev. E*, 78(3), September 2008.
- [50] A. Baskaran and M. C. Marchetti. Self-regulation in self-propelled nematic fluids. *Euro. Phys. J. E*, 35(9), September 2012.
- [51] F. Ginelli, F. Peruani, M. Bär, and H. Chaté. Large-Scale Collective Properties of Self-Propelled Rods. *Phys. Rev. Lett.*, 104(18):184502, May 2010.
- [52] H.-S. Kuan, R. Blackwell, L. E. Hough, M. A. Glaser, and M. D. Betterton. Hysteresis, reentrance, and glassy dynamics in systems of self-propelled rods. *Phys. Rev. E*, 92(6), December 2015.
- [53] M. Stefferson, H.-S. Kuan, M. A. Glaser, and M. D. Betterton. Self-organized band state of self-propelled hard needles in two dimensions. *(To be published)*, 2018.
- [54] J. H. Petropoulos. Membrane transport properties in relation to microscopic and macroscopic structural inhomogeneity. *J. Membr. Sci.*, 52(3):305–323, September 1990.
- [55] S. L. Veatch and S. L. Keller. Organization in Lipid Membranes Containing Cholesterol. *Phys. Rev. Lett.*, 89(26):268101, December 2002.
- [56] P. B. Crowley, E. Chow, and T. Papkovskaia. Protein Interactions in the Escherichia coli Cytosol: An Impediment to In-Cell NMR Spectroscopy. *Chembiochem*, 12(7):1043–1048, 2011.
- [57] M. A. Mourão, J. B. Hakim, and S. Schnell. Connecting the Dots: The Effects of Macromolecular Crowding on Cell Physiology. *Biophys. J.*, 107(12):2761–2766, December 2014.
- [58] V. P. Zhdanov and F. Höök. Kinetics of enzymatic reactions in lipid membranes containing domains. *Phys. Biol.*, 12(2):026003, April 2015.
- [59] T. Fujiwara, K. Ritchie, H. Murakoshi, K. Jacobson, and A. Kusumi. Phospholipids undergo hop diffusion in compartmentalized cell membrane. *J. Cell Biol.*, 157(6):1071–1082, June 2002.

- [60] M. B. Forstner, D. S. Martin, F. Rückerl, J. A. Käs, and C. Selle. Attractive membrane domains control lateral diffusion. *Phys. Rev. E*, 77(5):051906, May 2008.
- [61] J. Ehrig, E. P. Petrov, and P. Schwille. Near-Critical Fluctuations and Cytoskeleton-Assisted Phase Separation Lead to Subdiffusion in Cell Membranes. *Biophys. J.*, 100(1):80–89, January 2011.
- [62] J. R. Silvius. Partitioning of membrane molecules between raft and non-raft domains: Insights from model-membrane studies. *Biochim. Biophys. Acta BBA - Mol. Cell Res.*, 1746(3):193–202, December 2005.
- [63] A. Iyer, N. Schilderink, M. M. A. E. Claessens, and V. Subramaniam. Membrane-Bound Alpha Synuclein Clusters Induce Impaired Lipid Diffusion and Increased Lipid Packing. *Biophys. J.*, 111(11):2440–2449, December 2016.
- [64] A. Wedemeier, H. Merlitz, C.-X. Wu, and J. Langowski. How proteins squeeze through polymer networks: A Cartesian lattice study. *J. Chem. Phys.*, 131(6):064905, August 2009.
- [65] H. Berry. Monte carlo simulations of enzyme reactions in two dimensions: Fractal kinetics and spatial segregation. *Biophys. J.*, 83(4):1891–1901, October 2002.
- [66] D. S. Banks and C. Fradin. Anomalous Diffusion of Proteins Due to Molecular Crowding. *Biophys. J.*, 89(5):2960–2971, November 2005.
- [67] A. J. Ellery, R. E. Baker, and M. J. Simpson. Calculating the Fickian diffusivity for a lattice-based random walk with agents and obstacles of different shapes and sizes. *Phys. Biol.*, 12(6):066010, 2015.
- [68] P. Nandigrami, B. Grove, A. Konya, and R. L. B. Selinger. Gradient-driven diffusion and pattern formation in crowded mixtures. *Phys. Rev. E*, 95(2):022107, February 2017.
- [69] J.-F. Mercier and G. W. Slater. Numerically exact diffusion coefficients for lattice systems with periodic boundary conditions. II. Numerical approach and applications. *J. Chem. Phys.*, 110(12):6057–6065, March 1999.
- [70] J.-F. Mercier, G. W. Slater, and H. L. Guo. Numerically exact diffusion coefficients for lattice systems with periodic boundary conditions. I. Theory. *J. Chem. Phys.*, 110(12):6050–6056, March 1999.
- [71] A. J. Ellery, R. E. Baker, and M. J. Simpson. Communication: Distinguishing between short-time non-Fickian diffusion and long-time Fickian diffusion for a random walk on a crowded lattice. *J. Chem. Phys.*, 144(17):171104, May 2016.
- [72] A. Wedemeier, H. Merlitz, C.-X. Wu, and J. Langowski. Modeling diffusional transport in the interphase cell nucleus. *J. Chem. Phys.*, 127(4):045102, July 2007.
- [73] A. Wedemeier, H. Merlitz, and J. Langowski. Anomalous diffusion in the presence of mobile obstacles. *EPL*, 88(3):38004, November 2009.
- [74] A. Wedemeier, T. Zhang, H. Merlitz, C.-X. Wu, and J. Langowski. The role of chromatin conformations in diffusional transport of chromatin-binding proteins: Cartesian lattice simulations. *J. Chem. Phys.*, 128(15):155101, April 2008.

- [75] N. Metropolis, A. W. Rosenbluth, M. N. Rosenbluth, A. H. Teller, and E. Teller. Equation of State Calculations by Fast Computing Machines. *J. Chem. Phys.*, 21(6):1087–1092, June 1953.
- [76] M. Magdziarz, A. Weron, K. Burnecki, and J. Klafter. Fractional Brownian Motion Versus the Continuous-Time Random Walk: A Simple Test for Subdiffusive Dynamics. *Phys. Rev. Lett.*, 103(18):180602, October 2009.
- [77] J. H. P. Schulz, E. Barkai, and R. Metzler. Aging Renewal Theory and Application to Random Walks. *Phys. Rev. X*, 4(1):011028, February 2014.
- [78] M. J. Saxton. Single-particle tracking: The distribution of diffusion coefficients. *Biophys. J.*, 72(4):1744–1753, April 1997.
- [79] D. Stauffer and A. Aharony. *Introduction To Percolation Theory*. Taylor & Francis, July 1994.
- [80] C. Strambio-De-Castillia, M. Niepel, and M. P. Rout. The nuclear pore complex: Bridging nuclear transport and gene regulation. *Nat. Rev. Mol. Cell Biol.*, 11(7):490–501, July 2010.
- [81] A. F. L. Schneider and C. P. H. Hackenberger. Fluorescent labelling in living cells. *Curr. Opin. Biotechnol.*, 48:61–68, December 2017.
- [82] X. Huang, J. Chisholm, J. Zhuang, Y. Xiao, G. Duncan, X. Chen, J. S. Suk, and J. Hanes. Protein nanocages that penetrate airway mucus and tumor tissue. *Proc. Natl. Acad. Sci. U.S.A.*, 114(32):E6595–E6602, August 2017.
- [83] P. Mastorakos, A. L. da Silva, J. Chisholm, E. Song, W. K. Choi, M. P. Boyle, M. M. Morales, J. Hanes, and J. S. Suk. Highly compacted biodegradable DNA nanoparticles capable of overcoming the mucus barrier for inhaled lung gene therapy. *Proc. Natl. Acad. Sci. U.S.A.*, 112(28):8720–8725, July 2015.
- [84] D. Frenkiel-Krispin, B. Maco, U. Aebi, and O. Medalia. Structural Analysis of a Metazoan Nuclear Pore Complex Reveals a Fused Concentric Ring Architecture. *J. Mol. Biol.*, 395(3):578–586, January 2010.
- [85] T. Maimon, N. Elad, I. Dahan, and O. Medalia. The Human Nuclear Pore Complex as Revealed by Cryo-Electron Tomography. *Structure*, 20(6):998–1006, June 2012.
- [86] K. Ribbeck and D. Görlich. Kinetic analysis of translocation through nuclear pore complexes. *EMBO J.*, 20(6):1320–1330, 2001.
- [87] S. Milles, D. Mercadante, I. V. Aramburu, M. R. Jensen, N. Banterle, C. Koehler, S. Tyagi, J. Clarke, S. L. Shammas, M. Blackledge, F. Gräter, and E. A. Lemke. Plasticity of an Ultrafast Interaction between Nucleoporins and Nuclear Transport Receptors. *Cell*, 163(3):734–745, October 2015.
- [88] B. Pyhtila and M. Rexach. A gradient of affinity for the karyopherin Kap95p along the yeast nuclear pore complex. *J. Biol. Chem.*, 278(43):42699–42709, 2003.
- [89] D. Gilchrist, B. Mykytka, and M. Rexach. Accelerating the Rate of Disassembly of Karyopherin·Cargo Complexes. *J. Biol. Chem.*, 277(20):18161–18172, May 2002.

- [90] J. Tetenbaum-Novatt, L. E. Hough, R. Mironksa, A. S. McKenney, and M. P. Rout. Nucleocytoplasmic transport: A role for non-specific competition in karyopherin-nucleoporin interactions. *Mol. Cell. Proteomics*, 2012.
- [91] A. Vovk, C. Gu, M. G. Opferman, L. E. Kapinos, R. Y. H. Lim, R. D. Coalson, D. Jasnow, and A. Zilman. Simple biophysics underpins collective conformations of the intrinsically disordered proteins of the Nuclear Pore Complex. *eLife*, 5:e10785, May 2016.
- [92] J. P. Siebrasse and R. Peters. Rapid translocation of NTF2 through the nuclear pore of isolated nuclei and nuclear envelopes. *EMBO Rep.*, 3(9):887–892, September 2002.
- [93] N. I. Kiskin, J. P. Siebrasse, and R. Peters. Optical Microwell Assay of Membrane Transport Kinetics. *Biophys. J.*, 85(4):2311–2322, October 2003.
- [94] F. J. Nédélec, T. Surrey, A. C. Maggs, and S. Leibler. Self-organization of microtubules and motors. *Nature*, 389(6648):305–308, September 1997.
- [95] A. Cavagna, A. Cimarelli, I. Giardina, G. Parisi, R. Santagati, F. Stefanini, and M. Viale. Scale-free correlations in starling flocks. *Proc. Natl. Acad. Sci. U.S.A.*, 107(26):11865–11870, June 2010.
- [96] W.-J. Rappel, A. Nicol, A. Sarkissian, H. Levine, and W. F. Loomis. Self-organized Vortex State in Two-Dimensional Dictyostelium Dynamics. *Phys. Rev. Lett.*, 83(6):1247–1250, August 1999.
- [97] A. Kudrolli, G. Lumay, D. Volfson, and L. S. Tsimring. Swarming and Swirling in Self-Propelled Polar Granular Rods. *Phys. Rev. Lett.*, 100(5):058001, February 2008.
- [98] V. Narayan, S. Ramaswamy, and N. Menon. Long-Lived Giant Number Fluctuations in a Swarming Granular Nematic. *Science*, 317(5834):105–108, July 2007.
- [99] J. Deseigne, O. Dauchot, and H. Chaté. Collective Motion of Vibrated Polar Disks. *Phys. Rev. Lett.*, 105(9):098001, August 2010.
- [100] T. Vicsek, A. Czirók, E. Ben-Jacob, I. Cohen, and O. Shochet. Novel Type of Phase Transition in a System of Self-Driven Particles. *Phys. Rev. Lett.*, 75(6):1226–1229, August 1995.
- [101] J. Toner and Y. Tu. Long-Range Order in a Two-Dimensional Dynamical XY Model: How Birds Fly Together. *Phys. Rev. Lett.*, 75(23):4326–4329, December 1995.
- [102] J. Toner and Y. Tu. Flocks, herds, and schools: A quantitative theory of flocking. *Phys. Rev. E*, 58(4):4828–4858, October 1998.
- [103] F. Peruani and M. Bär. A kinetic model and scaling properties of non-equilibrium clustering of self-propelled particles. *New J. Phys.*, 15(6):065009, 2013.
- [104] F. Peruani, A. Deutsch, and M. Bär. Nonequilibrium clustering of self-propelled rods. *Phys. Rev. E*, 74(3):030904, September 2006.
- [105] H. H. Wensink and H. Löwen. Emergent states in dense systems of active rods: From swarming to turbulence. *J. Phys. Condens. Matter*, 24(46):464130, 2012.

- [106] S. R. McCandlish, A. Baskaran, and M. F. Hagan. Spontaneous segregation of self-propelled particles with different motilities. *Soft Matter*, 8(8):2527–2534, February 2012.
- [107] G. Grégoire and H. Chaté. Onset of Collective and Cohesive Motion. *Phys. Rev. Lett.*, 92(2):025702, January 2004.
- [108] H. Chaté, F. Ginelli, G. Grégoire, and F. Raynaud. Collective motion of self-propelled particles interacting without cohesion. *Phys. Rev. E*, 77(4):046113, April 2008.
- [109] T. Gao, R. Blackwell, M. A. Glaser, M. D. Betterton, and M. J. Shelley. Multiscale Polar Theory of Microtubule and Motor-Protein Assemblies. *Phys. Rev. Lett.*, 114(4):048101, January 2015.
- [110] S. Mishra, A. Baskaran, and M. C. Marchetti. Fluctuations and pattern formation in self-propelled particles. *Phys. Rev. E*, 81(6), June 2010.
- [111] A. Gopinath, M. F. Hagan, M. C. Marchetti, and A. Baskaran. Dynamical self-regulation in self-propelled particle flows. *Phys. Rev. E*, 85(6), June 2012.
- [112] A. Peshkov, I. S. Aranson, E. Bertin, H. Chaté, and F. Ginelli. Nonlinear Field Equations for Aligning Self-Propelled Rods. *Phys. Rev. Lett.*, 109(26):268701, December 2012.
- [113] R. A. Simha and S. Ramaswamy. Hydrodynamic Fluctuations and Instabilities in Ordered Suspensions of Self-Propelled Particles. *Phys. Rev. Lett.*, 89(5), July 2002.
- [114] S. Ramaswamy, R. A. Simha, and J. Toner. Active nematics on a substrate: Giant number fluctuations and long-time tails. *EPL*, 62(2):196, April 2003.
- [115] H. Chaté, F. Ginelli, and R. Montagne. Simple Model for Active Nematics: Quasi-Long-Range Order and Giant Fluctuations. *Phys. Rev. Lett.*, 96(18):180602, May 2006.
- [116] A. M. Menzel. Unidirectional laning and migrating cluster crystals in confined self-propelled particle systems. *J. Phys. Condens. Matter*, 25(50):505103, 2013.
- [117] K. R. Sütterlin, A. Wysocki, A. V. Ivlev, C. Räth, H. M. Thomas, M. Rubin-Zuzic, W. J. Goedheer, V. E. Fortov, A. M. Lipaev, V. I. Molotkov, O. F. Petrov, G. E. Morfill, and H. Löwen. Dynamics of Lane Formation in Driven Binary Complex Plasmas. *Phys. Rev. Lett.*, 102(8):085003, February 2009.
- [118] M. E. Leunissen, C. G. Christova, A.-P. Hynninen, C. P. Royall, A. I. Campbell, A. Imhof, M. Dijkstra, R. van Roij, and A. van Blaaderen. Ionic colloidal crystals of oppositely charged particles. *Nature*, 437(7056):235–240, September 2005.
- [119] T. Vissers, A. Wysocki, M. Rex, H. Löwen, C. P. Royall, A. Imhof, and A. van Blaaderen. Lane formation in driven mixtures of oppositely charged colloids. *Soft Matter*, 7(6):2352–2356, March 2011.
- [120] J. Palacci, S. Sacanna, A. P. Steinberg, D. J. Pine, and P. M. Chaikin. Living Crystals of Light-Activated Colloidal Surfers. *Science*, 339(6122):936–940, February 2013.
- [121] I. Theurkauff, C. Cottin-Bizonne, J. Palacci, C. Ybert, and L. Bocquet. Dynamic Clustering in Active Colloidal Suspensions with Chemical Signaling. *Phys. Rev. Lett.*, 108(26):268303, June 2012.

- [122] I. Buttinoni, J. Bialké, F. Kümmel, H. Löwen, C. Bechinger, and T. Speck. Dynamical Clustering and Phase Separation in Suspensions of Self-Propelled Colloidal Particles. *Phys. Rev. Lett.*, 110(23):238301, June 2013.
- [123] E. Bertin, M. Droz, and G. Grégoire. Hydrodynamic equations for self-propelled particles: Microscopic derivation and stability analysis. *J. Phys. A*, 42(44):445001, 2009.
- [124] T. B. Liverpool and M. C. Marchetti. Instabilities of Isotropic Solutions of Active Polar Filaments. *Phys. Rev. Lett.*, 90(13):138102, April 2003.
- [125] R. Evans. The nature of the liquid-vapour interface and other topics in the statistical mechanics of non-uniform, classical fluids. *Adv. Phys.*, 28(2):143–200, April 1979.
- [126] A. Baskaran and M. C. Marchetti. Nonequilibrium statistical mechanics of self-propelled hard rods. *J. Stat. Mech. Theory Exp.*, 2010(04):P04019, 2010.
- [127] D. Frenkel and R. Eppenga. Evidence for algebraic orientational order in a two-dimensional hard-core nematic. *Phys. Rev. A*, 31(3):1776–1787, March 1985.
- [128] Y.-G. Tao, W. K. den Otter, J. T. Padding, J. K. G. Dhont, and W. J. Briels. Brownian dynamics simulations of the self- and collective rotational diffusion coefficients of rigid long thin rods. *J. Chem. Phys.*, 122(24):244903, June 2005.
- [129] T.-G. Tao, W. K. den Otter, J. K. G. Dhont, and W. J. Briels. Isotropic-nematic spinodals of rigid long thin rodlike colloids by event-driven Brownian dynamics simulations. *J. Chem. Phys.*, 124(13):134906, April 2006.
- [130] H. Löwen. Brownian dynamics of hard spherocylinders. *Phys. Rev. E*, 50(2):1232–1242, August 1994.
- [131] J. D. Weeks, D. Chandler, and H. C. Andersen. Role of Repulsive Forces in Determining the Equilibrium Structure of Simple Liquids. *J. Chem. Phys.*, 54(12):5237–5247, June 1971.
- [132] A. J. Archer and M. Rauscher. Dynamical density functional theory for interacting Brownian particles: Stochastic or deterministic? *J. Phys. A*, 37(40):9325–9333, October 2004.
- [133] L. Onsager. The effects of shape on the interaction of colloidal particles. *Ann. N. Y. Acad. Sci.*, 51(4):627–659, 1949.
- [134] R. F. Kayser and H. J. Raveché. Bifurcation in Onsager’s model of the isotropic-nematic transition. *Phys. Rev. A*, 17(6):2067, 1978.
- [135] M. A. Bates and D. Frenkel. Phase behavior of two-dimensional hard rod fluids. *J. Chem. Phys.*, 112(22):10034–10041, June 2000.
- [136] B. Fornberg. *A Practical Guide to Pseudospectral Methods*. Cambridge University Press, October 1998.
- [137] R. B. Sidje. Expokit: A software package for computing matrix exponentials. *ACM Trans. Math. Softw. TOMS*, 24(1):130–156, 1998.
- [138] E. Putzig and A. Baskaran. Phase separation and emergent structures in an active nematic fluid. *Phys. Rev. E*, 90(4):042304, October 2014.

- [139] J. Chakrabarti, J. Dzubiella, and H. Löwen. Dynamical instability in driven colloids. *EPL*, 61(3):415, 2003.
- [140] A. J. Archer and A. Malijevský. On the interplay between sedimentation and phase separation phenomena in two-dimensional colloidal fluids. *Mol. Phys.*, 109(7-10):1087–1099, March 2011.
- [141] A. Malijevský and A. J. Archer. Sedimentation of a two-dimensional colloidal mixture exhibiting liquid-liquid and gas-liquid phase separation: A dynamical density functional theory study. *J. Chem. Phys.*, 139(14):144901, October 2013.
- [142] D. Reguera and H. Reiss. The role of fluctuations in both density functional and field theory of nanosystems. *J. Chem. Phys.*, 120(6):2558–2564, February 2004.
- [143] A. Lang, C. N. Likos, M. Watzlawek, and H. Löwen. Fluid and solid phases of the Gaussian core model. *J. Phys. Condens. Matter*, 12(24):5087, 2000.
- [144] J. Dzubiella and C. N. Likos. Mean-field dynamical density functional theory. *J. Phys. Condens. Matter*, 15(6):L147, 2003.
- [145] A. J. Archer, A. M. Rucklidge, and E. Knobloch. Quasicrystalline Order and a Crystal-Liquid State in a Soft-Core Fluid. *Phys. Rev. Lett.*, 111(16), October 2013.
- [146] Y. Rosenfeld. Free-energy model for the inhomogeneous hard-sphere fluid in D dimensions: Structure factors for the hard-disk (D=2) mixtures in simple explicit form. *Phys. Rev. A*, 42(10):5978–5989, November 1990.
- [147] D. Frenkel and J. F. Maguire. Molecular dynamics study of infinitely thin hard rods: Scaling behavior of transport properties. *Phys. Rev. Lett.*, 47(15):1025, 1981.
- [148] D. Frenkel and J. F. Maguire. Molecular dynamics study of the dynamical properties of an assembly of infinitely thin hard rods. *Mol. Phys.*, 49(3):503–541, 1983.
- [149] D. S. Dean. Langevin equation for the density of a system of interacting Langevin processes. *J. Phys. A: Math. Gen.*, 29(24):L613, 1996.
- [150] M. A. Choudhary, D. Li, H. Emmerich, and H. Löwen. DDFT calibration and investigation of an anisotropic phase-field crystal model. *J. Phys.: Condens. Matter*, 23(26):265005, 2011.
- [151] G. Kahl and H. Löwen. Classical density functional theory: An ideal tool to study heterogeneous crystal nucleation. *J. Phys.: Condens. Matter*, 21(46):464101, 2009.
- [152] E. Helfand, H. L. Frisch, and J. L. Lebowitz. Theory of the Two- and One-Dimensional Rigid Sphere Fluids. *J. Chem. Phys.*, 34(3):1037–1042, March 1961.
- [153] A. J. Archer, A. M. Rucklidge, and E. Knobloch. Soft-core particles freezing to form a quasicrystal and a crystal-liquid phase. *Phys. Rev. E*, 92(1), July 2015.
- [154] M. Schmidt and J. M. Brader. Power functional theory for Brownian dynamics. *J. Chem. Phys.*, 138(21):214101, June 2013.

Appendix A

Fluctuation-dissipation theorem

Here, I derive the fluctuation-dissipation theorem, which connects the drag and random fluctuating forces on a particle in a heat bath [16]. The Langevin equation in one dimension is

$$\dot{v} = -\frac{1}{m} \left[\zeta v + -\frac{\partial U}{\partial x} + \xi(t) \right], \quad (\text{A.1})$$

where m is the mass of the particle, ζ the drag coefficient, U the potential energy, and ξ the random fluctuating force. For a non-interacting particle in the absence of external fields,

$$\dot{v} = -\frac{1}{m} [\zeta v + \xi(t)]. \quad (\text{A.2})$$

The random force is zero on average, there are no correlations between random kicks in time, and the random force has an unknown amplitude. Therefore,

$$\langle \xi(t) \rangle = 0, \quad (\text{A.3})$$

$$\langle \xi(t) \xi(t') \rangle = C \delta(t - t'), \quad (\text{A.4})$$

where C is the unknown coefficient and δ the Dirac delta function. The brackets $\langle \dots \rangle$ denote an ensemble average of the noise, *i.e.*, an average over all noise realizations. To solve Eqn. A.2, let $v(t) = e^{-\zeta t/m} y(t)$. This gives

$$\dot{y} = e^{\zeta t/m} \frac{\xi(t)}{m}, \quad (\text{A.5})$$

which can be integrated to

$$y(t) = y(0) + \int_0^t e^{\zeta t'/m} \frac{\xi(t')}{m} dt'. \quad (\text{A.6})$$

Returning to the velocity,

$$v(t) = e^{-\zeta t/m} \left[v(0) + \frac{1}{m} \int_0^t e^{\zeta t'/m} \xi(t') dt' \right]. \quad (\text{A.7})$$

Now, we can solve for the square of the noise averaged velocity using Eqn. A.7 and taking the ensemble average

$$\begin{aligned} \langle v(t)^2 \rangle &= e^{-2\zeta t/m} \left[v(0)^2 + \frac{v(0)}{m} \int_0^t e^{\zeta t'/m} \langle \xi(t') \rangle dt' \right. \\ &\quad \left. + \frac{1}{m^2} \int_0^t \int_0^t e^{\zeta(s'+t')/m} \langle \xi(t') \xi(s') \rangle ds' dt' \right] \\ &= e^{-2\zeta t/m} \left[v(0)^2 + \frac{C}{m^2} \int_0^t e^{2\zeta t'/m} dt' \right] \\ &= e^{-2\zeta t/m} v(0)^2 + \frac{C}{2\zeta m} \left[1 - e^{-2\zeta t/m} \right]. \end{aligned} \quad (\text{A.8})$$

From the equipartition theorem, $\frac{1}{2}mv^2 = \frac{1}{2}k_B T$. Plugging Eqn. A.8 into the equipartition theorem and taking the late time limit, we get the fluctuation-dissipation theorem:

$$C = 2\zeta k_B T. \quad (\text{A.9})$$

Therefore,

$$\langle \xi(t) \xi(t') \rangle = 2\zeta k_B T \delta(t - t'). \quad (\text{A.10})$$

The fluctuation-dissipation theorem connects the random force fluctuation amplitude to the drag force through ζ .

Appendix B

Numerics for Brownian dynamics simulations

Here, I connect the Langevin equation and Brownian dynamics simulations [28]. The Brownian equation of motion is

$$\dot{x} = -\zeta^{-1} [f(x, t) + \xi(t)], \quad (\text{B.1})$$

where the force $f(x, t) = -\frac{dU}{dx}$ depends on time and the noise has the properties

$$\langle \xi(t) \rangle = 0, \quad (\text{B.2})$$

$$\langle \xi(t) \xi(t') \rangle = 2\zeta k_B T \delta(t - t'). \quad (\text{B.3})$$

Integrating from t to $t + \delta t$ gives

$$x(t + \delta t) = x(t) - \zeta^{-1} \int_t^{t+\delta t} dt' f(x, t') + \xi(t'). \quad (\text{B.4})$$

To numerically evaluate this, we approximate the delta function in the noise term variance (Eqn. B.3) as

$$\delta(t - t') \approx \delta(t, t') = \begin{cases} \frac{1}{\delta t}, & \text{if } t \text{ and } t' \text{ are in the same time step } \delta t \\ 0, & \text{otherwise} \end{cases}. \quad (\text{B.5})$$

Thus, upon integration we get

$$x(t + \delta t) \approx x(t) - \zeta^{-1} \delta t \left[f(t) + c(t) \sqrt{\frac{2\zeta k_B T}{\delta t}} \right]. \quad (\text{B.6})$$

where $c(t)$ is a random number selected from a distribution with average zero and variance 1.

Typically, we select a number from the uniform distribution $r \in [-1/2, 1/2]$ which has a variance

of $1/12$. Thus, the position at time t_{n+1} is

$$x_{n+1} \approx x_n - \zeta^{-1} \delta t f_n + \sqrt{24D\delta t} r_n, \quad (\text{B.7})$$

where we have used the Einstein relation $D = \frac{k_B T}{\zeta}$. At each time step, f_n is calculated, and r_n is selected. In the absence of forces, the MSD is

$$\langle x_N^2 \rangle = 24D\delta t \langle r^2 \rangle N = 2Dt, \quad (\text{B.8})$$

after $N = t/\delta t$ steps. A step is randomly selected from a uniform distribution $\Delta x \in [-\sqrt{6D\delta t}, \sqrt{6D\delta t}]$ in a Brownian dynamics simulation. Note that one can select a random number from a Gaussian distribution instead of a uniform distribution. In that case, a random step length is selected from a Gaussian distribution with average $\mu = 0$ and variance $\sigma = \sqrt{2D\delta t}$.

Appendix C

Derivation of the Smoluchowski equation

Here, I present a derivation of the Smoluchowski equation starting from the Langevin equation [16]. The Smoluchowski equation describes the dynamics of the N particle noise ensemble density, $\rho^N(\mathbf{r}^N)$ where $\mathbf{r}^N = [\mathbf{r}_1, \mathbf{r}_2, \dots, \mathbf{r}_N]$. The Langevin equation is

$$\dot{\mathbf{r}}_i = \zeta^{-1} [-\nabla_i U(\mathbf{r}^N) + \boldsymbol{\xi}_i(t)], \quad (\text{C.1})$$

where i is the particle label, U the potential energy, and $\boldsymbol{\xi}_i$ the noise. Assuming the friction is isotropic, homogeneous, and does not mediate hydrodynamic interactions between particles, the noise has properties

$$\langle \xi_i(t) \rangle = 0, \quad (\text{C.2})$$

$$\langle \xi_i^\alpha(t) \xi_j^\beta(t') \rangle = 2\zeta \delta_{ij} \delta_{\alpha\beta} \delta(t - t'), \quad (\text{C.3})$$

where α, β refer to dimensions and i, j to particle label. Consider the N particle phase space density $f(\mathbf{r}^N, t)$, which describes the probability density of finding particles between \mathbf{r}^N and $\mathbf{r}^N + \delta\mathbf{r}^N$. Note that this does not depend on momentum because we are in the overdamped limit. In other words, we are averaging over the momentum degrees of freedom because we assume their dynamics equilibrate on time scales we are not interested in [24].

The probability density is conserved. Therefore, it obeys a continuity equation

$$\frac{df(\mathbf{r}^N, t)}{dt} = \frac{\partial f(\mathbf{r}^N, t)}{\partial t} + \nabla_i \cdot [\mathbf{r}_i^N f(\mathbf{r}^N, t)] = 0, \quad (\text{C.4})$$

where the Einstein summing convention is implied. In the absence of noise, this is the Liouville equation [16]. Including noise leads to the Fokker-Planck equation. Let $\mathbf{v}_i = -\nabla_i U(\mathbf{r}^N)$, and plug Eqn. C.1 into Eqn. C.4 to get

$$\frac{\partial f(\mathbf{r}^N, t)}{\partial t} + \nabla_i \cdot \zeta^{-1} [f(\mathbf{r}^N, t) (\mathbf{v}_i(\mathbf{r}^N) + \boldsymbol{\xi}_i(t))] = 0. \quad (\text{C.5})$$

We can separate the noise term to get

$$\frac{\partial f}{\partial t} = -\mathcal{L}f - \nabla_i \cdot \zeta^{-1} \boldsymbol{\xi}_i(t)f, \quad (\text{C.6})$$

where $\mathcal{L} = \zeta_i^{-1} \nabla_i \mathbf{v}_i$. Integrating with respect to time gives

$$f(t) = e^{-\mathcal{L}t} f(0) - \zeta^{-1} \int_0^t ds e^{-\mathcal{L}(t-s)} \nabla_i \cdot f(s) \boldsymbol{\xi}_i(s). \quad (\text{C.7})$$

We plug Eqn. C.7 back into Eqn. C.6 and take the noise average $\langle \dots \rangle$, which gives

$$\frac{\partial \langle f(t) \rangle}{\partial t} = -L \langle f(t) \rangle + \nabla_i \cdot \zeta^{-1} \langle \boldsymbol{\xi}_i \rangle e^{-\mathcal{L}t} f(0) \quad (\text{C.8})$$

$$- \nabla_i \cdot \zeta^{-2} \int_0^t ds e^{-\mathcal{L}(t-s)} \nabla_j \cdot \langle \boldsymbol{\xi}_i(t) f(s) \boldsymbol{\xi}_j(s) \rangle. \quad (\text{C.9})$$

Before we can use the properties of the noise to deal with the integral, we consider the $\langle \boldsymbol{\xi}_i(t) \boldsymbol{\xi}_j(s) f(s) \rangle$ term. The term $f(s)$ depends on the noise terms at earlier times, and the noise terms are delta-function correlated in time. Thus, there cannot be correlations between the noise at s and t and the phase space density because $f(s)$ only depends on noise at earlier times. Therefore, $\langle \boldsymbol{\xi}_i(t) \boldsymbol{\xi}_j(s) f(s) \rangle = \langle \boldsymbol{\xi}_i(t) \boldsymbol{\xi}_j(s) \rangle \langle f(s) \rangle = \langle \boldsymbol{\xi}_i(t) \boldsymbol{\xi}_j(s) \rangle \rho^N(s)$, where $\rho^N(\mathbf{r}^N, s) = \langle f(s) \rangle$ is the noise averaged phase space probability density. Making this substitution and using properties of the noise we get the Smoluchowski equation,

$$\frac{\partial \rho^{(N)}(\mathbf{r}^N, t)}{\partial t} = \nabla_i \cdot [\zeta^{-1} \nabla_i U(\mathbf{r}_N) \rho^{(N)}(\mathbf{r}^N, t)] + \nabla_i \cdot D \nabla_i \rho^{(N)}(\mathbf{r}^N, t), \quad (\text{C.10})$$

In the absence of fields, this is the diffusion equation. When the potential energy arises from an external field $U(\mathbf{r}^N) = \sum_i \phi(r_i)$, we recover the drift-diffusion equation. If more complicated friction tensors are involved, the equation becomes [24]

$$\frac{\partial \rho^{(N)}(\mathbf{r}^N, t)}{\partial t} = \nabla_i \cdot [\zeta_{ij}^{-1} \nabla_j U(\mathbf{r}_N) \rho^{(N)}(\mathbf{r}^N, t)] + \nabla_i \cdot \mathbf{D}_{ij} \nabla_j \rho^{(N)}(\mathbf{r}^N, t). \quad (\text{C.11})$$

Appendix D

Derivation of DDFT

This appendix describes how to go from the Smoluchowski equation to a closed form for the one-particle density using dynamic density functional theory [24]. The Smoluchowski equation describes the evolution of the N particle density $\rho^{(N)}(\mathbf{r}^N, t)$, the probability of finding the particles near $\mathbf{r}^N = [\mathbf{r}_1, \mathbf{r}_2, \dots, \mathbf{r}_N]$ in phase space, is

$$\frac{\partial \rho^{(N)}(\mathbf{r}^N, t)}{\partial t} = \nabla_i \left[\zeta_{ij}^{-1} \nabla_j U(\mathbf{r}^N, t) \rho^{(N)}(\mathbf{r}^N, t) \right] + \nabla_i D_{ij} \nabla_j \rho^{(N)}(\mathbf{r}^N, t), \quad (\text{D.1})$$

where U is the potential. In general,

$$U(\mathbf{r}^N, t) = \sum_{i=1}^N V_{\text{ext}}(\mathbf{r}_i, t) + \frac{1}{2} \sum_{j \neq i} \sum_{i=1}^N v_2(\mathbf{r}_i, \mathbf{r}_j) + \frac{1}{6} \sum_{k \neq j \neq i} \sum_{j \neq i} \sum_{i=1}^N v_3(\mathbf{r}_i, \mathbf{r}_j, \mathbf{r}_k) + \dots \quad (\text{D.2})$$

where V_{ext} is the potential from external fields and v_n is the n -body interaction potential. We are deriving an equation for the one-body density

$$\rho^{(1)}(\mathbf{r}) = N \int d\mathbf{r}_2 \dots \int d\mathbf{r}_N \rho^{(N)}(\mathbf{r}^N), \quad (\text{D.3})$$

which describes the probability of finding a particle at position \mathbf{r} irrespective of the other particles' locations. In general, the n -body particle density is [46]

$$\rho^{(n)}(\mathbf{r}^n) = \frac{N!}{(N-n)!} \int d\mathbf{r}_{n+1} \int d\mathbf{r}_N \rho^N(\mathbf{r}^N, t). \quad (\text{D.4})$$

We can integrate the Smoluchowski equation over coordinates $\mathbf{r}_2, \dots, \mathbf{r}_N$ to get

$$\frac{\partial \rho^{(1)}(\mathbf{r}_1, t)}{\partial t} = \nabla_1 D \nabla_1 \rho^{(1)}(\mathbf{r}_1, s) + \zeta^{-1} \nabla_1 \left(\rho^{(1)}(t) \nabla_1 V_{\text{ext}} \right) \quad (\text{D.5})$$

$$+ \nabla_1 D \int d\mathbf{r}_2 \rho^{(2)}(\mathbf{r}_1, \mathbf{r}_2) \nabla_1 v_2(\mathbf{r}_1, \mathbf{r}_2) \quad (\text{D.6})$$

$$+ \nabla_1 D \int d\mathbf{r}_2 \int d\mathbf{r}_3 \rho^{(3)}(\mathbf{r}_1, \mathbf{r}_2, \mathbf{r}_3) \nabla_1 v_3(\mathbf{r}_1, \mathbf{r}_2, \mathbf{r}_3) + \dots \quad (\text{D.7})$$

This is not a closed equation because the evolution of $\rho^{(1)}$ depends on the higher order densities $\rho^{(2)}, \dots, \rho^{(n)}$. Evans found a way to express the two-body density in terms of the direct correlation function $-k_B T \rho^{(1)}(\mathbf{r}_1) \nabla_1 c^{(1)}(\mathbf{r}_1) = \int d\mathbf{r}_2 \rho^{(2)}(\mathbf{r}_1, \mathbf{r}_2) \nabla_1 v_2(\mathbf{r}_1, \mathbf{r}_2)$ for a liquid in equilibrium [125].

This can be generalized for higher order terms [24] to give

$$-k_B T \rho^{(1)}(\mathbf{r}_1) \nabla_1 c^{(1)}(\mathbf{r}_1) = \sum_n \int d\mathbf{r}_2 \dots \int d\mathbf{r}_n \rho^{(n)} \nabla_1 v_n(\mathbf{r}^n). \quad (\text{D.8})$$

Plugging this into Eqn. D.5 gives a closed form for our equations if $c^{(1)}$ is known and not dependent on higher order densities. The direct correlation function in equilibrium can be expressed as a functional derivative of the excess free energy, *i.e.*, free energy contribution from interactions, with respect to the single body free energy [22, 23, 46, 125]

$$c^{(1)}(\mathbf{r}) = -\beta \frac{\delta \mathcal{F}^{\text{ex}} [\rho^{(1)}(\mathbf{r})]}{\delta \rho^{(1)}(\mathbf{r})}. \quad (\text{D.9})$$

This assumes that Eqn. D.8 and D.9 are valid for a fluid out of equilibrium [24]. This gives the DDFT equation of motion [22–24, 125]

$$\frac{\partial \rho(\mathbf{r}, t)}{\partial t} = \nabla \cdot \left[\zeta^{-1} \rho(\mathbf{r}, t) \nabla \frac{\delta \mathcal{F} [\rho(\mathbf{r}, t)]}{\delta \rho(\mathbf{r}, t)} \right], \quad (\text{D.10})$$

where we have dropped the superscript (1) from the one-body density. The free energy is separable into contributions from the ideal gas entropy, excess/interactions, and external fields [46]

$$\mathcal{F} = \mathcal{F}^{\text{id}} + \mathcal{F}^{\text{ex}} + \mathcal{F}^{\text{ext}}. \quad (\text{D.11})$$

The ideal gas and external contributions are exact [24, 46]:

$$\mathcal{F}^{\text{id}} = k_B T \int d\mathbf{r}^d \rho(\mathbf{r}) \left[\ln \Lambda^d \rho(\mathbf{r}) - 1 \right], \quad (\text{D.12})$$

where Λ is the thermal de Broglie wavelength and

$$\mathcal{F}^{\text{ext}} = \sum_{i=1}^N V_{\text{ext}}(\mathbf{r}_i, t). \quad (\text{D.13})$$

The excess free energy is not necessarily known and may be approximated [46]. DDFT, although built on the stochastic Langevin equation, is deterministic [132] because we have taken the noise ensemble average.

Appendix E

Second virial approximation

DDFT requires approximation of the excess free energy [25]. In general, the excess free energy can be expressed as a perturbative expansion of integrals of the one-body density and the Mayer function [46]

$$\mathcal{F}^{\text{ex}} = \frac{1}{2} \int \int \rho(\mathbf{r})\rho(\mathbf{r}') F_M(\mathbf{r} - \mathbf{r}') d\mathbf{r}' d\mathbf{r} \quad (\text{E.1})$$

$$+ \frac{1}{6} \int \int \int \rho(\mathbf{r})\rho(\mathbf{r}')\rho(\mathbf{r}'') F_M(\mathbf{r} - \mathbf{r}') F_M(\mathbf{r}' - \mathbf{r}'') F_M(\mathbf{r} - \mathbf{r}'') d\mathbf{r} d\mathbf{r}' d\mathbf{r}'' \quad (\text{E.2})$$

$$+ \dots \quad (\text{E.3})$$

where $F_M = \exp(-\beta V) - 1$ is the Mayer function. This is the virial expansion. At low density, the free energy is given by the second virial approximation

$$\mathcal{F}^{\text{ex}} \approx -\frac{k_B T}{2} \int \int \rho(\mathbf{r})\rho(\mathbf{r}') F_M(\mathbf{r} - \mathbf{r}') d\mathbf{r}' d\mathbf{r}. \quad (\text{E.4})$$

In the second virial approximation, the direct pair correlation function is

$$c^{(2)}(\mathbf{r}, \mathbf{r}') = -\beta \frac{\delta^2 \mathcal{F}}{\delta \rho(\mathbf{r}) \delta \rho(\mathbf{r}')} \approx F_M(\mathbf{r} - \mathbf{r}'). \quad (\text{E.5})$$

Consider steric interactions where overlap is forbidden. In this approximation,

$$c^{(2)}(\mathbf{r} - \mathbf{r}') = \begin{cases} -1 & \text{particles overlap} \\ 0 & \text{no overlap} \end{cases}. \quad (\text{E.6})$$

Thus in the second virial approximation, the correlations are approximated as correlation holes at distances corresponding to particle overlap, and non-overlapping particles are completely uncorrelated. Note that for a finite potential at high temperature, we can Taylor expand the Mayer

function to give

$$-\beta \mathcal{F}^{\text{ex}} \approx \frac{1}{2} \int \int \rho(\mathbf{r})\rho(\mathbf{r}')V(\mathbf{r} - \mathbf{r}') \, d\mathbf{r}' \, d\mathbf{r}, \quad (\text{E.7})$$

which is the mean field (random-phase) approximation [46]. For anisotropic particles, the Mayer function depends on the orientation $\hat{\mathbf{u}}$ of each particle, $F_M(\mathbf{r} - \mathbf{r}') \rightarrow F_M(\mathbf{r} - \mathbf{r}', \hat{\mathbf{u}}, \hat{\mathbf{u}}')$.

For spherocylinders in 2D, including finite width in the Mayer function in Eqn. E.4 amounts to adding a constant to the free energy, which drops when taking the functional derivative. Therefore, the second virial approximation can only model the infinitely thin rod system.

Appendix F

Repositories

Repository	Project	Owner	Paper	Notes
<i>ActiveDDFT</i>	Active needles	mstefferson	[53]	General DDFT model for self-propelled particles
<i>McHydro</i>	Soft obstacle	mstefferson	[21]	Monte Carlo lattice model for soft binding
<i>Hydrogel</i>	NPC selectivity	mstefferson	[45]	Reaction-diffusion equation solver
<i>hoppingSim</i>	NPC selectivity	LauraMaguire	[45]	BD simulation for bound motion in the NPC

Table F.1: GitHub repositories I collaborated on for projects described in this thesis.